

ABSTRACT

Title of dissertation: NUMERICAL SIMULATION OF
THE BLUE WHIRL: A REACTING
VORTEX BREAKDOWN PHENOMENON

Joseph D. Chung
Doctor of Philosophy, 2019

Dissertation directed by: Professor Elaine S. Oran
Department of Aerospace Engineering

The blue whirl is a small, stable, spinning blue flame that evolved spontaneously in recent laboratory experiments while studying turbulent, sooty fire whirls. It burns a range of different liquid hydrocarbon fuels cleanly with no soot production, presenting a new potential way for low-emission combustion. This thesis uses numerical simulations to present, for the first time, the flame and flow structure of the blue whirl. These simulations show that the blue whirl is composed of three different flames - a diffusion flame and a premixed rich and lean flame - all of which meet in a fourth structure, a triple flame which appears as a whirling blue ring. The results also show that the flow structure emerges as the result of vortex breakdown, a fluid instability which occurs in swirling flows. This thesis also presents the development and testing of the numerical algorithms used in the simulation of the blue whirl. This work is a critical step forward in understanding how to use this new form of clean combustion.

NUMERICAL SIMULATION OF THE BLUE WHIRL: A REACTING VORTEX BREAKDOWN PHENOMENON

by

Joseph Dongil Chung

Dissertation submitted to the Faculty of the Graduate School of the
University of Maryland, College Park in partial fulfillment
of the requirements for the degree of
Doctor of Philosophy
2019

Advisory Committee:

Professor Elaine S. Oran, Chair/Advisor

Professor James D. Baeder

Associate Professor Michael J. Gollner, Dean's Representative

Research Associate Professor Carolyn R. Kaplan

Professor Norman M. Wereley

Professor Kenneth H. Yu

© Copyright by
Joseph Dongil Chung
2019

Acknowledgments

I would like to first thank my advisor, Dr. Elaine S. Oran. I thank her for accepting me into her group and guiding my research through the past three years. Most importantly, she taught me to ask the critical questions of “why?” and “how?” and showed me how to unravel what seemed to be the most complicated ideas. I also thank my committee members, Dr. James D. Baeder, Dr. Michael J. Gollner, Dr. Carolyn R. Kaplan, Dr. Norman M. Wereley, and Dr. Kenneth H. Yu. I thank my friends and officemates (both past and present) who have helped me in many ways, from offering simple advice on how to navigate graduate school to helping solve some of my most critical technical problems. Finally, I owe much of my success to my colleague and wife, Xiao Zhang. I would not have made it this far without her support both in the research and at home.

This work was supported by the Army Research Office (grant W911NF1710524), the National Science Foundation (award CBET 1839510), and by the Army Research Laboratory (under Cooperative Agreement Number W911NF-19-2-0307). Computations were performed using the University of Maryland Deepthought2 HPC cluster and DoD HPCMP resources.

Table of Contents

Table of Contents	iii
List of Tables	v
List of Figures	vi
List of Abbreviations	xi
1 Introduction	1
1.1 Objectives	3
1.2 Literature Review	4
1.2.1 Fire Whirls	4
1.2.2 Blue Whirl	7
1.3 Approach to Simulate the Blue Whirl	10
2 Numerical Methods	12
2.1 Barely Implicit Correction	12
2.2 Integration of BIC with Combustion	16
2.2.1 Governing equations	17
2.2.2 Chemical-diffusive model	18
2.2.3 Temporal integration procedure	20
2.3 Chemical-Diffusive Model	27
2.3.1 Diffusion Parameters	30
2.3.2 Reaction Parameters	32
2.3.3 Computing Progress Variable	34
2.3.4 Computing species conversion and heat release	36
3 Test Problems	38
3.1 One-dimensional, premixed, laminar flames	39
3.1.1 Boundary and Initial Conditions	40
3.1.2 Comparison of explicit FCT and BIC-FCT	41
3.1.3 Convergence test	43
3.1.4 Varying Stoichiometry	44
3.2 Two-dimensional coflow diffusion flame	46
3.3 Two-dimensional counter flow diffusion flame	47
3.3.1 Boundary and Initial Conditions	48

3.3.2	Results	49
3.4	Two-dimensional triple flame	54
3.4.1	Boundary and Initial Conditions	55
3.4.2	Results	57
3.5	Two-dimensional, unsteady, coflow diffusion flame	59
3.5.1	Boundary and Initial Conditions	59
3.5.2	Results	61
3.6	Three-dimensional fire whirl	62
3.6.1	Boundary and Initial Conditions	64
3.6.2	Results	65
3.7	Summary and Conclusions	74
4	Reactive Vortex Breakdown	77
4.1	Introduction	77
4.2	Numerical Model	79
4.3	Parameter Study	80
4.3.1	Geometrical Setup and Boundary Conditions	81
4.3.2	Results	82
4.3.3	Discussion	87
4.4	Lifted Flame Computations	88
4.4.1	Geometrical Setup and Boundary Conditions	88
4.4.2	Results and Discussion	90
4.4.3	Increased Resolution	93
4.4.4	Conclusions	95
5	Blue Whirl	97
5.1	Computational setup	97
5.2	Simulation pathway	99
5.3	Results	104
5.3.1	The flame structure revealed	104
5.3.2	Flow structure	108
5.3.3	Comparison with Burgers vortex model	109
5.3.4	Boundary layer diagnostics	112
5.4	Discussion	114
5.5	Computational resources required	117
6	Summary and Conclusions	118
6.1	Summary of Contributions	122
6.2	Recommendations for Future Work	123
A	Parametric study results	124

List of Tables

4.1	Fuel inflow conditions for the 7 cases in the parametric study. The fuel supply rate is the equivalent volumetric flow rate for liquid heptane whereas the fuel velocity is for the gaseous flow rate.	82
-----	--	----

List of Figures

1.1	a) A blue whirl. b) Slightly unstable blue whirl with yellow bubble in the middle, taken from [1].	1
1.2	A fire whirl at the University of Maryland, reprinted from [12].	5
1.3	Four common types of configurations for reproducing fire whirls in experiments. Reprinted from [17].	6
1.4	The three major modes of vortex breakdown as identified from [26]. (a) and (c) reprinted from [26]. (b) is reprinted from [28].	8
2.1	Flowchart of the coupling of the physical processes in one time-step. The sub-cycling procedure is changed from the prior paper [29] to include the effects of chemical reactions and heat release.	20
2.2	Reference heat diffusivity versus equivalence ratio for heptane-air (dashed-dot blue line) and ethylene-air (solid black line) mixtures.	32
2.3	Normlized heat release versus equivalence ratio for heptane-air (dashed-dot blue line) and ethylene-air (solid black line) mixtures.	33
2.4	Optimized CDM parameters for ϕ in the range of 0.35 to 2.50 for heptane-air with $T_0 = 372$ K and ethylene-air with $T_0 = 298$ K. . . .	35
3.1	A schematic of the boundary conditions, initial conditions, and computational mesh used in the 1D, steady-state, premixed, laminar flame computations.	41
3.2	A comparison of a one-dimensional, heptane-air, stoichiometric, premixed, laminar flame computation using the explicit FCT (blue square) and the implicit BIC (red circles) algorithms.	42
3.3	The error in flame speed from BIC-FCT using the CDM with varying resolution for stoichiometric, heptane-air flame, shown on the horizontal axis as the number of cells within the ideal flame thickness (0.28 mm). The error compares against the ideal flame speed of 65.51 cm/s.	43

3.4	A comparison of flame temperature, speed, and thickness for heptane-air mixtures. Blue lines are computed from Cantera [61] with the 188-species n-Heptane Lu and Law [58] mechanism. Red squares are computed using BIC-FCT with the calibrated CDM as the chemical model.	44
3.5	A comparison of flame temperature, speed, and thickness for ethylene-air mixtures. Blue lines are computed from Cantera [61] with the Wang and Laskin [59] mechanism. Red squares are computed using BIC-FCT with the calibrated CDM as the chemical model.	45
3.6	A steady state computation of a 2D, laminar, n-Heptane and air, coflow diffusion flame.	47
3.7	Simulation of a ethylene-air, counter-flow diffusion flame. The red box in (a) shows a zoomed in region of the mesh refinement.	49
3.8	A comparison of results from two steady-state counter-flow diffusion flame computations using BIC-FCT and the Cantera [61] chemical equilibrium software. (a) - (c) are results from air and fuel inflow of 4 m/s, whereas (d) - (f) are results for 3 m/s. BIC-FCT uses the CDM as its chemical model for a 2D counter flow flame simulation. Cantera uses a detailed mechanism [59] for a quasi-1D counter flow flame simulation. Cantera results are dashed red lines and BIC-FCT results are solid black lines.	51
3.9	A comparison of Cantera and BIC-FCT-CDM in how they predict the temperature versus strain relationship for counter-flow diffusion flames of ethylene-air. The strain is calculated as the maximum velocity gradient on the oxidizer side of the flame.	53
3.10	Schematic of the mesh and the initial and boundary conditions for a triple flame simulation. The red box in (a) shows a zoomed in region near the mesh refinement.	54
3.11	Maps of (a) temperature, (b) equivalence ratio, and (c) flame index overlaid with contours of heat release rate of the triple-flame simulation.	58
3.12	Boundary conditions overlaid with the instantaneous temperature map from the simulation result of a the 2D, unsteady, coflow diffusion flame.	59
3.13	Temperature maps at different time instants in the simulation. a) 19.843 s, b) 19.852 s, c) 19.862 s, d) 19.873 s, e) 19.883 s, f) 19.893 s, and g) 19.902 s	61
3.14	Three-dimensional, unsteady fire whirl computation. (a) A schematic of the geometrical setup (not to scale) and boundary conditions for the fire whirl computation. (b) A slice of the computational mesh overlaid with the 3D contour heat release. The mesh is refined in the center.	63
3.15	Volume renderings of the temperature for selected time instances. Visualization was performed using the yt-project python library [70].	66
3.16	Volume renderings of the stoichiometric equivalence ratio. Visualization was performed using the yt-project python library [70].	67

3.17	Instantaneous maps of (a) temperature, (b) tangential velocity, (c) axial velocity, and (d) gauge pressure at $t = 8.95$ s. The gauge pressure is defined as $P - 101316$ Pa where P is the absolute pressure and 101316 Pa is the minimum measured pressure within the domain. . . .	68
3.18	Averaged (a) temperature, (b) axial velocity, (c) tangential velocity, and (d) gauge pressure of the fire whirl simulation. The averaging was performed over the last 2 s of the computation.	70
3.19	A comparison of averaged results from the CFD simulation and a curve fit using a Burgers vortex model for tangential velocity. The filled circles correspond to the locations of computational cells in the simulation.	74
4.1	(Reprinted from [15]) Measured velocities at the slit inlets at different heights above the bottom surface. The fuel evaporation rates given in terms of volumetric flow rates, \dot{V} , are presented for each of the corresponding velocity measurements. Note that the blue whirl is observed for lower fuel flow rates, from $\dot{V} = 0.6$ to 1.1 ml/min. . . .	80
4.2	Schematic of the domain and boundary conditions used in the parametric study. The slit velocity is 40 cm/s and pushes in air. The fuel is heptane. In the parameter study, the fuel diameter and fuel mass flow rates are varied.	81
4.3	Case 1	83
4.4	Case 6	83
4.5	Constant fuel flow rate.	85
4.6	Constant fuel diameter.	86
4.7	(a) The geometrical setup and boundary conditions. (b) A cut view of the computational mesh. The numbers indicate the number of cells at the coarsest and finest levels of refinement.	88
4.8	Contours of (a) temperature, (b) axial velocity, (c) tangential velocity, and (d) normalized pressure.	90
4.9	Contours of the flame index overlaid with contours of heat release within a zoomed in region of the reactive bubble.	93
4.10	refinement	94
4.11	Temperature contour maps with superimposed heat release contour lines on vertical slices taken at various locations across the flame. From (a) to (g) vertical slices (z-y plane) are taken from $x = 0.144$ m to $x = 0.156$ m with a 0.002 m interval. The flame structure is shown by a 3D heat release surface contour with a value of 1×10^6 W/m ³ . A horizontal (x-y plane) slice is taken at the bottom of the domain ($z = 0$ m) colored by fuel mass fraction, on which the region with high fuel concentration indicates the fuel inflow.	95

4.12	Flame index maps with superimposed heat release contour lines on vertical slices taken at various locations across the flame. From (a) to (g), vertical slices (z-y plane) are taken from $x = 0.144$ m to $x = 0.156$ m with a 0.002 m interval. The flame structure is shown by a 3D heat release surface contour with a value of 1×10^6 W/m ³ . A horizontal (x-y plane) slice is taken at the bottom of the domain ($z = 0$ m) colored by fuel mass fraction, on which the region with high fuel concentration indicates the fuel inflow.	96
5.1	Computational setup. a) Schematic of the computational domain and the boundary conditions. b) A center slice of the 3D computational mesh. The mesh is composed of cubical control volumes. The width of the control volume in each level of refinement is half the width of the coarser level. The mesh is refined around the blue whirl which is shown as a volume rendering of the heat release rate. The size of the largest and smallest cells (Δx_{Max} , Δx_{Min} respectively) and the number of cells in the coarsest and finest mesh are indicated in b.	98
5.2	First step in the simulation pathway. Center-slice map of temperature (shown in units of K). Solid teal line is the stoichiometric contour. The dashed white lines are contours of zero axial velocity, indicating the regions of reverse flow. The mesh is refined with 2 levels and the fuel inflow diameter is 2.54 cm with an equivalent liquid fuel supply rate of 0.4 ml/min.	100
5.3	Second step in the simulation pathway. The fuel inflow diameter is decreased from 2.54 cm to 0.9 cm and the equivalent liquid fuel supply rate is changed from 0.4 ml/min to 0.35 ml/min. See Fig. 5.2 for color and contour description.	101
5.4	Third step in the simulation pathway. The mesh is refined another level from the second step. See Fig. 5.2 for color and contour description.	102
5.5	Fourth step in the simulation pathway. The mesh is refined another level from the third step. See Fig. 5.2 for color and contour description.	102
5.6	Fifth step in the simulation pathway. The mesh is refined another level from the fourth step. See Fig. 5.2 for color and contour description.	103
5.7	The flame structure of the blue whirl. a) Volume rendering of the heat release rate from the numerical simulation described in the text. b) Schematic diagram that summarizes a final result of the blue whirl simulation. c) Observed blue whirl.	105
5.8	Comparison of a) experimental OH* concentration measurement (taken from Fig. 8a in [14]) with b) 3D volume rendering of heat release rate in the simulation. The volume rendering is taken from the side view.	106
5.9	Slices through the center of the computational domain and parameters selected for combustion diagnostics. a) Flame index. b) Equivalence ratio. c) Temperature. Contours of heat release rate are superimposed on top to indicate reaction regions. Slices are shown for a zoomed in region which is 8 cm wide.	107

5.10	Slices through the center of the computational domain and values selected for flow diagnostics. a) Streamlines. b) Tangential velocity. c) Axial velocity. Contours of heat release rate are superimposed on top to indicate reaction regions. Slices are shown for a zoomed in region which is 8 cm wide. d) Line plot of tangential velocity taken below the blue whirl from the white dashed line in b), shown for the entire width of the computational domain.	110
5.11	A comparison of a time instance from the blue whirl simulation and a curve fit using the Burgers vortex model for tangential velocity. The simulation results are extracted along the x direction at a height of 7 mm, about 5 mm below the flame.	111
5.12	A comparison of a time instance from the blue whirl simulation and a curve fit using the Burgers vortex model for tangential velocity. The simulation results are extracted along the x direction at a height of 80 mm, approximately 40 mm above the flame.	112
5.13	Streamlines superimposed on a 3D heat release rate isocontour of 3 MW/m ³ . a) Streamlines which originate at 0.5 mm from the lower boundary. b) Streamlines which originate at 2.0 mm from the lower boundary. The streamlines are colored by the local temperature of the flow. A 2D map of fuel mass fraction along the bottom boundary is shown, indicating the region of fuel inflow. The box indicates the region of mesh refinement.	113
A.1	Case 2	124
A.2	Case 3	125
A.3	Case 4	125
A.4	Case 5	126
A.5	Case 7	126

List of Abbreviations

CFD	Computational Fluid Dynamics
BIC	Barely Implicit Correction
FCT	Flux-Corrected Transport
CDM	Chemical-Diffusive Model
CFL	Courant-Friedrichs-Lewy

Chapter 1: Introduction

A blue whirl, shown in Fig.1.1a, is a small, soot-free blue flame that was discovered serendipitously while performing experimental studies of fire whirls burning liquid hydrocarbon fuels on a water base [1]. Even though fire whirls are dangerous, violent, turbulent eddies of fire, they can be created in (relatively) safe, confined conditions for laboratory study (e.g., [2, 3, 4, 5, 6, 7, 8]). Because fire whirls burn at higher temperatures [9] with higher burning rates [3, 10, 11] than their nonwhirling counterparts, preliminary studies [1] were being performed to determine if it would be beneficial to use controlled fire whirls for practical purposes, such as oil-spill remediation.

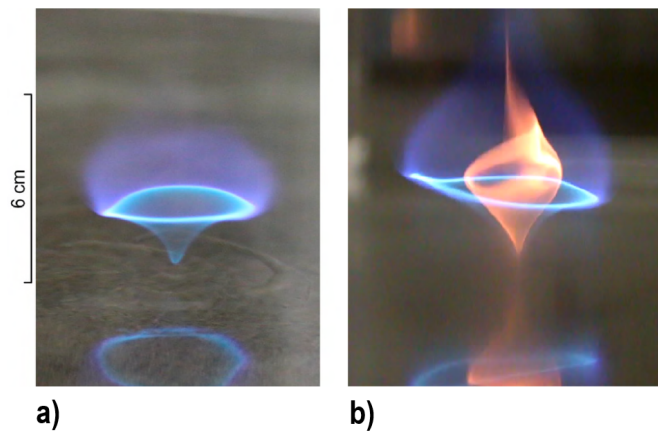


Figure 1.1: a) A blue whirl. b) Slightly unstable blue whirl with yellow bubble in the middle, taken from [1].

In the experiment, the blue whirl evolves from a fire whirl which burns liquid fuel poured onto a water base. The blue whirl appears as a stable, quiet, strongly swirling, hydrocarbon flame sitting on a water surface. The blue burning state, which implies nearly soot-free combustion, indicates its potential of contributing to highly efficient, low-emissions combustion with no harm to humans or to the natural environment. Understanding the blue whirl is important to be able to harness this potential for clean burning.

Since the initial discovery, experiments [12, 13, 14, 15, 16] have given considerable information about the formation conditions and thermal structure of the blue whirl. There has not, however, been any clear theory or measurements that reveal the flame structure or dynamics. Only if we understand its structure can we find ways to tame it, scale it, and create it at will.

There are two limits of laminar flames that are discussed quite separately in the literature. In a *laminar premixed flame*, the flame front passes through premixed fuel and oxidizer, leaving behind the reaction products. The flame front is driven by expansion due to heat release from the reactions and physical diffusion processes, such as thermal conduction, molecular diffusion, and radiation transport. There can be fuel-lean, stoichiometric, and fuel-rich premixed flames. This is to be contrasted to a *laminar diffusion flame*, in which the fuel and oxidizer are initially separated and mix by physical diffusion processes. In this case, the rates of reactions are controlled by diffusion and the flame is said to be “diffusion limited.”

Thus a fundamental question for combustion theory that was posed by the blue whirl is: *What is the flame structure of the blue whirl?* Is it a premixed flame or a

diffusion flame, or some combination? This work attempts to answer this question through numerical simulations.

1.1 Objectives

There are two key objectives in this thesis:

- Identify the flame and flow structure of the blue whirl.
 1. Reproduce the blue whirl within numerical simulations.
 2. Identify whether it is a diffusion flame, premixed flame, or both using computational diagnostics.
 3. Characterize the flow field and its relationship to the flame.
- Develop the numerical model and tool which can be used to explore the formation conditions of the blue whirl.
 1. Develop and implement a combustion model which considers the critical characteristics of low-Mach-number flames for *both* premixed and non-premixed systems and can resolve these characteristics in a computationally efficient way.
 2. Integrate the combustion model into an algorithm which can efficiently resolve the time-dependent dynamics of low-Mach-number, compressible fluids.
 3. Build a code that incorporates these algorithms to compute low-Mach-number, reactive flows.

4. Test this code and algorithm on multiple applications to assess its ability in simulating low-Mach-number flames.

1.2 Literature Review

Fire whirls (an example is shown in Fig. 1.2) form when circulation couples with burning or burned gasses, generating a vortex column of hot material. Most experiments have studied fire whirls using confined configurations [17]; four common configurations are shown in Fig. 1.3. Three of these (Figs. 1.3a, b, and c) place walls with open slits (labeled as “air intake” in Fig. 1.3) around a liquid-fuel pool. When the fuel is ignited, the resulting flame entrains air through the slits. The slits are strategically placed so that the entrained air enters the configuration tangential to the flame, thereby imposing circulation.

1.2.1 Fire Whirls

Velocity measurements have been made by Hassan et al. [4], Hayashi et al. [6], and Wang et al. [7] who used the offset, half-cylinder configuration in Fig. 1.3a and by Lei et al. [18] who used the square enclosure shown in Fig. 1.3b. These experiments measured the velocity field using particle image velocimetry (PIV), showing that the flow exhibits characteristics of solid-body rotation within a core and irrotational, free vortex characteristics outside of it. Hassan et al. [4], Wang et al. [7], and Lei et al. [18] found that their tangential velocity data fit well with a Burgers vortex. Hayashi et al. [6], however, showed that the Burgers vortex does



Figure 1.2: A fire whirl at the University of Maryland, reprinted from [12].

not provide an accurate description of the fire whirl vortex.

Emmons and Ying [3] presented one of the earliest temperature measurements of a fire whirl. They used a rotating screen, shown in Fig. 1.3d, to impose circulation. They showed that increasing circulation causes the temperature to peak at a certain radius and become colder in the center, suggesting that increasing circulation would increase the fuel concentration within the core. Similar trends in the radial temperature profile are also seen in later experiments, such as those by Lei et al. [5, 18] using a square configuration.

Lei et al. [19] also used a rotating screen, except here, they decoupled the circulation from the fuel consumption rate by injecting gaseous fuel instead of using

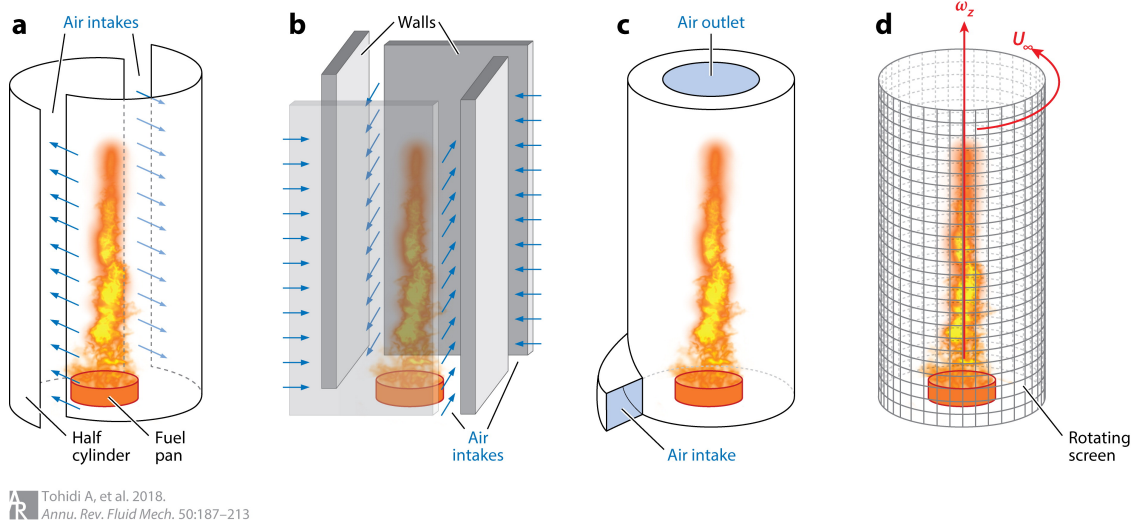


Figure 1.3: Four common types of configurations for reproducing fire whirls in experiments. Reprinted from [17].

a liquid-fuel pool. By changing the circulation for different fuel flow rates, they observed the fire whirl transitioning through distinct states which were characterized by the shape of the flame.

Numerical simulations [4, 20, 21, 22, 23, 24, 25] have been able to predict many of these reported features of fire whirls. Satoh and Yang [20] solved the unsteady conservation laws to study how the walls of a square enclosure affect the entrainment of air. Their model used constant gas properties (i.e. viscosity, heat conduction, and heat capacity did not vary with temperature) and a specified region of constant heat release as a surrogate for combustion. Using this simplified numerical approach, they were able to compute the entrainment of air and the velocity field of a fire whirl. They found that if the width of the air inlet was increased beyond a critical size, the flow would no longer whirl.

Snegirev et al. [21], incorporating a single-step combustion model with soot production and radiation, simulated fire whirls in an open, unconfined configuration,

with specified velocity profiles at the boundary representing a free vortex. They found that their resulting flow profiles matched more closely with that of a Rankine vortex. Similar to experiments by Lei et al. [19], computations by Snegirev et al. [21] showed that increasing circulation would increase the flame length until a critical value of circulation was reached, after which, the flame length would decrease. They also performed simulations of fire whirls in a square enclosure with one slit and compared the results to their experiments. Their simulation results reproduced the “periodic process of formation, precession and destruction of the whirling flame” [21] that was seen in the experiments. Hassan et al. [4], Chuah and Kushida [22], Kuwana et al. [23], also used axisymmetric simulations with single-step combustion models. Their results agreed favorably with their respective fire whirl experiments in predicting the expected vortex flow structure and flame shapes.

1.2.2 Blue Whirl

In the initial experiments [1], the blue whirl evolved spontaneously from a 1-m high fire whirl in a few seconds, as the whirling flame transitioned through a series of intermediate states. The result was that a noisy, turbulent, yellow fire whirl changed into a quiet, laminar, blue spinning flame. The glowing soot patterns formed in the intermediate states suggested the complex reactive-flow system was subject to the fluid dynamics instability, *vortex breakdown*, which changes the structure of swirling flows into bubble, helical, or whirling structures [26, 27], shown in Fig. 1.4.

Hariharan et al. [12, 13, 14] investigated the thermal structure of the blue

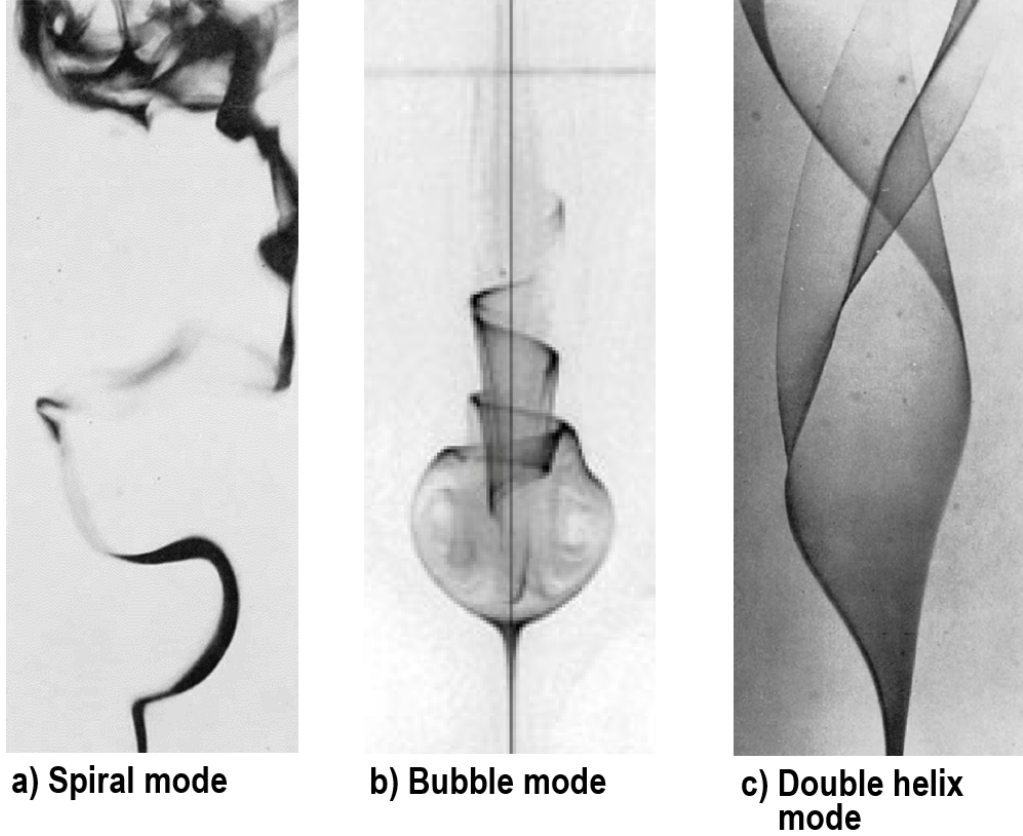


Figure 1.4: The three major modes of vortex breakdown as identified from [26]. (a) and (c) reprinted from [26]. (b) is reprinted from [28].

whirl within the same configuration as [1]. They showed that the hottest regions of the blue whirl are in the blue ring and in the upper, hazy region above the blue ring by using two-dimensional temperature maps produced by thin-filament pyrometry. Their thermocouple measurements showed that the temperature peaks around 2000 K. They also demonstrated that the blue whirl forms with many different fuels, extending upon what was originally reported by Xiao et al. [1]. In these studies, the blue whirl formed for heptane [1, 12, 13, 14], iso-octane [13], cyclohexane [13], and even crude oil [1].

Hariharan et al. [14] also investigated the role of the boundary layer in the blue whirl. By placing fuel flush with the bottom surface, on a pan above it, and then

below it, they found that the blue whirl only forms when the fuel is flush with the bottom surface. This showed that a *smooth* boundary layer may be necessary for the blue whirl to form and gave a possible explanation as to why prior experiments did not observe the blue whirl. In prior configurations, the boundary layer near the flame is disturbed by the presence of a fuel pan or rotating mesh. Adding to the original visualization [1], they more clearly visualized the recirculating flow within the blue whirl by using controlled exposure images of the glowing soot, strongly suggesting that vortex breakdown may play a key role in the blue whirl formation. Their OH* chemiluminescence measurements showed that most of the heat release occurs within the bright blue ring, with a small amount of heat release in the upper hazy region, and almost none in the lower cone.

Hu et al. [15] measured the fuel consumption rates and slit inflow velocities as the fire whirl transitioned to the blue whirl. Using these measurements, they identified the range of circulation and heat release values for which the blue whirl can form. Their velocity measurements suggested that circulation peaks around the height of the blue ring, decreases above it, and remains constant above the visible flame region.

Coenen et al. [16] developed a new configuration using 12 walls, instead of 2 half cylinders. By changing the angle of the walls, they could *control* the imposed swirl on the flame, thereby controlling the visible states of the fire whirl. They showed that the blue whirl formed for high swirl levels. During its formation, they visualized the flame receding from the edge of the liquid-fuel pool and eventually lifting up into the blue whirl.

1.3 Approach to Simulate the Blue Whirl

Parallel to experiments, there have been computational and theoretical efforts to simulate fire whirls and the evolution to a blue whirl. In experiments, the blue whirl moves around and makes it difficult to diagnose. Therefore, the flow and flame structure are still not certainly defined. This led us to believe that a full numerical simulation, from a fire whirl to a blue whirl, would be needed to tell us what the blue whirl really is. Such a simulation capability could also be used with experiments to study fundamental questions, such as whether the blue whirl scales or how to create it more directly without going through the full, dangerous fire whirl state.

Simulating a realistic fire whirl is expensive computationally because of the very wide range of space and time scales involved. Simulating a blue whirl would mean either simulating a fire whirl subject to vortex breakdown, or finding a way to go more directly to blue-whirl conditions. At the beginning of the simulation effort, we did not know which approach, or whether a combined approach, would work best. This leads us to a computational “hunt” for the blue whirl, in which we first developed the numerical method and then used the simulations to explore the effects of varying the controlling parameters, for example, fuel and air inlet sizes and velocities.

In a separate work related to this thesis, we took the approach to creating the simulations by first simulating vortex breakdown in a nonreactive gas in order to observe the modes induced by vortex breakdown as they evolve in a gaseous reactive flow. This led to the development of the low-Mach-number algorithm [29]

described in more detail in the following chapters. Then, in this thesis, we developed a chemical-diffusion model (CDM) that reproduces features of a diffusion flame as well as a premixed flame, and found parameters for it suitable for heptane [30] used as the fuel in the original experiments. The next step taken this thesis is simulating a series of low-Mach-number flames with successively increasing difficulty to ensure the computed flow and properties are consistent with experimental observations. These test problems culminate with a fire whirl. This required generalizing the low-Mach-number algorithm so that it is able to simulate reactive flow, with energy release and species conversion. Then we simulated *reactive vortex breakdown*, as it would occur when the swirling gas consists of an ignited mixture of fuel and air. The conditions should be similar to those that produced the experimentally observed blue whirl. Finally, we used the new numerical model and the general initial conditions of the experiment to reproduce the blue whirl numerically.

This thesis presents the first results of unsteady, three-dimensional (3D) numerical simulations that examine vortex breakdown in a reactive flow that leads to a blue whirl. It reveals the flame and flow structure of the blue whirl through a series of numerical diagnostics, relates the results to prior experiments, and suggests a path forward for both future experiments and simulations to examine and potentially use this new, soot-free flame structure. We first describe the combustion model used in this study in Chapter 2, outline the fluid model and its test problems in Chapter 3, present results of reactive vortex breakdown simulations in Chapter 4, and finally present the blue whirl results in Chapter 5.

Chapter 2: Numerical Methods

In this chapter, we present the numerical methods used to simulate the blue whirl. The chapter is organized by two sections. The first section describes the methods used to model the fluid equations and how to couple them to the combustion processes. The second section describes how to calibrate the combustion model and the resulting parameters that are used in the simulations.

2.1 Barely Implicit Correction

Numerical modeling of low-Mach-number flows poses distinct challenges to the application of reactive-fluid algorithms. These challenges arise from the time-varying local and intense chemical energy release, the steep gradients that form within flames, and the disparity of time scales among the acoustic, chemical, and convective processes. How to address these challenges and efficiently solve the governing equations is an important area of research.

Flames form steep gradients of density, temperature, and momentum, and can introduce numerical instability into a computation. High-order, monotone methods can be used to overcome this difficulty [31]. They were developed to maintain monotonicity and stability near steep gradients by strategically reducing the local

accuracy near discontinuities to first-order while retaining high-order accuracy near smoother parts of the flow. These methods are widely applied to supersonic flows, subsonic flows with turbulence, and reactive flows which transition from low-speed flames to high-speed detonations. Many of these methods are reviewed in [32].

High-order, monotone algorithms were originally designed to use explicit time integration, so that the computational time-step is restricted by the sound speed and flow velocity or any processes requiring smaller times. Explicit time integration poses no serious limitation on computational efficiency when computing supersonic or fast subsonic flows because the convective and acoustic time scales are comparable. Directly adopting explicit algorithms for low-speed flows, especially with chemical reactions, however, can be prohibitively expensive due to the large difference in time scales among the convective, acoustic, and chemical processes.

Low-Mach-number approximations of the Navier-Stokes equations were proposed to overcome the numerical stiffness introduced by these differing time-scales. A limiting case of low-Mach-number approximations completely removes acoustic waves from the equations, resulting in the incompressible Navier-Stokes equations. Algorithms for low-Mach-number, compressible flows take two main approaches: the first modifies compressible solvers and the second extends incompressible solvers to include compressibility. A brief review of these algorithms can be found in [33].

The objective of low-Mach-number algorithms derived by modifying compressible solvers is to remove the acoustic limitation on the time step. One way to do this is precondition the governing equations to scale the eigenvalues to a similar order of magnitude, so that differences in time-scales between physical processes is

minimized. Examples of this approach include Turkel [34], Choi and Merkle [35], and Liou [36]. The modified equations, however, do not describe the same transients as the original system of equations because preconditioning changes the time derivatives by pre-multiplying them with a designed preconditioning matrix.

In another approach, perturbation or asymptotic methods are used to decouple the physical acoustic waves from the system of equations by using regular perturbation theory and applying a Taylor series expansion of the Mach number to the variables. Examples of this include the methods developed by Jones & Boris [37], Rehm & Baum [38], and Thornber et al. [39]. As the Mach number is sufficiently small, the asymptotic approximation still allows compression and rarefaction over time. The spatial variations in pressure, however, are filtered out, which means acoustic wave effects are eliminated.

The low-Mach-number algorithms that adopt pressure as a primary variable are modified from incompressible solvers. A common method is the pressure-correction, or projection method. These methods use a fractional step technique which first advances the solution in time with a prediction using the asymptotic approximation. They then correct the pressure to enforce the divergence constraint imposed on the velocity. Examples of this approach include the SIMPLE family of algorithms [40, 41], and methods for reactive flows developed by Tomboullides et al. [42] and Motheau & Abraham [43]. These methods may converge slowly because the pressure and velocity are updated through an iterative process.

In previous work [29], we applied the Barely Implicit Correction (BIC) [44, 45] to the fourth-order, Flux-Corrected Transport (FCT) [46] algorithm for nonreactive,

low-Mach-number flows. This approach first solves the full Navier-Stokes equations using an explicit, monotone algorithm as a prediction and then solves one elliptic equation for a pressure correction, thus eliminating the sound speed restriction in the time step. This method lowers the cost per time step from that of an explicit solution and preserves the effects of acoustic waves when needed. In [29], we stabilized the BIC-FCT algorithm and then demonstrated its ability to compute low-Mach-number, viscous, swirling flows efficiently with and without open boundaries.

In this chapter, we show how the BIC integration procedure can be expanded to include chemical reactions with heat release and physical diffusion processes. The base monotone algorithm, fourth-order FCT, is the same as used in the nonreactive BIC algorithm[44]. Including the chemistry and diffusion processes is illustrated with a calibrated, chemical-diffusive model (CDM) [30, 47, 48]. We use BIC-FCT and the CDM to compute a series of test problems, each demonstrating a different aspect of the algorithm. A series of one-dimensional, premixed flames are first computed, and these show that the computed flame properties agree well with results from chemical equilibrium software and a detailed chemical-transport model. Two-dimensional (2D) counter-flow diffusion flames are then computed, which also show good agreement with chemical equilibrium software computations. A two-dimensional triple flame is simulated to show that the method can compute complex flame structures containing diffusion flames as well as rich and lean premixed flames. Finally, we compute an unsteady, three-dimensional (3D) fire whirl to demonstrate that the method can compute complex, unsteady combustion in a turbulent, swirling flow.

2.2 Integration of BIC with Combustion

The BIC algorithm was originally designed to remove the acoustic limit on the CFL time step when solving the inviscid Euler equations [44]. The first step computes an explicit prediction of the mass, momentum, and energy conservation equations using a monotone method. Here, we use the fourth-order, flux-corrected transport (FCT) algorithm [46, 49], although in principle this approach can be applied to any monotone explicit algorithm. Then, an implicit correction is computed by solving one elliptic equation for the change in pressure throughout the time step. This pressure change is used to correct the predicted momentum and energy at the end of the time step.

The prior paper [29] outlined the BIC procedure and showed how it could be used to solve the Navier-Stokes equations for low-Mach-number, viscous flows. In this procedure, time-step splitting is used to first compute the diffusion fluxes and then compute the convection fluxes using the BIC algorithm. Changes in internal energy from the diffusion fluxes were removed and stored as a separate scalar variable before computing the convection fluxes and this avoided problems with asynchronization. This new variable was added back into the energy as a source term during the explicit prediction and equilibrated through the pressure correction process. The source term, however, can introduce spurious oscillations during the pressure correction. A monotone filter was introduced [29] to remove these oscillations by passing the conservative variables through an extra FCT step with no pressure gradients or convection. By doing this, controlled amount of numerical

diffusion is selectively added to the regions of the flow with spurious oscillations, enforcing monotonicity.

In this section, we show how chemical reactions and species diffusion processes can be included in the BIC procedure. This can be used as a guide to adding more complex source terms in the future.

2.2.1 Governing equations

Consider the time-dependent, compressible, reactive Navier-Stokes equations with an added scalar Y_i and source terms \dot{q} and $\dot{\omega}_i$, representing the mass fraction for species i , energy release rate, and species production rate, respectively,

$$\frac{\partial \rho}{\partial t} = -\nabla \cdot (\rho \mathbf{V}) \quad (2.1)$$

$$\frac{\partial (\rho \mathbf{V})}{\partial t} = -\nabla \cdot (\rho \mathbf{V} \mathbf{V}) - \nabla P - \nabla \cdot \hat{\tau} \quad (2.2)$$

$$\frac{\partial E}{\partial t} = -\nabla \cdot ((E + P) \mathbf{V}) - \nabla \cdot (\mathbf{V} \cdot \hat{\tau}) - \nabla \cdot (K \nabla T) + \dot{q} \quad (2.3)$$

$$\frac{\partial (\rho Y_i)}{\partial t} = -\nabla \cdot (\rho Y_i \mathbf{V}) + \nabla \cdot (\rho D \nabla Y_i) + \dot{\omega}_i \quad (2.4)$$

$$\hat{\tau} = \rho \nu \left(\frac{2}{3} (\nabla \cdot \mathbf{V}) \mathbf{I} - (\nabla \mathbf{V}) - (\nabla \mathbf{V})^\dagger \right). \quad (2.5)$$

Here, t is time, ρ is density, P is pressure, E is total energy, \mathbf{V} is the velocity vector, T is temperature, K is thermal conductivity, and \mathbf{I} is the identity matrix. We consider Newtonian fluids for which $\hat{\tau}$ is the stress tensor as shown in Eq. (2.5) and ν is the kinematic viscosity. The superscript \dagger denotes the matrix transpose.

The total energy is calculated according to

$$E = \rho e + \frac{1}{2}\rho \mathbf{V} \cdot \mathbf{V}. \quad (2.6)$$

Here, e is the specific internal energy,

$$e = \frac{P}{\rho(\gamma - 1)}, \quad (2.7)$$

which assumes a perfect, ideal gas using the ideal gas equation of state,

$$P = \rho \frac{R_u}{M_w} T, \quad (2.8)$$

where R_u is the universal gas constant and M_w is the molecular weight.

2.2.2 Chemical-diffusive model

Chemical reaction effects are modeled here by a calibrated CDM, which uses an Arrhenius function,

$$\dot{\omega} = A\rho Y \exp(-E_a/R_u T), \quad \dot{q} = q\dot{\omega} \quad (2.9)$$

to regulate \dot{q} in Eq. 2.3 and $\dot{\omega}_i$ in Eq. 2.4. The parameters used in the Arrhenius function are the pre-exponential factor A , progress variable Y , and activation energy E_a . The heat release is given by q . The variables A , E_a , and q are calibrated so that the flame properties (flame speed, thickness, and temperature) of ethylene-air

and heptane-air mixtures are reproduced within a Navier-Stokes computation. The calibration procedure is repeated over a range of stoichiometry, making the reaction parameters functions of equivalence ratio ϕ .

The CDM used here considers three species: fuel, oxidizer, and product. We assume a constant molecular weight M_w for all species and a constant specific heat ratio γ for all species and temperature. For ethylene-air mixtures, we assume M_w to be 28.5 g/mol and γ to be 1.35. For heptane-air mixtures, M_w is 30.6 g/mol and γ is 1.18. The diffusion coefficients (species diffusion, heat conduction, and viscosity) are assumed to have a temperature and density dependence.

The Arrhenius and diffusion parameters are tabulated and accessed within the computation through a table look-up according to the local ϕ . Details on the diffusion coefficients and the calibration procedure for the Arrhenius parameters are presented in the following section.

2.2.3 Temporal integration procedure

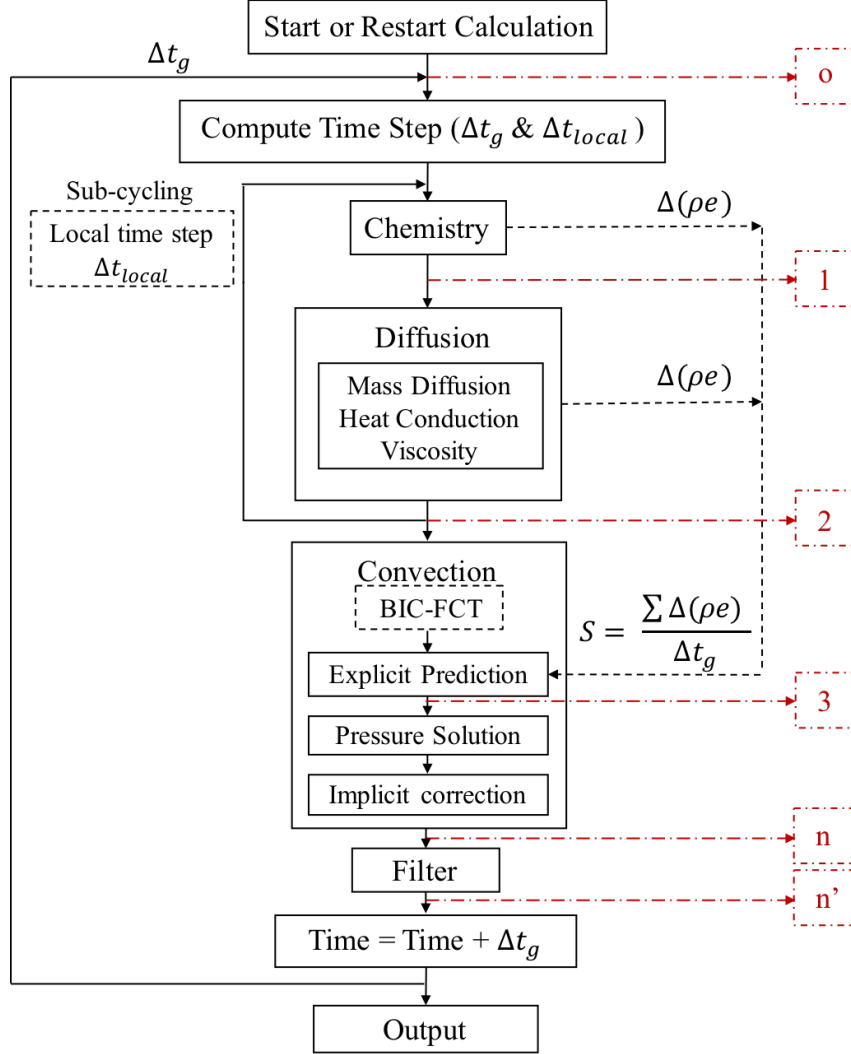


Figure 2.1: Flowchart of the coupling of the physical processes in one time-step. The sub-cycling procedure is changed from the prior paper [29] to include the effects of chemical reactions and heat release.

The chemical conversion is coupled with the diffusion and convection processes through the time-step splitting procedure. This means that, in one time step, the

chemistry, diffusion, and the convective processes are calculated sequentially. The temporal integration procedure of BIC with chemical reactions is summarized in Fig. 2.1. The subscript o represents the starting (or “old”) value, and subscripts 1, 2, 3, n and n' denote stages where the variables need to be updated. The total procedure is now explained step by step.

Step (1) Calculate the time steps

The global time step Δt_g used to advance from time t^o to $t^o + \Delta t_g$ is determined using the convective CFL condition,

$$\Delta t_g = CFL_{fluid} \min(\Delta x/|v|), \quad (2.10)$$

where v is the fluid velocity, CFL_{fluid} is the Courant-Friedrichs-Levy (CFL) condition governed by the fluid velocity, and Δx is the width of a computational control volume. Each of the diffusive processes, including the Fickian mass diffusion, Fourier heat conduction, and Newtonian viscosity, however, has its own integration time step limit to ensure numerical stability. The required time steps from these nonconvective processes can be smaller than the Δt_g . If this is the case, subcycling is applied for the integration of the chemistry or diffusion using a smaller local time step Δt_{local} within the required stability limit.

The time step used in the reaction integration, Δt_{chem} , is restricted to avoid integration error. Here, the maximum allowed size of the reaction time step is restricted so that it is never larger than the time required for a stoichiometric premixed flame to propagate through 30% of a computational cell,

$$\Delta t_{chem} = \frac{\Delta x}{30 \cdot S_L(\phi = 1)}. \quad (2.11)$$

Step (2a) Compute the chemical conversion, energy release, and physical diffusion effects – no subcycling required

When no subcycling is required, use the global time step Δt_g to compute the conversion of species, the related energy changes, and integrate the diffusion processes. In this step, we first compute the changes in species concentration, ρY_i , and total energy, E , due to chemical conversion and energy release. The rate of conversion for species i is governed by $\dot{\omega}_i$ in Eq. (2.4). After computing the change in species concentration, the species mass fraction is updated from Y_{i_o} to Y_{i_1} . The rate of chemical energy release is governed by \dot{q} in Eq. (2.5). The update of energy is discussed in the following paragraphs. In this paper, $\dot{\omega}_i$ and \dot{q} are computed using the CDM. Other chemical models, however, could also be used.

When the global time step is large, there can be an unphysically large change in pressure during the energy release process. One way to deal with this problem is to modify the procedure after the chemical energy release. We recommend temporarily removing the change of total internal energy and storing it as a temporary variable, $S = \Delta(\rho e)/\Delta t_g$. The quantity S will be dealt with during the convection process, as described in Step 3. The total internal energy at this stage remains unchanged after the chemical energy release. After computing the temporary variable S and the changes in species concentration, the pressure P_1 is equal to P_o and the total energy E_1 is updated using the old internal energy ($P_o/(\gamma - 1)$).

Next, we compute the changes in the momentum, total energy, and species concentration from the diffusion processes in Eqs. (2.2-2.5). These changes can be computed by integrating the diffusion fluxes using either an explicit or implicit time integration method. The computations described in this paper use one-step, Euler, explicit integration with second-order, three-point central spatial discretization.

After computing the changes from the diffusion processes, the update of variables is similar to those used before. That is, the change of total internal energy due to diffusion processes is extracted and accumulated in the variable S . For consistency, the total internal energy temporarily keeps the value it had at the beginning of the global time step. The pressure P_2 is accordingly equal to P_o . The momentum $\rho_2 V_2$ at stage 2 is updated from the diffusion flux integration. The total energy is again updated using the old internal energy ($P_o/(\gamma - 1)$) and the new kinetic energy ($\rho_2 V_2^2/2$). The total energy at stage 2 is then

$$E_2 = \frac{P_o}{\gamma - 1} + \frac{\rho_2 V_2^2}{2}. \quad (2.12)$$

Step (2b) Compute the chemical conversion, energy release, and physical diffusion effects – subcycling required

If any of the diffusion and reaction time-step limits, Δt_{local} computed in Step 1, are smaller than Δt_g , then subcycling of the chemical and diffusion processes is required. Subcycling these processes needs careful treatment to avoid infinitely fast reactions. In reality, diffusion and reaction processes occur simultaneously within the flame and strongly influence each other. Here, staggered integration is performed

to include the dynamics between the diffusion and reaction processes. This is done by first integrating the chemistry process as done in Step 2a, except now, we use Δt_{local} instead of Δt_g . Then the diffusion processes are integrated for the same Δt_{local} . The update of the variables and accumulation of energy changes in S is the same as in Step 2a. This procedure is repeated until the accumulated local time steps reach the global time step.

Step (3) Compute the convective transport using BIC: explicit predictor

Now perform the explicit prediction stage of the BIC algorithm for the predicted convective fluxes. This step and the following step for implicit correction are essentially the same as the procedure described in [29]. Here, we repeat the equations to clarify the usage and update of variables.

1. Solve for predicted density ρ' , species concentration $\rho'Y'_i$, and momentum $\rho'\vec{V}'$:

$$\frac{\rho' - \rho_2}{\Delta t_g} = -\nabla \cdot (\rho_2 \mathbf{V}_2) \quad (2.13)$$

$$\frac{\rho'Y'_i - \rho_2Y_{i2}}{\Delta t_g} = -\nabla \cdot (\rho_2Y_{i2} \mathbf{V}_2) \quad (2.14)$$

$$\frac{\rho'\mathbf{V}' - \rho_2\mathbf{V}_2}{\Delta t_g} = -\nabla \cdot (\rho_2\mathbf{V}_2\mathbf{V}_2) - \nabla P_2 \quad (2.15)$$

Use a monotone method (here, FCT with one-step time integration) to solve for predicted density ρ' , species concentration $\rho'Y'_i$, and momentum $\rho'\vec{V}'$ with the global time step Δt_g . The variables with subscript ‘2’ are the values at stage 2 in Fig. 2.1, which is after Step 2 for diffusion and reaction effects.

2. Solve for intermediate energy \bar{E} :

$$\frac{\bar{E} - E_2}{\Delta t_g} = -\nabla \cdot (E_2 + P_2) [\omega \mathbf{V}' + (1 - \omega) \mathbf{V}_2] + S \quad (2.16)$$

Again, use FCT with the one-step time integration with the same Δt_g as in step 1 to solve for an intermediate energy \bar{E} . Same as in step 1, the variables with subscript ‘2’ are the values at stage 2, after Step 2. Note that the source term S here includes the accumulated internal energy change due to the chemistry and diffusion processes.

The stage after the explicit predictor is denoted as stage 3 in Fig. 2.1. The density ρ_3 , momentum $\rho_3 \vec{V}_3$, and energy E_3 have the output values from the monotone algorithm solver, which are ρ' , $\rho' \vec{V}'$, and \bar{E} respectively. The pressure should not be updated from the original value at the beginning of the time step, P_o . The temperature and velocity are yet not updated to save computational effort as they will not be used in the next corrector step.

Step (4) Compute the convective transport using BIC: implicit corrector

Solve the elliptic equation (Eq. 2.17) for the pressure correction δP . In this equation, variables without subscript 2 are from stage 3, after the explicit prediction.

$$\frac{\delta P}{(\gamma - 1)\omega \Delta t_g} - \omega \Delta t_g \nabla \cdot \left(\frac{E_2 + P_2}{\rho'} \right) \nabla \delta P = \frac{\bar{E} - E_2}{\Delta t_g} - \frac{\rho' \mathbf{V}'^2 - \rho_2 \mathbf{V}_2^2}{2\Delta t_g} \quad (2.17)$$

Then correct the momentum, total energy and pressure using Eqs. 2.18, 2.19, and

2.20:

$$\rho^n \mathbf{V}^n = \rho' \mathbf{V}' - \Delta t_g \nabla \delta P \quad (2.18)$$

$$E^n = \frac{\omega P_o + \delta P}{(\gamma - 1)\omega} + \frac{1}{2} \rho^n \mathbf{V}^{n2} \quad (2.19)$$

$$P^n = P_o + \delta P \quad (2.20)$$

At this stage ‘ n ’, all of the flow properties are synchronized to the new time step $t^o + \Delta t_g$.

Step (5) Apply a high-frequency filter, if necessary

A high-frequency filter could be applied here after all the integration processes to remove spurious oscillations during the pressure correction when necessary. As done in [29], we use an extra FCT step as the spatial filter. This is done by passing the conservative variables through an extra FCT step with no pressure gradients and the velocity set to zero. This stage is denoted as ‘ n' ’ in Fig. 2.1.

In summary, chemical reactions and heat release were added to the BIC algorithm. This was done by solving additional conservation equations 2.4 which solve the time rate of change for species concentration and by adding a source term in the energy equation 2.3 to account for changes in energy due to heat release. To include these additional equations and source terms to the BIC integration procedure, we changed the sub-cycling integration for diffusion described in the prior paper [29]. This procedure can be used as a guide to include other source terms and physical processes into the BIC integration procedure.

2.3 Chemical-Diffusive Model

Reactive-flow simulations have benefited significantly from the progress made in algorithms and methodologies that solve the governing fluid equations and chemical reactions. There is a large body of ongoing research that addresses these areas, including the difficulty of coupling fluid dynamics and combustion models. A significant portion of this difficulty arises from the orders-of-magnitude variation in temporal and spatial scales within and between the combustion and fluid processes.

The combustion process is often modeled using detailed and skeletal chemical mechanisms, which are important for resolving effects due to chemical kinetics but generally require including many chemical species and reactions. These species and reactions can have large variations in transport properties and reaction rates within a single mechanism, introducing stiffness to the time-step integration. Furthermore, resolving the transport of n species requires solving n equations, in addition to the conservation laws of mass, momentum, and energy. These challenges can make reactive flow computations which use detailed mechanisms prohibitively expensive, even at small scales.

To reduce the numerical cost, a simplified combustion model can be an attractive alternative. This is especially true when the effects of heat release are the primary interest rather than the details of the chemical kinetics. The rate of heat release, in the simplest form, can be regulated by the conversion rate (i.e., the reaction rate) of reactants to products. A one-step, irreversible reaction can be used to represent this conversion, which might be governed by a rate that has an Arrhenius

form,

$$\dot{\omega} = A \exp(-E_a/R_u T) C_f^a C_o^b \quad (2.21)$$

where $\dot{\omega}$ is the reaction rate, E_a is the activation energy, R_u is the universal gas constant, T is the temperature, C_f and C_o are the concentrations of fuel and oxidizer, respectively, and a and b are the reaction orders. The heat release rate is then given by $q\dot{\omega}$, where q is the heat of reaction. This approach was shown to work well for matching low-speed combustion wave properties of a mixture. One early example is by Westbrook and Dryer [50], who investigated the use of such a simplified single-step mechanism to model the slow burning of hydrocarbons and oxygen. They showed that one could match laminar flame speeds and flame temperatures from premixed experiments by calibrating and optimizing the parameters used in Eq. 2.21. Fernandez-Tarrazo et al. [51] demonstrated the capability of the single-step model to predict the structure of non-premixed, diffusion flames, along with the correct flame temperatures and speeds of hydrocarbon-air premixed mixtures, by allowing for the heat of reaction and activation energy to vary according to the equivalence ratio.

Although these examples are for diffusion-limited combustion waves, simplified mechanisms have also been successful for matching detonation properties. The first such method is the induction parameter model (IPM) [52] by Oran et al., which allowed heat release in a control volume based on the local state of the reaction and thermodynamic variables. Though successfully used for modeling detonations, the formulation of the IPM does make sense for computing flames.

Following the IPM, there has been a body of work (we list a selected few: [48, 53, 54, 55]) which developed and used a simplified combustion model that could be used for both flames and detonations. This model was called the chemical-diffusive model (CDM), which also uses the functional form of a single-step Arrhenius rate to regulate the heat release. The CDM is based on a calibration of the parameters for the Arrhenius rate, along with the heat of combustion and heat diffusivity, such that the properties of *both* the subsonic flame and supersonic detonation are reproduced in a reactive flow computation. These properties have traditionally been the premixed flame speed, flame thickness, detonation speed, detonation half-reaction thickness, and the adiabatic constant-pressure and constant-volume temperatures. The CDM has been applied to the simulation of deflagration-to-detonation transitions (DDT) for mixtures with single and, more recently, variable stoichiometry [56, 57]. The principles behind the calibration of the CDM are discussed further in [48, 56] and recently, an automated procedure for this calibration process was introduced in [57].

Prior applications of the CDM, however, focused on premixed modes of combustion, where combustion waves are limited by the amount of compression from a shock wave or by the diffusion of heat from products to reactants. In this work, we apply a simplified CDM calibration procedure, which considers only premixed flames and forgoes matching the detonation properties. We repeat this procedure for varying values of the stoichiometry and then, later in Chapter 4, use the calibrated CDM in Navier-Stokes computations of non-premixed diffusion flames.

The CDM used here considers three species: fuel, oxidizer, and product. We

assume a constant molecular weight M_w for all species and a constant specific heat ratio γ for all species and temperature. For ethylene-air mixtures, we assume M_w to be 28.5 g/mol and γ to be 1.35. For heptane-air mixtures, M_w is 30.6 g/mol and γ is 1.18.

2.3.1 Diffusion Parameters

The thermal conductivity K in Eq. 2.3 is obtained from the mixture-averaged transport properties of the Lu and Law mechanism [58] for heptane-air mixtures with a temperature and pressure of 372 K and 1 atm and the Wang and Laskin mechanism [59] for ethylene-air mixtures with a temperature of 298 K and the same pressure. The values of K are obtained as a function of equivalence ratio ϕ which is computed as

$$\phi = OF_{st} \frac{Y_{fuel}}{Y_{air}} \quad (2.22)$$

where OF_{st} is the stoichiometric air to fuel mass ratio, Y_{fuel} is the fuel mass fraction and Y_{air} is the air mass fraction. The mixture averaged values of K are used to compute the thermal diffusivity κ using $\kappa = K/\rho C_p$, where C_p is the heat capacity at constant pressure given by

$$C_p = \frac{R\gamma}{\gamma - 1}, \quad (2.23)$$

with $R = R_u/M_w$. The thermal diffusivity is modeled to have a temperature dependence,

$$\kappa = \kappa_0 \frac{T^n}{\rho}. \quad (2.24)$$

The subscript 0 refers to a reference state with temperature T_0 and pressure P_0 . The exponent n is chosen to be 0.7, consistent with prior applications of the CDM [48, 53, 54, 60]. For heptane-air mixtures, we choose $T_0 = 372$ K, the evaporation temperature of liquid heptane at 1 atm, and for ethylene-air, we choose $T_0 = 298$ K. Both mixtures use $P_0 = 1$ atm. The reference thermal diffusivity κ_0 is computed from Eq. 2.24 and tabulated as a function of ϕ . We show κ_0 in Fig. 2.2 for heptane-air (dashed-dot blue line) and ethylene-air (solid black line) mixtures as a function of equivalence ratio ϕ .

The mass diffusivity D in Eq. 2.4 is computed using a unity Lewis number approximation. The viscosity ν in Eq. 2.5 is computed from the Prandtl number which is assumed to be 0.7.

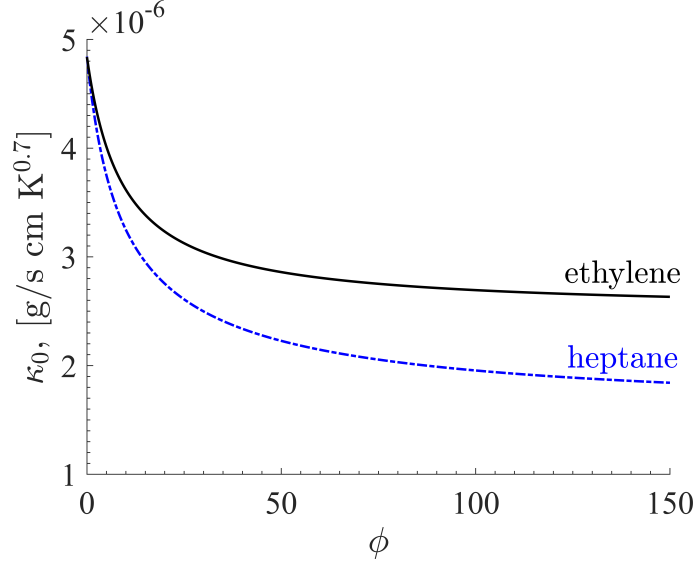


Figure 2.2: Reference heat diffusivity versus equivalence ratio for heptane-air (dashed-dot blue line) and ethylene-air (solid black line) mixtures.

2.3.2 Reaction Parameters

The heat release rate q is calibrated according to

$$q(\phi) = (T_b(\phi) - T_0)C_p, \quad (2.25)$$

where q is shown as a function of ϕ and T_b is the adiabatic flame temperature for a premixed laminar flame with equivalence ratio ϕ . Here, the adiabatic flame temperature is obtained using Cantera [61] with the Lu and Law mechanism [58] for heptane-air and the Wang and Laskin mechanism [59] for ethylene-air. The constants T_0 and C_p are the same as used in the diffusion parameters. The resulting normalized values of heat release are shown in Fig. 2.3 for heptane-air (dashed-dot

blue line) and ethylene-air (solid black line) mixtures.

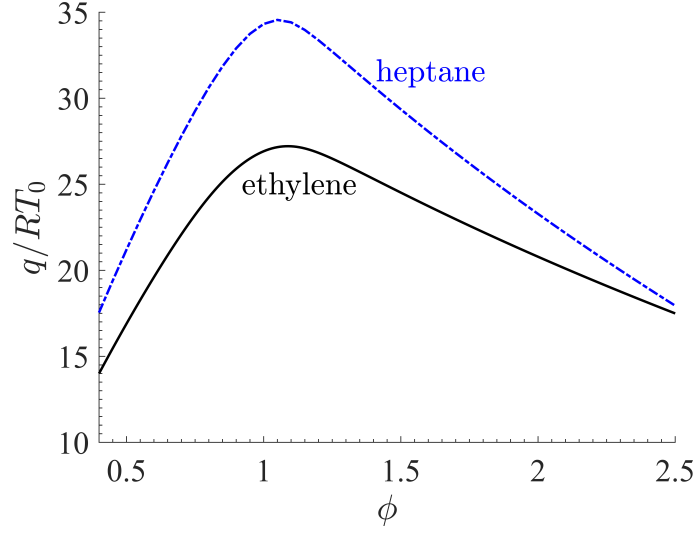


Figure 2.3: Normlized heat release versus equivalence ratio for heptane-air (dashed-dot blue line) and ethylene-air (solid black line) mixtures.

The burning properties used to calibrate A and E_a in Eq. 2.9 are the premixed laminar flame speed S_L and thickness Δx_L . The values for S_L and Δx_L can be obtained from experimental data or from detailed chemistry calculations. Here, we use detailed chemistry calculations as done for the flame temperature for both heptane-air and ethylene-air to obtain S_L and Δx_L as a function of ϕ from 0.35 to 2.5. The definition of Δx_L used here is

$$\Delta x_L = \frac{T_b - T_0}{\max |dT/dx|}, \quad (2.26)$$

where x is position and $\max |dT/dx|$ is the maximum temperature gradient in the flame.

The E_a - A calibration is carried out by solving an inviscid, one-dimensional

balance of heat conduction and convection with heat release for a single ϕ , assuming unity Lewis number,

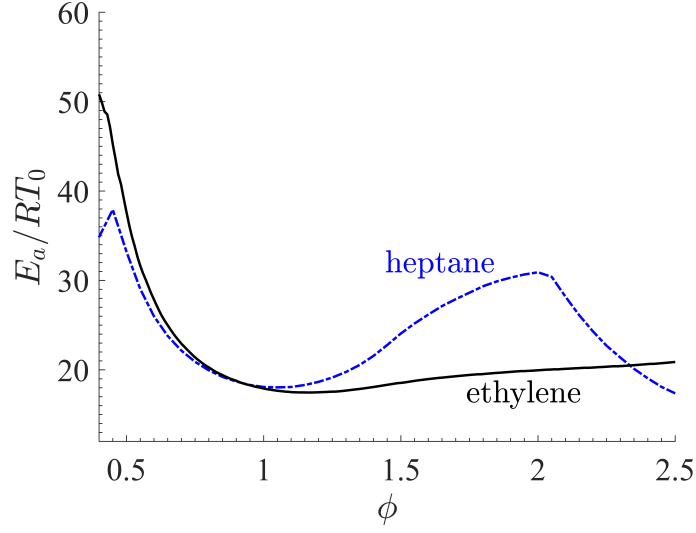
$$\frac{d}{dx} \left(K(\phi) \frac{dT}{dx} \right) = \rho \left(U_l C_p \frac{dT}{dx} - q(\phi) \dot{\omega}(\phi) \right). \quad (2.27)$$

Here, U_l is the fluid velocity in the reference frame of the flame. The values for K and q are obtained from Figs. 2.2 and 2.3 for a value of ϕ . For this ϕ , the parameters E_a and A in the reaction rate $\dot{\omega}$ are iteratively varied until the resulting laminar flame speed and thickness from the flame computed by Eq. 2.27 matches the S_L and Δx_L from the chemical equilibrium software. This process is repeated over a range of ϕ , generating a range of E_a and A which are functions of ϕ . The resulting calibrated values of E_a and A are presented in Fig. 2.4.

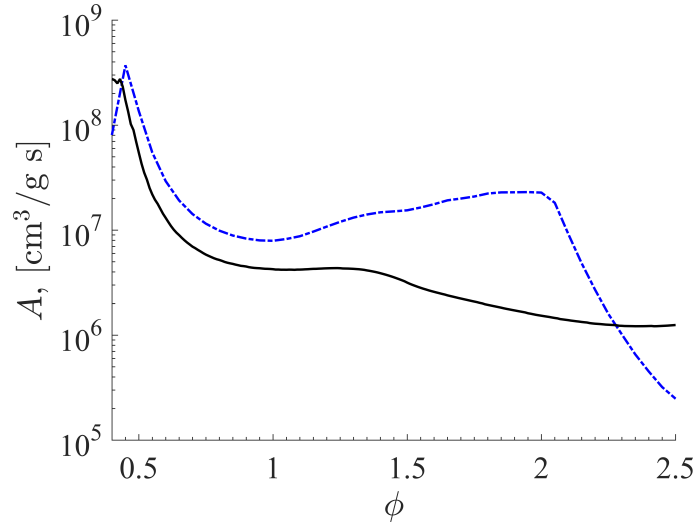
The integration procedure for Eq. 2.27 for a single ϕ is described in [48]. The main difference between the calibration used here and in [48] is that here, the values of κ_0 and q are found independently from E_a and A . This means that in this work, κ_0 and q are not changed during the E_a - A calibration procedure.

2.3.3 Computing Progress Variable

After determining A and E_a , to compute the reaction rate $\dot{\omega}$, we need to compute the progress variable Y . Here, to track the progress of the reaction, we need Y to scale from 1 to 0 in all cases of fuel-rich, fuel-lean, and stoichiometric mixtures. If the mixture is fuel-rich, we use the oxidizer mass fraction to compute Y since the oxidizer is completely consumed at the end of the reaction. This is



(a) Activation energy versus equivalence ratio.



(b) Pre-exponential factor versus equivalence ratio.

Figure 2.4: Optimized CDM parameters for ϕ in the range of 0.35 to 2.50 for heptane-air with $T_0 = 372$ K and ethylene-air with $T_0 = 298$ K.

expressed as

$$Y = \frac{Y_{air}}{Y_{air,u}} \quad \text{if } \phi > 1, \quad (2.28)$$

where $Y_{air,u}$ is the mass fraction oxidizer before any burning occurred. If the mixture is fuel-lean, we use the fuel mass fraction since the fuel is completely consumed at

the end of the reaction. This is expressed as

$$Y = \frac{Y_{fuel}}{Y_{fuel,u}} \quad \text{if } \phi < 1, \quad (2.29)$$

where $Y_{fuel,u}$ is the mass fractions of fuel before any burning occurred. In the case of a stoichiometric mixture, Eqs. 2.28 and 2.29 are the same.

To compute what the reactant mass fractions were before burning, we assume burning occurs stoichiometrically and then use this assumption to find how much of each reactant species, fuel and oxidizer, contributed to the formation of product. This amount is added to the existing reactant mass fraction to obtain $Y_{i,u}$, where i is a reactant species. This can be expressed as

$$Y_{air,u} = Y_{air} + \frac{OF_{st}}{OF_{st} + 1} Y_{Pr}, \quad Y_{fuel,u} = Y_{fuel} + \frac{1}{OF_{st} + 1} Y_{Pr}. \quad (2.30)$$

2.3.4 Computing species conversion and heat release

We now have all reaction and diffusion parameters, E_a , A , q , and κ_0 , as functions of ϕ as shown in Figs. 2.4, 2.3. and 2.2. These can be tabulated into a lookup table to use in solving the reactive NS equations. In the NS calculation, to compute the species conversion rates and heat release rate, we must first determine the local ϕ which is computed using the mass fractions obtained from Eqs. 2.30,

$$\phi = OF_{st} \frac{Y_{fuel,u}}{Y_{air,u}}, \quad (2.31)$$

then use this ϕ to access the look-up table.

Computing the species conversion rates, $\dot{\omega}_{fuel}$, $\dot{\omega}_{air}$, and $\dot{\omega}_{Pr}$, requires special consideration because of how the calibration procedure is performed. The calibration computes premixed 1D flames using Eq. 2.27 which uses $\dot{\omega}$ to convert reactant to product. For any ϕ , this $\dot{\omega}$ converts all reactants to “product” which implicitly groups any remaining reactant with the “product”. This means the “product” generated by $\dot{\omega}$ is composed of two parts: the “actual” product, Y_{Pr} , from stoichiometric burning and the leftover reactant species (fuel for rich mixtures and oxidizer for lean mixtures). We decompose $\dot{\omega}$ into conversion rates for actual product and reactants by assuming stoichiometric burning for two situations: fuel-rich and fuel-lean mixtures. For fuel-rich mixtures, conversion rates for Y_{Pr} , Y_{fuel} , and Y_{air} are given by

$$\dot{\omega}_{fuel} = -\frac{1}{OF_{st} + \phi}\dot{\omega}, \quad \dot{\omega}_{air} = -\frac{OF_{st}}{OF_{st} + \phi}\dot{\omega}, \quad \text{and} \quad \dot{\omega}_{Pr} = \frac{1 + OF_{st}}{OF_{st} + \phi}\dot{\omega}, \quad (2.32)$$

and for fuel-lean mixtures,

$$\dot{\omega}_{fuel} = -\frac{\phi}{OF_{st} + \phi}\dot{\omega}, \quad \dot{\omega}_{air} = -\frac{\phi OF_{st}}{OF_{st} + \phi}\dot{\omega}, \quad \text{and} \quad \dot{\omega}_{Pr} = \frac{\phi(1 + OF_{st})}{OF_{st} + \phi}\dot{\omega}. \quad (2.33)$$

In the case of $\phi = 1$, the above Eqs. 2.32 and 2.33 become equivalent.

Chapter 3: Test Problems

We apply the BIC-FCT algorithm to five successively more complex test problems, each testing a different property or behavior of low-speed, reactive flows. We first simulate a series of one-dimensional (1D), premixed, laminar flames to determine whether the BIC-FCT algorithm with the CDM can reproduce the correct flame properties. Second, we compute two-dimensional, counter-flow diffusion flames to test the ability of BIC-FCT to compute non-premixed flames. Third, a two-dimensional triple flame is then simulated to test the ability of the algorithm to compute flames with complex transport and heat release structures. Fourth, an unsteady, co-flow diffusion flame is computed to test boundary conditions and whether BIC-FCT with the CDM can compute a lifted flame. Lastly, we compute a turbulent, three-dimensional flow with unsteady combustion by simulating a fire whirl.

For these applications, the entire algorithm is incorporated into the BoxLib [62] adaptive mesh refinement framework which provides the software structure for parallelization and grid refinement. All computations presented in this work employ a fixed, Cartesian mesh with no adaptive refinement. The BoxLib [62] library also provides a multigrid solver for elliptic equations, which we use to solve Eq. 2.17.

The default solver settings are used, with relaxation performed using the red-black Gauss-Seidel smoother, the coarse grid exact solver using the biconjugate gradient stabilized algorithm, and restriction and interpolation between fine and coarse grids using a V-cycle.

The convective, hyperbolic fluxes in the explicit predictor step are computed using an unsplit version of fourth-order flux-corrected transport (FCT) [46, 49]. Flux limiting is performed using the Zalesak [63] multidimensional limiter with the monotone correction by DeVore [64].

All test problems in this paper use an implicitness parameter $\omega = 1$, which is appropriate for low-Mach-number flows, and a CFL_{fluid} of 0.3. The filter is applied to all test problems. We use the fluid parameters for ethylene-air and heptane-air mixtures, shown in Section 2.2.2. The values for the chemical and diffusion parameters used here are presented in the Appendix.

3.1 One-dimensional, premixed, laminar flames

Simulations of 1D, premixed, laminar flames of heptane-air mixtures are performed to assess whether the BIC-FCT method can reproduce the flame properties that the CDM was calibrated to match. Here, we first compare BIC-FCT to explicit FCT using the flame profile from a stoichiometric heptane-air mixture. Then, the convergence of BIC-FCT is tested by varying the mesh size. Finally, we compare flame properties computed from BIC-FCT against those computed from chemical equilibrium software for heptane-air and ethylene-air mixtures over a range of equiv-

alence ratios.

3.1.1 Boundary and Initial Conditions

The boundary conditions, initial conditions, and computational mesh are shown in Fig. 3.1. The length of the domain is 100 mm long and is discretized with a uniform mesh with a cell size Δx . The initial pressure within the domain and the pressure at the outflow boundary condition are 1 atm. At the inflow boundary condition, the velocity V_x is set to be the ideal laminar flame speed S_L for an inflow mixture with equivalence ratio ϕ , ensuring the flame remains in the domain. The temperature T at the inflow is $T_0 = 372$ K, which is the evaporation temperature of liquid heptane at 1 atm. The fuel and oxidizer mass fractions (Y_F and Y_{Ox}) at the inflow are defined according to a specified equivalence ratio ϕ . The variable OF is the stoichiometric oxidizer to fuel mass ratio, which is 15.075 for heptane-air and 14.68 for ethylene-air. All other primitive variables on both boundaries are extrapolated using a zero-gradient Neumann condition.

The initial condition in the domain is divided into two equal parts. The left side is initialized with unburned reactants with a temperature of T_0 and a velocity of S_L . The right side is initialized with all product which has a temperature of $T_2 = 2000$ K and velocity of $S_L \cdot (T_2/T_0)$.

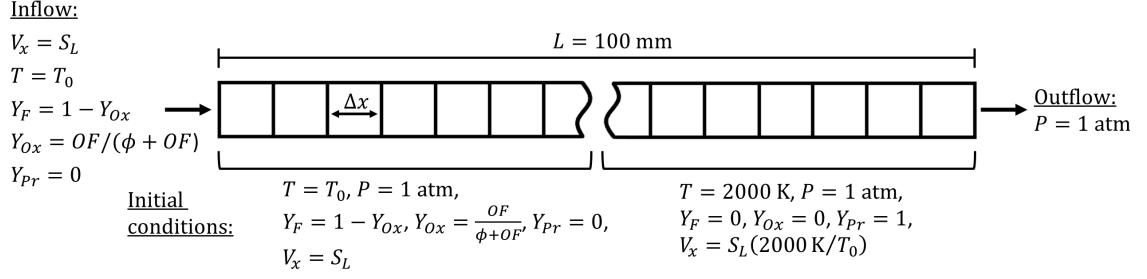


Figure 3.1: A schematic of the boundary conditions, initial conditions, and computational mesh used in the 1D, steady-state, premixed, laminar flame computations.

3.1.2 Comparison of explicit FCT and BIC-FCT

We first compare BIC-FCT with explicit FCT by solving the 1D flame for a stoichiometric heptane-air mixture. The cell size Δx for this comparison is 0.05 mm. The resulting, steady-state temperature profiles are shown in Fig. 3.2 with the explicit FCT result shown as blue squares and the implicit BIC-FCT result shown as red circles. The temperature profiles in Fig. 3.2 show that the steady-state explicit FCT and BIC-FCT solutions are essentially the same.

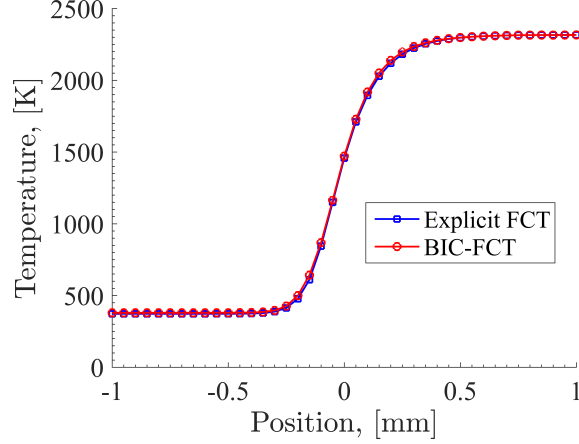


Figure 3.2: A comparison of a one-dimensional, heptane-air, stoichiometric, premixed, laminar flame computation using the explicit FCT (blue square) and the implicit BIC (red circles) algorithms.

Here, explicit FCT uses an average time-step size of $\Delta t = 2.6 \times 10^{-8}$ s which is determined using a CFL condition based on the acoustic speed, CFL_{wave} ,

$$\Delta t = CFL_{wave} \min \left(\frac{\Delta x}{|v| + a} \right), \quad (3.1)$$

where a is the sound speed and CFL_{wave} is 0.9. BIC-FCT achieves a CFL_{wave} of 125 using an average time-step size of 3.5×10^{-6} s, which is 135 times larger than the explicit time step. The average processor time per time step on a Intel Ivy Bridge 2.2 GHz processor using a single core is 0.0433 s for explicit FCT and 0.127 s for BIC-FCT. Although BIC-FCT requires three times more processing time per time step because of the additional subcycling and convergence of the elliptic solver, it is 45 times faster overall than explicit FCT to reach the same physical time in the

computation.

3.1.3 Convergence test

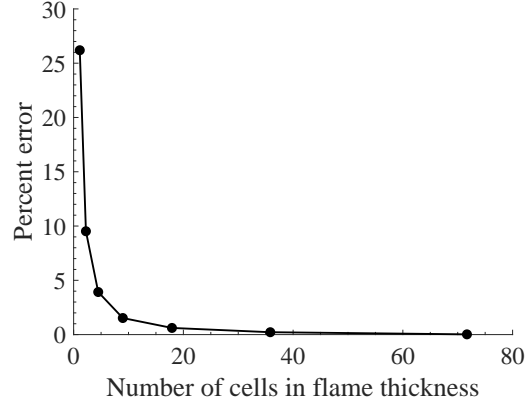


Figure 3.3: The error in flame speed from BIC-FCT using the CDM with varying resolution for stoichiometric, heptane-air flame, shown on the horizontal axis as the number of cells within the ideal flame thickness (0.28 mm). The error compares against the ideal flame speed of 65.51 cm/s.

The convergence properties of BIC-FCT were tested by changing the cell size Δx . Figure 3.3 shows the comparison of the flame speed as computed from BIC-FCT ($S_{L,BIC}$) and the ideal flame speed (S_{Lideal}) the CDM was calibrated to match. The percent error is computed by finding the difference between $S_{L,BIC}$ and S_{Lideal} and then dividing that difference by the S_{Lideal} . This is expressed as

$$\text{Percent error} = 100 \cdot \frac{S_{L,BIC} - S_{Lideal}}{S_{Lideal}} \quad (3.2)$$

This error is evaluated for different Δx which is shown in Fig. 3.3 as the number of cells within the ideal flame thickness. Here, the ideal flame speed is 65.51 cm/s and the ideal flame thickness is 0.028 mm.

From Fig. 3.3, we find that approximately 4 cells within the flame thickness is sufficient to resolve the flame with less than 5% error, consistent with prior work using the CDM [48]. As the cell size is further decreased, the BIC-FCT flame speed converges to the ideal CDM calibrated value. Regardless of the cell size, the calculations compute the correct flame temperature of 2317 K.

3.1.4 Varying Stoichiometry

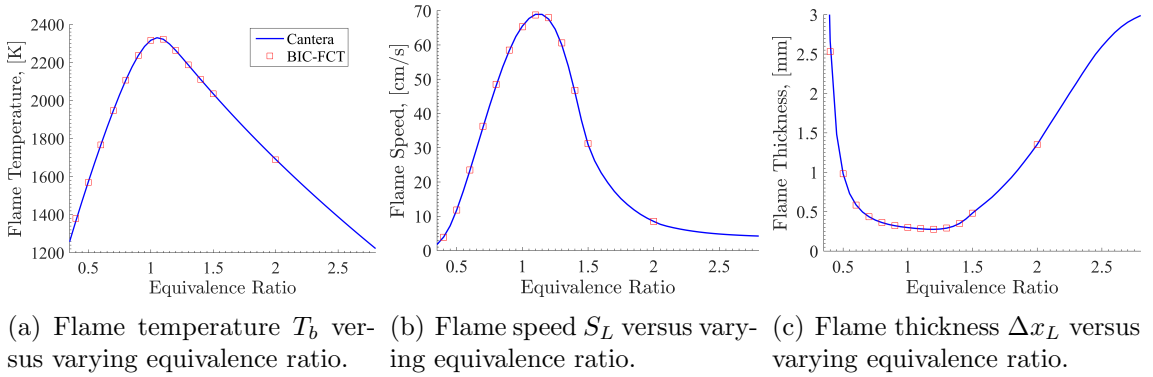
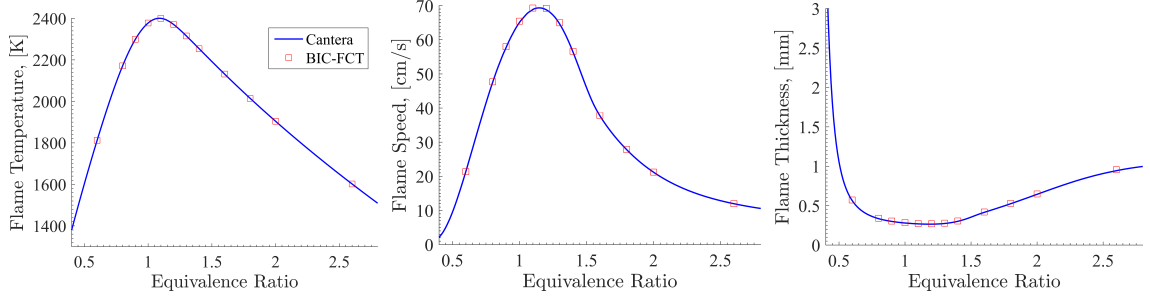


Figure 3.4: A comparison of flame temperature, speed, and thickness for heptane-air mixtures. Blue lines are computed from Cantera [61] with the 188-species n-Heptane Lu and Law [58] mechanism. Red squares are computed using BIC-FCT with the calibrated CDM as the chemical model.

Additional simulations were carried out for heptane-air and ethylene-air mixtures with each case using a different ϕ , varied from 0.35 to 2.0. The computational setup is the same as described in Section 3.1.2 with a few differences. Each case varies ϕ and the cell size Δx so that at least 10 cells are within the flame thickness for each ϕ . For heptane-air, the resulting steady-state flame temperature, flame speed,



(a) Flame temperature T_b versus varying equivalence ratio. (b) Flame speed S_L versus varying equivalence ratio. (c) Flame thickness Δx_L versus varying equivalence ratio.

Figure 3.5: A comparison of flame temperature, speed, and thickness for ethylene-air mixtures. Blue lines are computed from Cantera [61] with the Wang and Laskin [59] mechanism. Red squares are computed using BIC-FCT with the calibrated CDM as the chemical model.

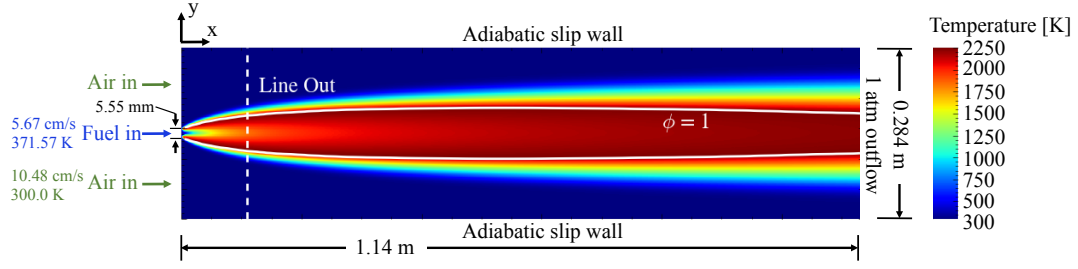
and flame thickness for each case are shown in Fig. 3.4 as red squares. The blue line shows values from Cantera and the Lu and Law mechanism [58] for heptane. For ethylene-air, The resulting steady-state flame temperature, flame speed, and flame thickness for each case are shown in Fig. 3.5 as red squares. The blue line shows values from Cantera using the Wang and Laskin mechanism [59] for ethylene-air.

For both fuels, the results show good agreement in all three flame properties across all equivalence ratios. The agreement with the temperature indicates the pressure correction is correctly redistributing the changes in energy due to heat release. The agreement in the flame speed and thickness shows that the subcycling process, described in Section 2.2.3, step 2, is able to correctly capture the coupling between diffusion and reaction processes of premixed flames.

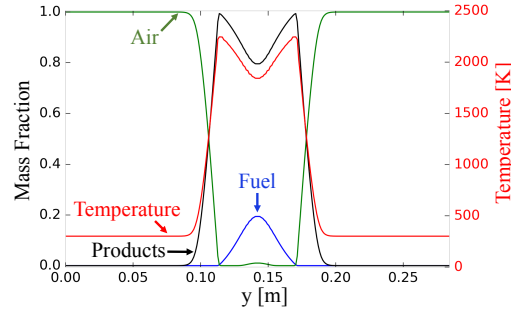
3.2 Two-dimensional coflow diffusion flame

We now assess whether the calibration approach for the chemical-diffusive model taken in Chapter 2 can indeed compute a non-premixed flame by simulating a two-dimensional, coflow diffusion flame. The boundary conditions and domain size are shown in Fig. 3.6a. Here, the inflow boundary on the left has heptane injected in the center with a constant temperature of 371.57 K and velocity of 5.67 cm/s. The inflow also has a parallel coflow of air with a temperature of 300 K and a faster velocity of 10.48 cm/s. The outflow boundary on the right is set to be a constant pressure of 1 atm, and the upper and lower walls are adiabatic symmetry planes. All other primitive variables at the inflow and outflow boundaries are extrapolated using a zero-gradient Neumann condition. The domain is discretized using a uniform, Cartesian mesh with $\Delta x = 28.4/2056$ cm.

Figure 3.6a also shows the steady-state temperature contour with a solid white line corresponding to the stoichiometric mixture fraction, i.e. the flame sheet. In Fig. 3.6b, we show the temperature, air, fuel, and product mass fractions along the vertical dashed white line in Fig. 3.6a. The peak temperature and maximum product concentration are located where the fuel and air are mostly depleted, as expected for a diffusion flame. In Fig. 3.6a, the peak temperature occurs near the flame sheet throughout the entire flow-field, also as expected. Also, the peak temperature does not exceed the maximum adiabatic flame temperature, indicating the balance of heat conduction and heat release rate for this non-premixed flame performs qualitatively well. These results suggest that the CDM approach to combustion can at least



(a) Boundary conditions, domain size, and temperature contour of a 2D laminar coflow diffusion flame.



(b) The mass fractions of air, fuel, and product along with temperature along a line in the y -direction as indicated by the dashed vertical white line in (a) of this figure.

Figure 3.6: A steady state computation of a 2D, laminar, n-Heptane and air, coflow diffusion flame.

model the qualitative features of a non-premixed flame.

3.3 Two-dimensional counter flow diffusion flame

Counter-flow diffusion flames are a canonical configuration for studying the structure and characteristics of non-premixed flames. Here, the flame sits between two opposed jets of fuel and oxidizer. The resulting flowfield establishes a continuous removal of reactants from the flame through diffusive and convective transport. The removal of reactants competes against the reactant conversion rate by the flame, causing incomplete combustion and lower peak flame temperature. These highly

coupled processes within a simple, canonical configuration make the counter-flow diffusion flame a useful test problem for reactive flow algorithms.

3.3.1 Boundary and Initial Conditions

To simulate a counter-flow diffusion flame, we consider ethylene as the fuel and air as the oxidizer. A schematic of the boundary conditions and mesh are shown in Fig. 3.7a. We consider a two-dimensional square domain with sides that are 10 mm in length, with an inflow of ethylene from the left and air from the right. The inflow has a temperature of 298 K. In the first case presented, the inflow velocity is set to be 4 m/s (as illustrated in Fig. 3.7) whereas in the second case, the inflow velocity is changed to 3 m/s. All other primitive variables at the inflow boundaries are extrapolated using a zero-gradient Neuman condition. The upper and lower outflow boundary conditions extrapolate the first spatial derivative of the primitive variables that is orthogonal to the boundary, so that their second derivative is zero. This is expressed as

$$d^2b/dy^2 = 0, \quad (3.3)$$

where b is a primitive variable. The boundary pressure is extrapolated using a far-field gradient so that a mean pressure is maintained in the interior flow without imposing a strong adverse pressure gradient. This far-field gradient is defined as

$$\left. \frac{dP}{dy} \right|_{boundary} = \frac{P_{boundary} - P_{\infty}}{L}, \quad (3.4)$$

where $P_{boundary}$ is the pressure of the interior computational cell closest to the boundary, and P_{∞} is the far-field pressure, which we set to be 1 atm. The distance between the boundary and location of the far-field pressure is L , defined to be 100 mm for these simulations.

The initial condition consists of hot product gas across the entire domain with a temperature of 2000 K to provide a heat source for ignition. All of the initial product gas is convected out of the domain in the calculation.

The mesh is Cartesian and is refined around regions of the flow with temperature larger than 300 K. The coarsest cell size is 7.8125×10^{-2} mm and the finest cell size is 9.7656×10^{-3} mm. A zoomed view of the mesh refinement is shown in Fig. 3.7a.

3.3.2 Results

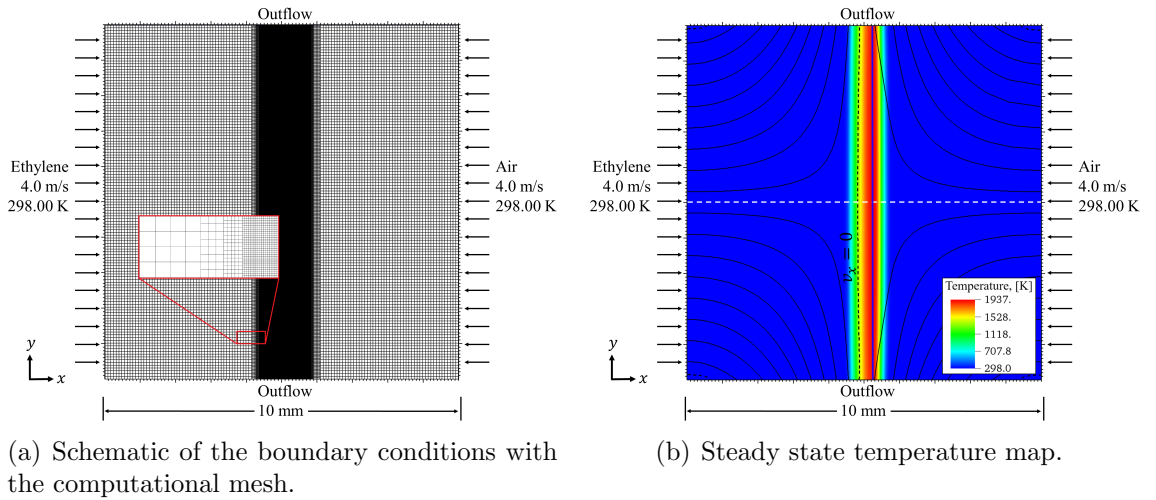


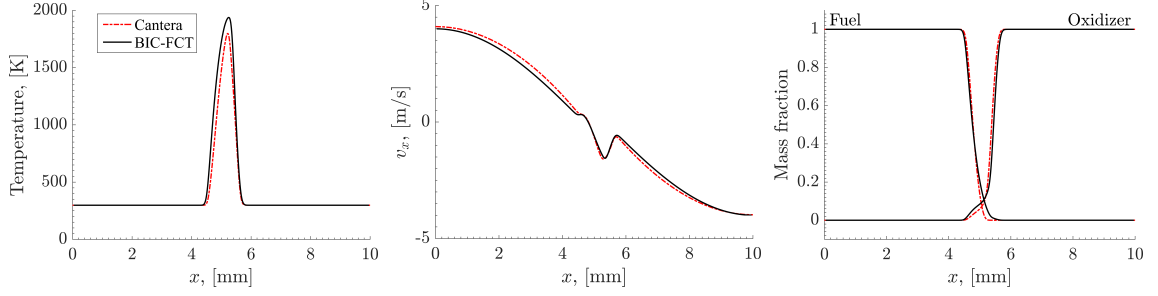
Figure 3.7: Simulation of a ethylene-air, counter-flow diffusion flame. The red box in (a) shows a zoomed in region of the mesh refinement.

Figure 3.7b shows the resulting temperature map at the steady-state for the

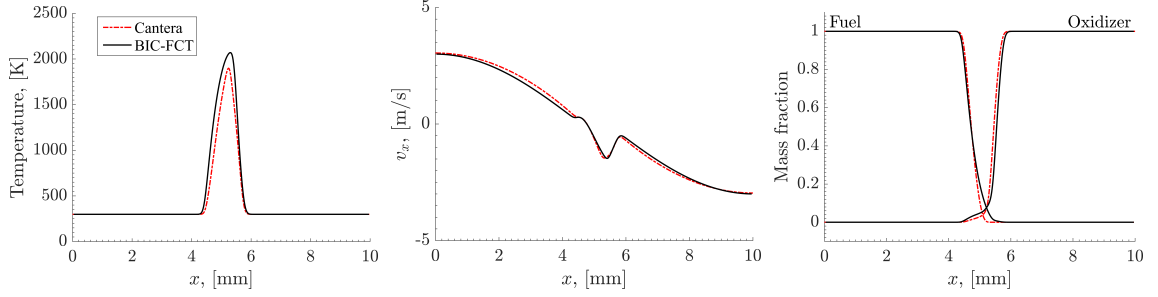
4 m/s inflow case with streamlines overlaid on top as black lines. The dashed vertical black line indicates the stagnation plane, where the x -velocity is zero. The vertical solid blue line shows the contour of $\phi = 1$. The result shows that the region of stoichiometric burning ($\phi = 1$ contour) is on the oxidizer side of the stagnation plane. This is expected in counter-flow diffusion flames with fuel-air mixtures that have stoichiometric air to fuel mass ratios larger than one. The peak temperature occurs along the $\phi = 1$ contour, indicating stoichiometric burning which is expected in non-premixed diffusion flames. Also, the peak temperature is 1937 K, approximately 400 K lower than the stoichiometric adiabatic flame temperature. This shows that the reaction is not completely burning the reactants, causing the lower flame temperature, as expected in strained diffusion flames.

The solid black lines in Fig 3.8 show the temperature, x -velocity, and fuel and oxidizer mass fractions along the centerline which is shown as the dashed white line in Fig. 3.7. The dashed-dot red lines show results from 1D counter-flow flame simulations using Cantera [61] with the Wang and Laskin [59] mechanism for ethylene-air. These results show that BIC-FCT with the CDM can compute the structure of a counterflow diffusion flame with some small differences from the 1D solutions using a detailed chemical model.

Figures 3.8a and d show that BIC-FCT predicts a larger thermal layer, the region where temperature is larger than 300 K, in both cases. For the 4 m/s case, the thermal layer from BIC-FCT is 1.44 mm wide whereas Cantera is 1.35 mm. For the 3 m/s case, BIC-FCT is 1.71 mm and Cantera is 1.60 mm. In both cases, BIC-FCT predicts a 7% larger thermal layer. This can be attributed to its larger peak



(a) Temperature along the center line for air and fuel inflow of 4 m/s. (b) Velocity along the center line for air and fuel inflow of 4 m/s. (c) Fuel and oxidizer mass fractions along the centerline for air and fuel inflow of 4 m/s.



(d) Temperature along the center line for air and fuel inflow of 3 m/s. (e) Velocity along the center line for air and fuel inflow of 3 m/s. (f) Fuel and oxidizer mass fractions along the centerline for air and fuel inflow of 3 m/s.

Figure 3.8: A comparison of results from two steady-state counter-flow diffusion flame computations using BIC-FCT and the Cantera [61] chemical equilibrium software. (a) - (c) are results from air and fuel inflow of 4 m/s, whereas (d) - (f) are results for 3 m/s. BIC-FCT uses the CDM as its chemical model for a 2D counter flow flame simulation. Cantera uses a detailed mechanism [59] for a quasi-1D counter flow flame simulation. Cantera results are dashed red lines and BIC-FCT results are solid black lines.

temperature, which, for the 4 m/s case, is 148 K higher and for the 3 m/s case, is 171 K higher than that computed by Cantera. This difference in peak temperature can be attributed to the present CDM calibration procedure. Although both the CDM used by BIC-FCT and multi-step chemical model used by Cantera have the same the laminar flame speed, thickness, and temperature, the CDM calibration procedure does not explicitly consider the rate of temperature rise of the multi-step model. Therefore, the rate of temperature rise is different between the two chemical

models. In a counter flow diffusion flame, there is continuous transport of reactants away from the flame which causes an incomplete conversion of reactant to product. During this incomplete chemical conversion process, the rate of temperature rise dictates the final flame temperature. Because this rate is different between the two models, the flame temperature is different. We expect better agreement with further calibration of the CDM. This is left to future work.

The velocity comparisons in Figs. 3.7b and e show strong agreement within the thermal layer with small differences outside of it. The largest difference is on the fuel-side of the thermal layer, with BIC-FCT predicting a slower velocity. This is because of the difference in molecular weight assumed in the CDM and Cantera. The CDM in this paper assumes a constant molecular weight of 28.5 g/mol whereas the multi-step model uses a molecular weight of 28.05 g/mol for ethylene and 28.96 g/mol for air. The fuel and oxidizer mass fractions of both methods shown in Fig. 3.7b show the reactant concentration decreasing within the thermal layer, with BIC-FCT predicting higher concentration, when compared to the multi-step model in Cantera, for both the oxidizer and fuel within the flame. This is because the CDM in this paper uses a single-step Arrhenius rate which converts the reactants directly to product, whereas the multi-step model converts the O_2 and C_2H_4 to other intermediate species before forming the products.

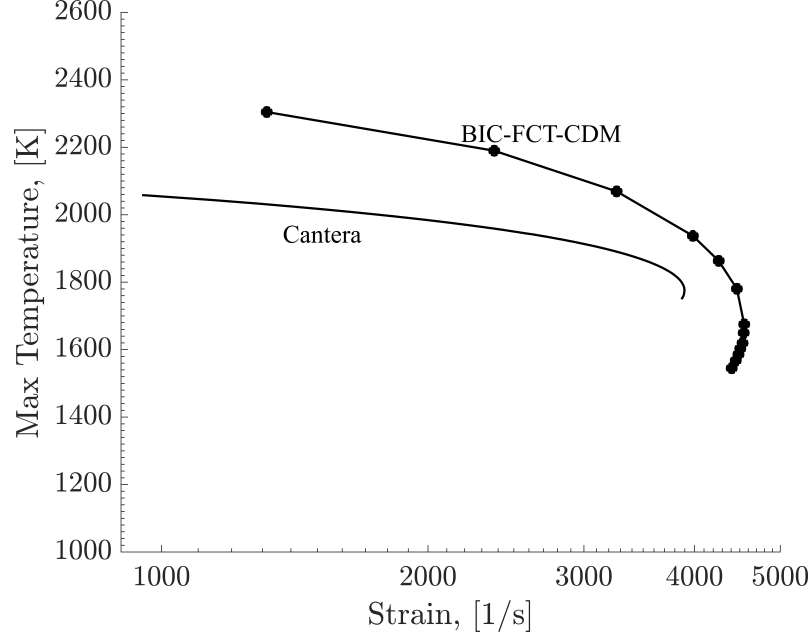


Figure 3.9: A comparison of Cantera and BIC-FCT-CDM in how they predict the temperature versus strain relationship for counter-flow diffusion flames of ethylene-air. The strain is calculated as the maximum velocity gradient on the oxidizer side of the flame.

BIC-FCT shows a 132 K decrease in temperature for the higher strain case, i.e. the case with 4 m/s inflow, showing that BIC-FCT is able to capture the trend of decreasing temperature with increasing strain rate in diffusion flames. The strain versus temperature relationship predicted by the CDM and BIC-FCT is further investigated by carrying out additional simulations which vary the inflow rates of fuel and air. The inflow velocities are varied from 1 m/s to 5.9 m/s. A comparison of these results with Cantera is shown in Fig. 3.9. Similar to the two cases presented earlier, BIC-FCT-CDM over predicts the temperature for all strain rates, but captures the trend of decreasing temperature with increasing strain. With sufficiently

high strain, the flame extinguishes. This result shows that BIC-FCT with the CDM can compute extinction.

Overall, the results show that the combined BIC-FCT and CDM methods can compute the critical features of a counter flow diffusion flame, which include the velocity profile, species concentration, decreasing peak temperature with increasing strain, and extinction. With further calibration of the CDM, we expect the agreement with Cantera and the multi-step model to be stronger. This is left to future work.

3.4 Two-dimensional triple flame

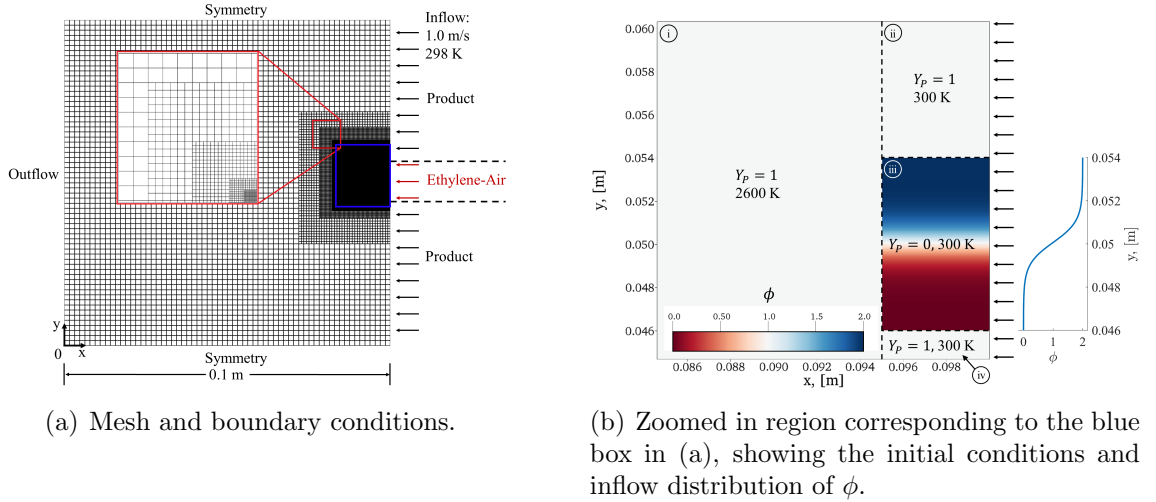


Figure 3.10: Schematic of the mesh and the initial and boundary conditions for a triple flame simulation. The red box in (a) shows a zoomed in region near the mesh refinement.

Triple flames play an important role in the ignition of nonpremixed flames, such as in lifted diffusion flames or in turbulent nonpremixed flows [65]. They form in the regions of flows which are partially premixed with a gradient of stoichiometry

spanning from fuel-rich to fuel-lean. Triple flames propagate through these regions with three distinct burning modes: rich premixed, lean premixed, and non-premixed (diffusion flame). The rich and lean premixed flames generate excess fuel and oxidizer which surround and diffuse towards the stoichiometrically burning diffusion flame. The premixed flames can stabilize the diffusion flame in flows which are faster than the stoichiometric flame speed by causing the flow ahead of the triple flame to diverge, thereby lowering the local flow velocity that the triple flame propagates into. The resulting heat release and flow structure is complex but also important in computing many nonpremixed reactive flows. We therefore simulate a triple flame to assess the ability of BIC-FCT to compute such a complex flame structure.

3.4.1 Boundary and Initial Conditions

To simulate a triple flame, we consider an ethylene-air mixture within a 0.1 m square domain with an inflow-outflow boundary as indicated in Fig. 3.10a. The domain uses a Cartesian mesh with 7 levels of refinement. The coarsest cell size is 0.1 m/64 while the smallest cell size is 0.1 m/4096, approximately 12 cells within the stoichiometric flame thickness for ethylene-air. The mesh is refined in the region outlined by the blue box in Fig. 3.10a. This region is defined by $x > 0.085$ m, $y < 0.06$ m, and $y > 0.045$ m.

The boundary conditions consist of symmetry conditions along the upper and lower boundaries, an outflow on the left, and an inflow on the right. The outflow condition uses the same pressure gradient condition in Eq. 3.4. Here L is 0.1 m and

the y coordinate is swapped with the x coordinate. The inflow condition specifies a uniform velocity of -1 m/s and temperature of 298 K. The inflow species are segregated into three sections, as shown by the horizontal black dashed lines in Fig. 3.10a. The upper and lower sections are an inert coflow of product with no reactants. In the center is a partially premixed ethylene-air mixture with an equivalence ratio that varies from $\phi = 0$ at $y = 0.046$ m to $\phi = 2$ at $y = 0.054$ m. The distribution of ϕ at the inflow is shown on the right of 3.10b. All other primitive variables at the inflow and outflow boundaries are extrapolated using a zero-gradient Neumann condition.

Figure 3.10b shows the initial conditions within the refined region. The initial conditions are separated by the black dashed lines in Fig. 3.10b into four sections, each labeled with a circled Roman numeral. Region i of Fig. 3.10b corresponds to the part of the domain where $x < 0.095$ m. Region ii is $x > 0.095$ m and $y > 0.054$ m. Region iii is 0.046 m $< y < 0.054$ m and $x > 0.095$ m. Region iv is $y < 0.046$ m and $x > 0.095$ m. Regions i, ii, and iv are initialized with all product. Region iii is initialized with ethylene-air which has a gradient in stoichiometry along the y -axis, the same as used in the inflow. Regions ii, iii, and iv, i.e. the domain that is to the right of $x = 0.095$ m, are initialized with a temperature of 300 K while region i is initialized with 2600 K. The entire domain is initialized with a velocity of -1 m/s and a pressure of 1 atm. The hot product gas in region i is the energy source for ignition of the cold reactant gas in region iii. The coflow of inert product gas in regions ii and iv and in the inflow serve to contain the flame within a small part of the domain.

3.4.2 Results

The steady-state results are shown in Fig. 3.11. Figure 3.11a shows the temperature distribution overlaid with contours of heat release rate. Although the inflow velocity is faster than the stoichiometric flame propagation speed, the tip of the flame initially moves upstream into the inflow and eventually stops at an equilibrium position that is 0.5 cm from the inflow boundary. This is because the gas that is upstream of the flame decelerates to a velocity below the flame speed as it approaches the low-density, high-temperature gas generated by the flame. This behavior is qualitatively consistent with many reported results in experiments [65, 66, 67].

The highest heat release occurs in the region near the tip of the flame, consistent with other computations [65, 68]. As seen in Fig. 3.11a, the oblique heat release regions correspond to lower flame temperatures while the center heat release region corresponds to the highest flame temperature, which is near the adiabatic flame temperature for stoichiometric ethylene-air.

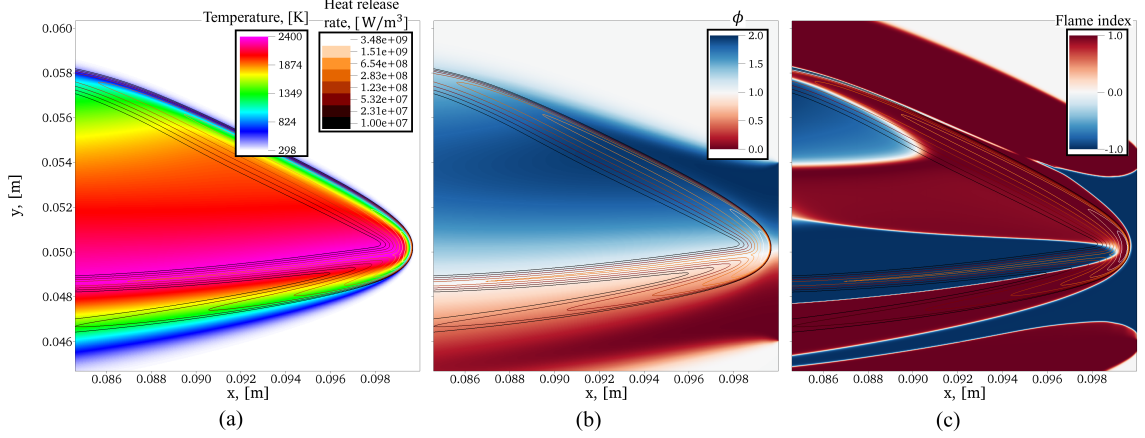


Figure 3.11: Maps of (a) temperature, (b) equivalence ratio, and (c) flame index overlaid with contours of heat release rate of the triple-flame simulation.

Figure 3.11c shows the flame index [69] calculated to visualize the flame structure. The flame index is given by

$$\text{Flame Index} = \frac{\nabla Y_F \cdot \nabla Y_{Ox}}{|\nabla Y_F| |\nabla Y_{Ox}| + \epsilon} \quad (3.5)$$

where ϵ is some small number to prevent division by zero. The flame index ranges from -1 to 1. Positive values indicate regions where the fuel and oxidizer gradients point to the same direction, corresponding to a premixed flame. Negative values indicate regions where the fuel and oxidizer have opposite gradients, corresponding to a diffusion flame. Taken together with the heat release rate contours, the oblique heat release regions overlapping the red regions of Fig. 3.11c are premixed flames and the center heat release region overlapping the blue region is a diffusion flame. From the map of equivalence ratio shown Fig. 3.11b, we can also see that the upper

premixed flame is fuel rich and the lower premixed flame is fuel lean. The center flame is stoichiometric, consistent with Fig. 3.11a which shows that the center flame temperature is near the adiabatic, stoichiometric flame temperature. These results show that BIC-FCT can compute the heat release and flow structure of a triple flame.

3.5 Two-dimensional, unsteady, coflow diffusion flame

In this section, we present a simulation of an unsteady, coflow diffusion flame to answer two key questions: 1. Can BIC-FCT with the CDM compute a lifted diffusion flame? 2. How does the boundary condition presented in 3.4 interact with vortex structures which have gradients in density, temperature, and pressure?

3.5.1 Boundary and Initial Conditions

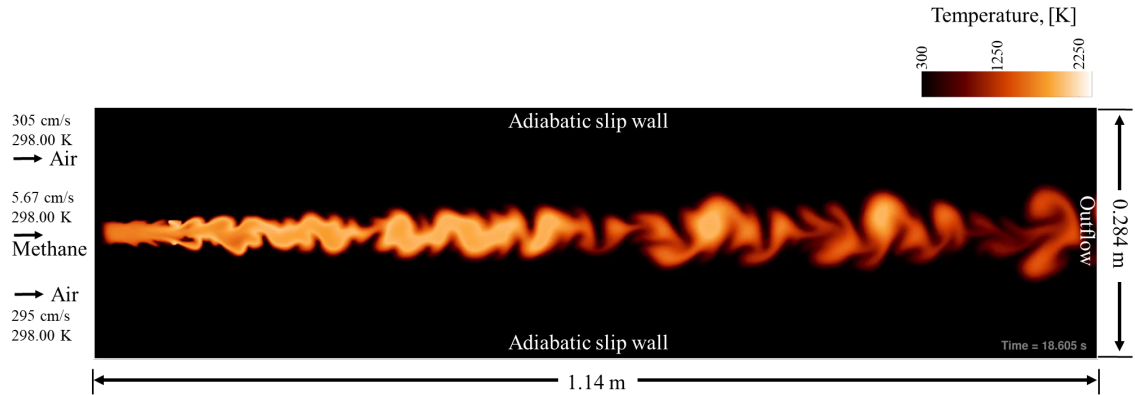


Figure 3.12: Boundary conditions overlaid with the instantaneous temperature map from the simulation result of a the 2D, unsteady, coflow diffusion flame.

The boundary conditions with the resulting temperature map is shown in Fig. 3.12. The inflow boundary on the injects methane in the center with a temperature of 298 K and velocity of 5.67 cm/s. The inflow has a parallel coflow of air with a temperature of 298 K. The upper air inflow has a velocity of 305 cm/s and the lower air inflow has a velocity of 295 cm/s. The air inflows are defined to by asymmetric to promote the growth of shear layer instabilities. The outflow boundary on the right uses the same boundary condition as described in Eq. 3.4. The upper and lower walls are adiabatic symmetry planes. All other primitive variables at the inflow and outflow boundaries are extrapolated using a zero-gradient Neumann condition. The entire domain is discretized using a uniform, Cartesian mesh with $\Delta x = 28.4/2056$ cm.

The simulation begins with a slower coflow of air with a velocity of 10.48 cm/s to establish a laminar diffusion flame. The domain is first initialized with hot product gas with a temperature of 2000 K to provide a heat source for ignition. The initial pressure is 1 atm. After a steady-state, laminar diffusion flame is established, we accelerate the air inflow to its full velocity of 305 cm/s in the upper layer and 295 cm/s in the lower layer over a period of 1 second. This acceleration increase the velocity linearly in time.

3.5.2 Results

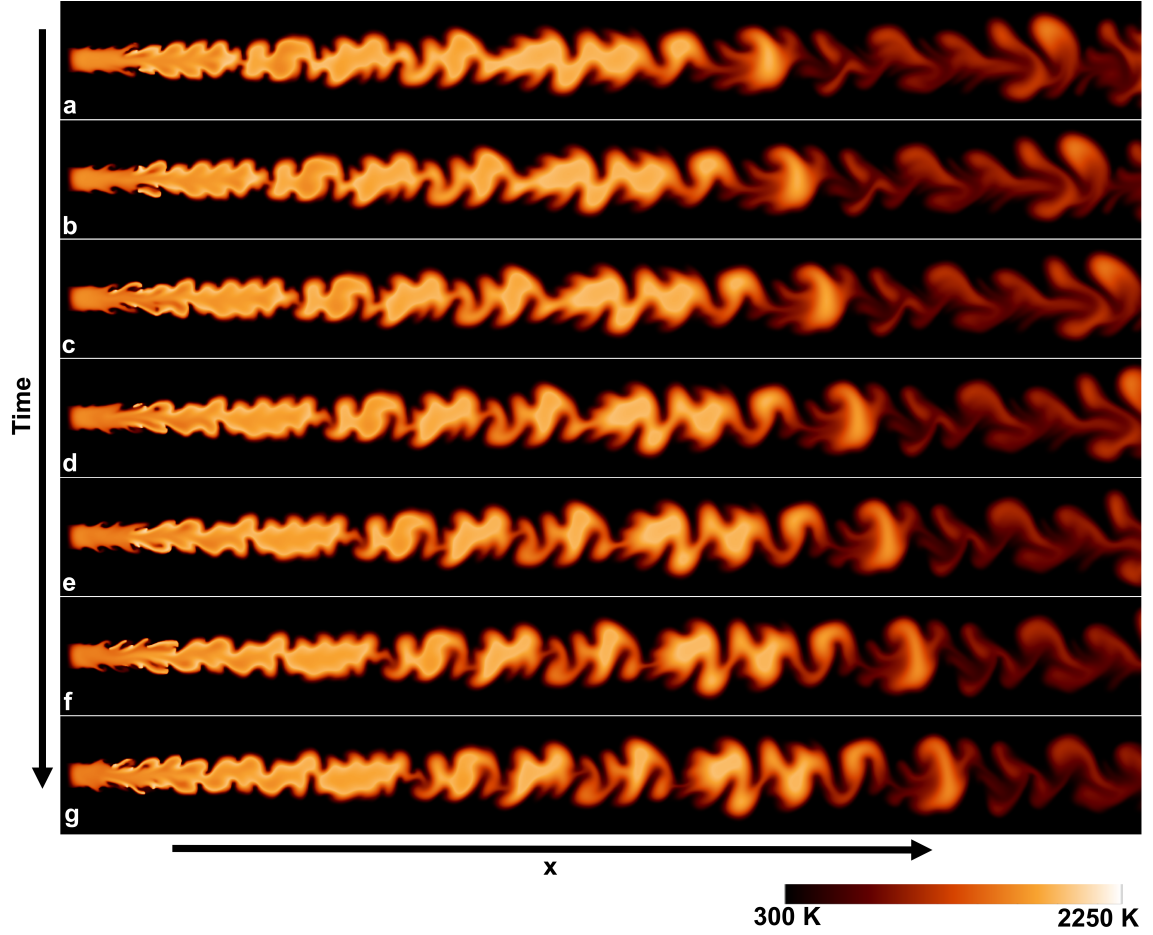


Figure 3.13: Temperature maps at different time instants in the simulation. a) 19.843 s, b) 19.852 s, c) 19.862 s, d) 19.873 s, e) 19.883 s, f) 19.893 s, and g) 19.902 s

Temperature maps at successive time instants after the flow has fully developed are presented in Fig. 3.13. The flame is lifted from the inflow boundary and is stabilized by a region of reverse flow near the inlet. The reverse flow occurs due to the strong wake-like flow created by the slow velocity of the fuel and faster coflow

velocity of the air. We find that increasing the air velocity in this configuration leads to blow-off. In Fig. 3.13, the combustion generates hot product gasses which then mix with the colder coflow of air through the unsteady shear layer. The shear layer develops vortical structures which are convected towards the outflow. These structures do not undergo drastic changes as they approach the outflow, indicating that the outflow pressure boundary condition given by Eq. 3.4 and the zero-gradient Neuman condition are able to convect complex flow structures out of the domain without introducing strong reflections back into the domain. Also, a mean pressure of 1 atm is maintained through the computation, showing that the boundary conditions are able to maintain the desired mean pressure.

These results show that the combined BIC-FCT and CDM methods can compute lifted diffusion flames and reactive and unsteady shear layers. They also demonstrate that the boundary conditions are sufficiently non-reflective.

3.6 Three-dimensional fire whirl

Fire whirls form when circulation couples with the hot, bouyant flow of burning material, generating swirling structures of hot gas. The flow field of a fire whirl is a highly unsteady vortex and its properties are tightly coupled to the diffusion and combustion processes. The vortex core contains unburned fuel which rotates and mixes with the entrained air. The fuel-air mixture burns, generating a column of hot, low-density gas which rises upward forming a jet-like velocity profile. The resulting flow is characterized by the whirling structure of this hot gas with turbulent eddies

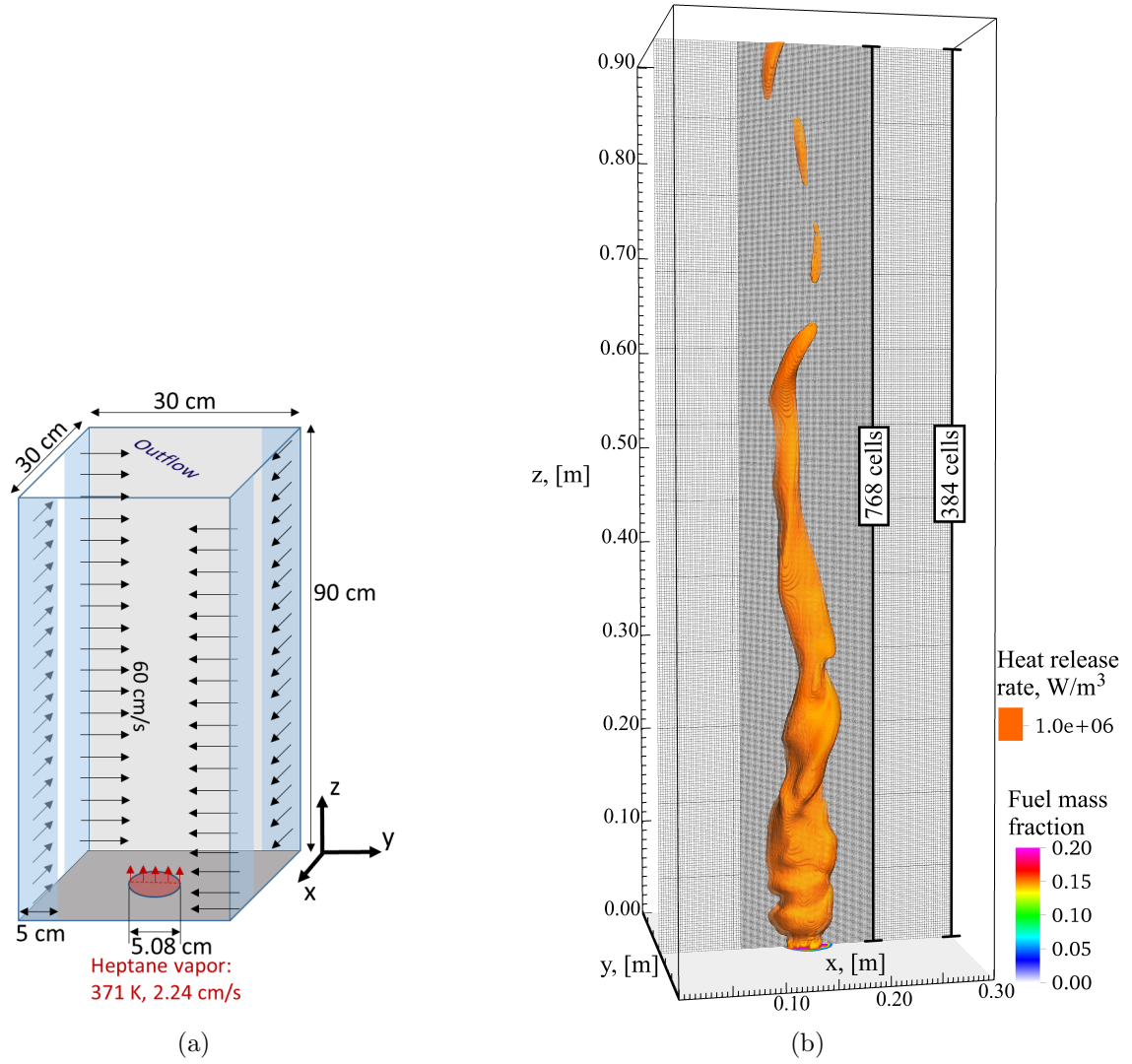


Figure 3.14: Three-dimensional, unsteady fire whirl computation. (a) A schematic of the geometrical setup (not to scale) and boundary conditions for the fire whirl computation. (b) A slice of the computational mesh overlaid with the 3D contour heat release. The mesh is refined in the center.

outside of the vortex. We compute a 3D fire whirl to demonstrate that the BIC-FCT algorithm can be used to compute such an unsteady, turbulent flow field with chemical energy release.

3.6.1 Boundary and Initial Conditions

To study fire whirls, laboratory studies apply circulation to a flame with geometries such as rotating screens [3], offset cylinders [8], and square chambers with corners [5] open to ambient air. Here, we consider a square chamber with four open corners.

A schematic of the geometrical setup and boundary conditions is shown in Fig. 3.14a. The vertical walls are 90 cm tall and 30 cm wide. The bottom floor is 30 cm \times 30 cm. Fuel with the burning properties of heptane vapor is injected at the center of the bottom floor with a constant velocity of 2.24 cm/s and temperature of 372 K within a diameter of 5.08 cm. Circulation is applied by forcing air through the corners with a speed of 60 cm/s along slits which are 5 cm wide. The boundary conditions on all walls are specified to be non-slip. The upper boundary is an outflow condition which specifies a zero-gradient Neumann condition for all primitive variables. The boundary pressure at the outflow is extrapolated using a far-field gradient from Eq. 3.4 with $L = 1$ m, $P_\infty = 101316$ atm, and the y coordinate swapped with the z coordinate. The effects of buoyancy are included with a gravity source term.

The initial conditions consist of quiescent air with a temperature of 298 K and

pressure of 1 atm. A column of hot product gas with a temperature of 2500 K is placed in the center above the fuel inlet to provide a source for ignition.

Figure 3.14b shows a slice of the computational mesh overlaid with a 3D contour of the heat release rate with a value of $1.0 \times 10^6 \text{ W/m}^3$. The mesh uses two levels of refinement. The coarsest cell size is $0.3 \text{ m}/128$ while the finest cell size is $0.3 \text{ m}/256$. The coarse mesh has 6.3 million cells and the refined mesh has 16.6 million cells.

To reduce computational cost, the simulation initially starts with one level of refinement using the coarsest cell size. When the flow reaches a quasi-steady state around $t = 5.4 \text{ s}$, we further refine the mesh around the core with a width of 0.12 m . Afterwards, the computation is carried out for another 3.6 s using the refined mesh. Using $CFL_{fluid} = 0.3$, the average time step for the coarse mesh is $7.1 \times 10^{-5} \text{ s}$ and for the fine mesh is $3.5 \times 10^{-5} \text{ s}$.

3.6.2 Results

Volume renderings of the temperature are shown in Figs. 3.15a to f for selected time instances in sequential order from 7.906 s to 8.007 s . At this point in time, the mean flow field has established a whirling, columnar flame in the center of the domain. The flame is anchored to the bottom floor around the fuel inlet. Near the bottom, the flame temperature is the hottest and the width of the flame is the widest. In the upper region near the outflow, the temperature is colder and the flame column is narrower.

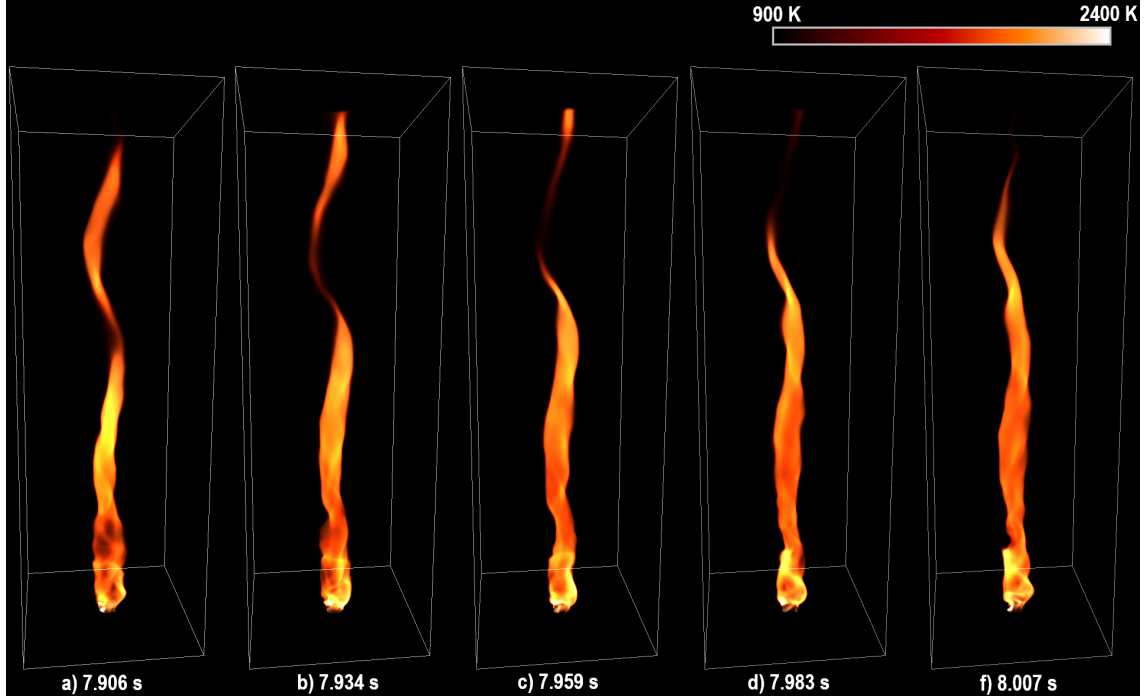


Figure 3.15: Volume renderings of the temperature for selected time instances. Visualisation was performed using the yt-project python library [70].

A spiraling structure, visible in Fig. 3.15a, forms in the upper part of the flame. In Fig. 3.15b, the upper portion of the spiral begins to detach from the lower part of the flame. In Fig. 3.15d, the detached flame is convected out of the domain and in Fig. 3.15f, the flame becomes a single column with the formation of another spiraling structure.

Figure. 3.16 shows volume renderings of the stoichiometric equivalence ratio, i.e. the flame sheet, for the same time instances shown in Fig. 3.15. Here, the whirling, helical structures are more evident than in Fig. 3.15. The columnar structure of hot gas shown in Fig. 3.15 is closely aligned with the flame sheet shown in Fig. 3.16. The flame sheet, however, shows an earlier detachment of the spiraling structure in Fig. 3.16a which was not visible in the thermal structure shown in Fig.

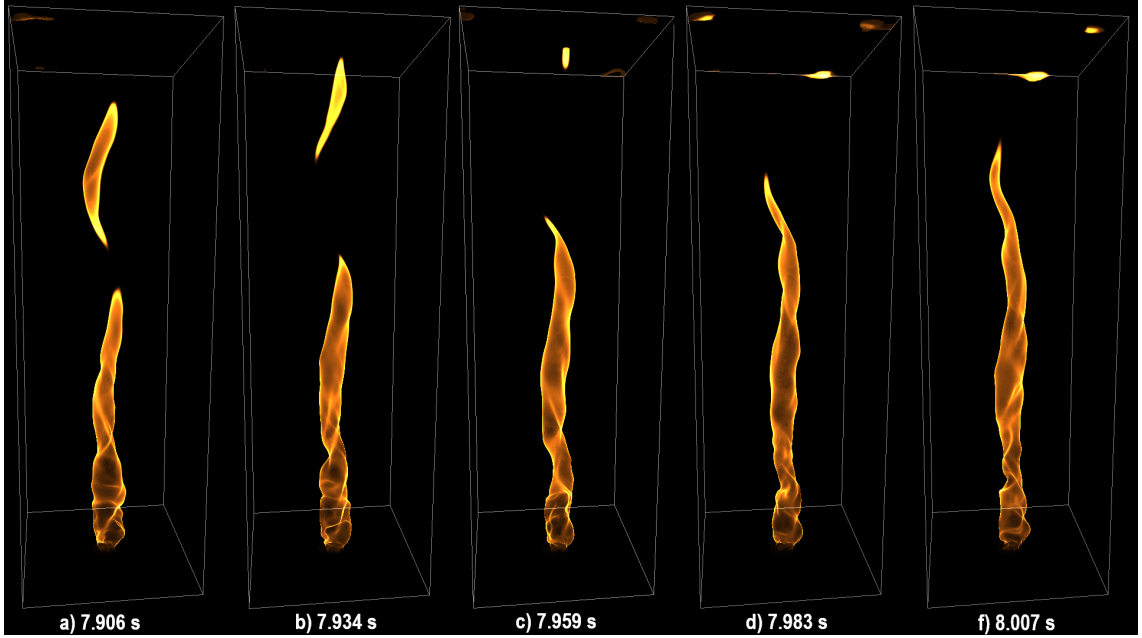


Figure 3.16: Volume renderings of the stoichiometric equivalence ratio. Visualisation was performed using the yt-project python library [70].

3.15a.

The temperature and flame sheet shown in Figs. 3.15 and 3.16 show that the BIC and CDM algorithms can compute the qualitative, three-dimensional features of a fire whirl. The close alignment of the hot gasses with the flame sheet demonstrates that the CDM is computing heat release correctly and that the implicit correction in the BIC algorithm can compute the pressure for whirling, three-dimensional flows with heat release.

Figure 3.17 shows the turbulent structure of the computed fire whirl through instantaneous, center-slice maps of temperature, tangential velocity, axial velocity, and gauge pressure at $t = 8.95$ s. Here, we define gauge pressure as $P' = P - P_\infty$. Contours of heat release rate are overlaid on all four of the figures to denote the flame position. In the temperature, small eddies are seen just outside of the flame

region, but is more laminar within the flame region. This is also the case in the tangential and axial velocities. The eddies can also be seen in the pressure by small regions of low pressure outside of the flame region, corresponding to the centers of the eddies.

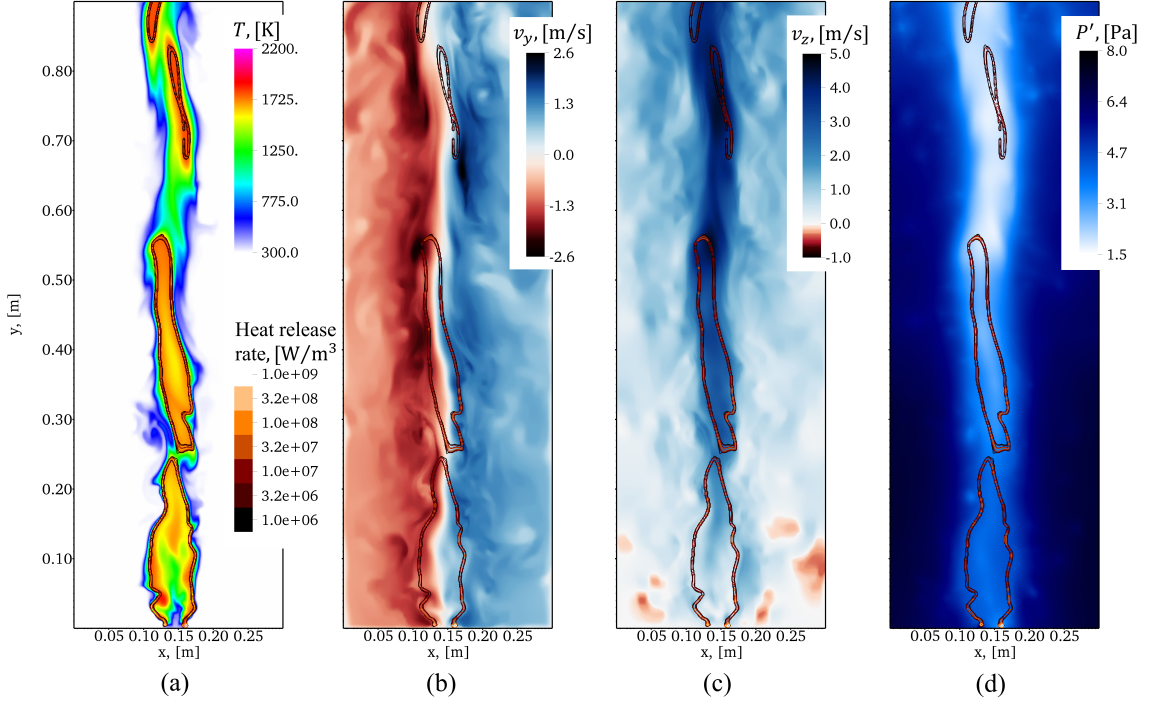


Figure 3.17: Instantaneous maps of (a) temperature, (b) tangential velocity, (c) axial velocity, and (d) gauge pressure at $t = 8.95$ s. The gauge pressure is defined as $P - 101316$ Pa where P is the absolute pressure and 101316 Pa is the minimum measured pressure within the domain.

The high temperature region is concentrated in the center of the domain with the peak temperature not exceeding the adiabatic flame temperature, shown by Fig. 3.17a. Furthermore, the regions of peak temperature overlap with the regions of heat release. These results demonstrate that the energy “storage” variable S and

the pressure correction in Eq. 2.19 are able to distribute the chemical energy release in unsteady, turbulent conditions and not just for steady, laminar flows.

The tangential velocity is shown in Fig. 3.17b. The peak tangential velocity occurs just outside the active reactive regions, consistent with experimental measurements in [4, 18] and shows the formation of a columnar vortex. Figure 3.17c shows the axial velocity, which increases as the height increases and has a jet-like profile near the center of the domain. Figure 3.17d shows a map of the gauge pressure which shows lower pressure near the center, corresponding to the vortex core. The pressure becomes lower near the upper part of the domain as the flow accelerates due to buoyancy and bulk flow effects. In previous work, we have shown that Eq. 2.19 is able to correct the pressure for vortex flows, and this result demonstrates that Eq. 2.19 is also able to correct the pressure for vortex flows with chemical energy release.

We show the time-averaged temperature, axial velocity, and tangential velocity, and gauge pressure along the radial direction at different heights in the domain in Fig. 3.18. The averaging was performed over the last 2 s of the simulation. The black line corresponds to 5 cm, the purple line corresponds to 25 cm, and the blue line corresponds to 85 cm. The filled circles correspond to the computational cell locations.

Figure 3.18a shows the averaged temperature profile at different heights. The temperature at the lower height of $z = 5$ cm shows two peaks near the edge of the vortex core. This height is in the reaction region and the two peaks correspond to the flame sheet. The region between the two peaks contains unburned fuel which is

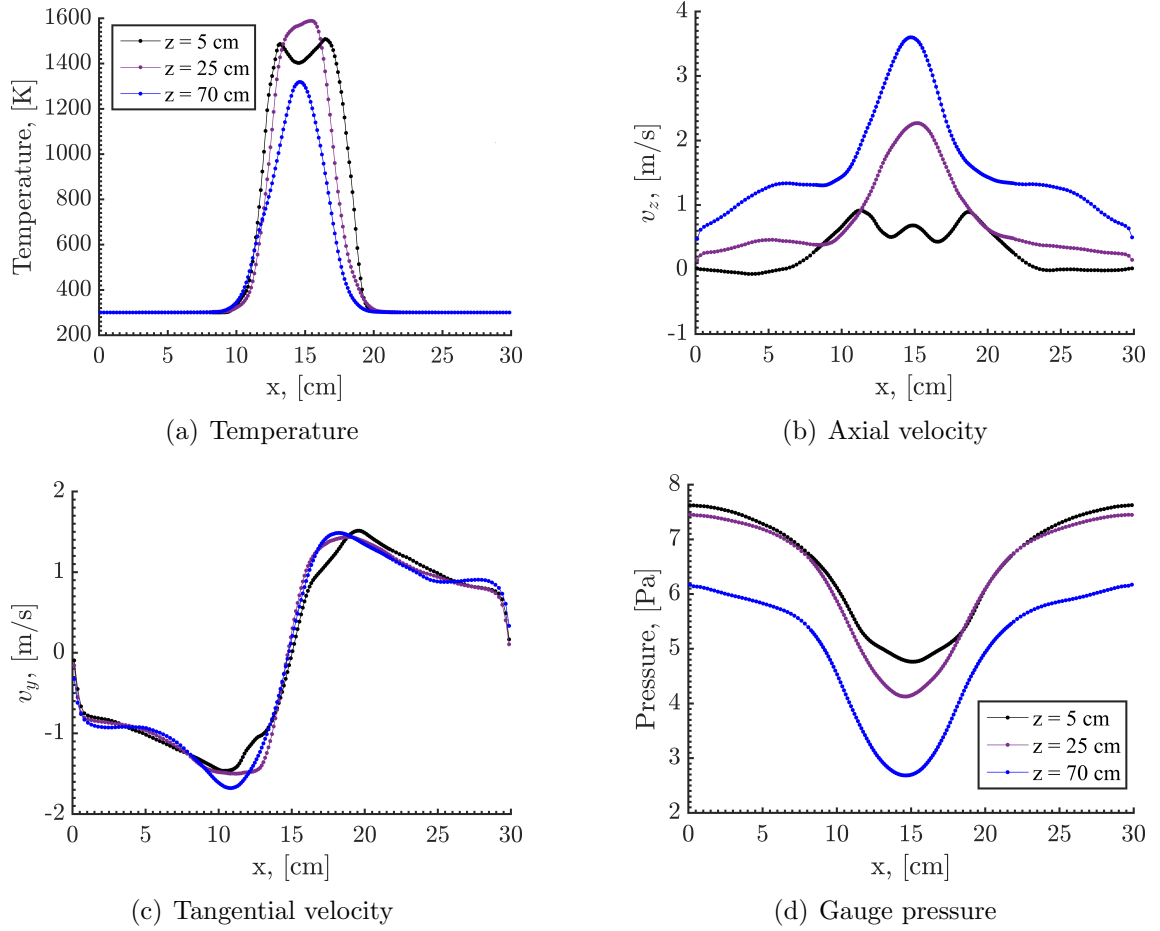


Figure 3.18: Averaged (a) temperature, (b) axial velocity, (c) tangential velocity, and (d) gauge pressure of the fire whirl simulation. The averaging was performed over the last 2 s of the computation.

colder than the flame sheet, but hotter than the ambient temperature since the heat from the flame diffuses inward raising the temperature of the unburned fuel within the core. This result is consistent with experimental temperature measurements of fire whirls [3, 5, 17, 18, 71]. At $z = 70$ cm, the flow is within the plume region where there is little to no reaction, and so the peak temperature decreases and the profile attains a parabolic shape with the peak near the center of the domain. This is consistent with what is observed in experiments [5, 17, 18, 71] and in prior simulations [23, 24].

Figure 3.18b shows the averaged axial velocity. The axial velocity near the bottom boundary shows peaks near the location of the high temperature gradient, similar to what is reported in experiments [5, 18] and simulations [23]. Further from the bottom boundary, the peak of the axial velocity is in the center of the domain, with increasing peak velocity as the height increases due to the bouyancy effect. The parabolic profile and the trend in the velocity are also qualitatively consistent with experiments [7, 18] and other simulations [23, 24].

The averaged tangential velocity shown in Fig. 3.18c shows that the average peak tangential velocity is approximately 1 m/s lower than the peak tangential velocity seen in the instantaneous results. The tangential velocity profile attains two peaks just outside of the high temperature core with rotational flow inside of the core and irrotational flow outside of it. This structure is seen in experimental measurements of fire whirls [4, 7, 18] and also in other simulations [22, 24]. The averaged pressure in Fig. 3.18d shows a minimum pressure near the center, corresponding to the center of the vortex core. The pressure decreases as the height increases due to

increasing axial velocity.

We now compare the velocity with an analytical vortex model. Prior studies have used different vortex models (Rankine, Burgers, and Sullivan) to describe the velocity field of a fire whirl [17]. The most recent experimental work [7, 18, 72] show that the Burgers vortex provides the best fit. We therefore compare our results against the Burgers vortex model. Here, we focus on the tangential (azimuthal) component of velocity. The radial profile of the tangential velocity U_θ for a Burgers vortex is given by

$$U_\theta = \frac{\Gamma_0}{2\pi r} \left(1 - e^{-kr^2}\right) \quad (3.6)$$

where Γ_0 is a far-field circulation and r is the radius which starts at 0 within the center of the vortex. The parameter k is a constant that is determined according to

$$r_c = \alpha k^{-0.5} \quad (3.7)$$

where r_c is the radial location of the peak tangential velocity and α is approximated to be 1.12091 [7, 17, 18, 72].

The time-averaged, radial profile of the tangential velocity at a height of 70 cm from the numerical simulation is shown in Fig. 3.19a by the black line with filled circles. The tangential velocity profile can be fit to Eq. 3.6 by considering two parameters: r_c and Γ_0 . The peak tangential velocity along the profile shown in Fig. 3.19a is 1.562 m/s at a radial location of $r_c = 3.8086$ cm. With r_c known, we can solve for k using equation 3.7 which yields $k = 866.19$. Then, we fit the value of

Γ_0 until the tangential velocity profile from Burgers vortex model in Eq. 3.6 yields the same peak velocity and at the same location as the profile from the numerical simulation. The resulting value of Γ_0 is then $0.5225 \text{ m}^2/\text{s}$. The Burgers vortex profile that is fit to the simulation data is

$$U_\theta = \frac{0.5225}{2\pi r} \left(1 - e^{-866.19r^2}\right). \quad (3.8)$$

This is shown in Fig. 3.19a as the solid blue line. The comparison in Fig. 3.19a shows that the inner core of the vortex along with a small region outside of it is well represented by a Burgers vortex profile, which agrees with prior experimental results [7, 18, 72]. The comparison deviates at the larger radial distance because the numerical simulation forms a boundary layer along the vertical wall.

The circulation is also compared between the numerical and Burgers profile. The circulation is computed as

$$\Gamma = 2\pi r U_\theta \quad (3.9)$$

where U_θ is either from Eq. (3.8) or the simulation data. The results are shown in Fig. 3.19b. Similar to the tangential velocity, the circulation decays within the inner vortex core. The circulation for the Burgers model approaches $\Gamma_0 = 0.5225 \text{ m}^2/\text{s}$ as the radius becomes larger, whereas the simulation profile continues to increase due to wall effects. Overall, the agreement within the vicinity of the vortex core between the numerical and analytical profiles shows that the BIC algorithm can compute the vortex structure of a fire whirl.

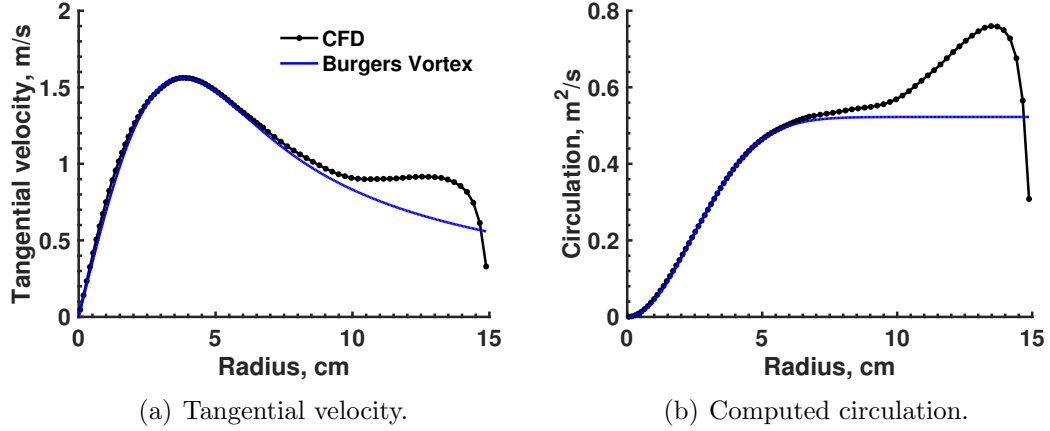


Figure 3.19: A comparison of averaged results from the CFD simulation and a curve fit using a Burgers vortex model for tangential velocity. The filled circles correspond to the locations of computational cells in the simulation.

The results shown here demonstrate that BIC-FCT can compute many of the important features of fire whirls which are reported in prior experimental and numerical work.

3.7 Summary and Conclusions

This chapter has described the extension and application of the BIC algorithm to low-Mach-number flows with chemical reactions and energy release. The original BIC algorithm [44] applied a pressure correction to the inviscid euler equations by solving a single elliptic equation, removing the acoustic limit on the time step constraint. In a prior paper [29], we developed, stabilized, and extended the BIC algorithm for multi-dimensional viscous flows. A scalar variable S was introduced to couple the changes in internal energy from viscous processes to the BIC integration procedure. Here, we described how to include combustion processes into S and the integration procedure. The BIC algorithm was combined with FCT, which

solved the convection process, and a calibrated chemical model, the CDM, which modeled the combustion processes. We then applied the combined BIC-FCT and CDM algorithm to four different test problems, each with increasing difficulty and testing a different aspect of low-Mach-number flows with combustion.

First, we computed a series of 1D, premixed, laminar flames and showed that BIC-FCT can accurately reproduce flame properties that the chemical model used in this paper was calibrated to match. BIC-FCT predicts the correct flame temperature, regardless of the grid resolution. The flame speed, however, requires approximately 4 cells per flame thickness to maintain a 5% error. The results also showed good agreement with the ideal flame properties across a wide range of equivalence ratios.

Second, we computed 2D counter-flow diffusion flames and showed that BIC-FCT with the CDM can compute the temperature, velocity, and species profiles of a strained diffusion flame. BIC-FCT predicts a lower peak temperature when increasing the velocity of the opposing jets, which is an expected result of counter-flow diffusion flames. We compared the results against quasi-1D simulations from chemical equilibrium software [61] using a detailed chemical-transport model [58]. The comparison showed that the temperature, velocity, and species profiles show good agreement. We find, however, that BIC-FCT with the CDM tends to overpredict the peak temperature and size of the thermal layer. We suppose that better agreement can be obtained with further calibration of the CDM or the use of the same chemical-transport model as used in the quasi-1D simulation. This is left to future work.

Third, we computed a 2D triple flame and showed that BIC-FCT is able to compute flows with complex heat release regions. Many features of a triple flame, such as the flame structure, propagation speed, and temperature, qualitatively agree with observations reported in prior experiments and simulations. The results show that the pressure correction in the BIC algorithm is able to correctly compute the pressure in a multi-dimensional flow with gradients in stoichiometry.

Finally, we computed a 3D fire whirl to test the ability of BIC-FCT to compute unsteady, multi-dimensional, turbulent, reactive flows. The results show that BIC-FCT is able to reproduce the observed features of fire whirls, such as the vortex structure, the jet-like axial velocity, the axial velocity increasing as the height increases, and the peak temperature decreasing within the plume region, the hot gas in the vortex core, and the peak tangential velocities just outside of the hot gas column. The major features computed in this simulation are in qualitative agreement with prior work. The results also demonstrate that the BIC-FCT algorithm is stable using a convective CFL condition of 0.3 for unsteady, multidimensional, turbulent, reactive flows and within these flows, the pressure correction is capable of handling chemical energy release.

Chapter 4: Reactive Vortex Breakdown

4.1 Introduction

Swirling jet flows appear in many forms in nature, such as tornadoes, hurricanes, dust devils, and fire whirls. They are used in combustion devices to mix fuel and air or to stabilize a flame. With the “right” conditions of swirl (ratio of azimuthal to axial velocity), adverse pressure gradient (aligned with the jet axis), and Reynolds number, swirling flows transition to a new state with a stagnation point and finite recirculation zone along the jet axis. This transition is referred to as vortex breakdown [26, 73, 74] and the resulting states have significant effects on the ensuing fluid and combustion dynamics.

The result of vortex breakdown has been described by three distinct states [26, 73]: the bubble mode, spiral mode, and double-helix mode. Due to computational constraints, early nonreactive, numerical simulations of vortex breakdown assumed incompressible, laminar, axisymmetric, and steady flows. These assumptions, however, do not allow the computation of the spiral and double-helix modes because of their inherent three-dimensional and unsteady structures [74, 75]. Later approaches solved the unsteady, three-dimensional, incompressible Navier-Stokes equations and were able to compute nonsymmetric modes of breakdown [76, 77].

For example, Spall et al. [76] studied the bubble mode of breakdown and its asymmetry. Ruith et al. [77] computed all three major modes by varying the Reynolds number, swirl, and jet profile.

Vortex breakdown has also been studied in reactive systems, primarily in swirl-stabilized premixed combustors. Huang and Yang [78] computed the flow within such a combustor by using three-dimensional, compressible large eddy simulations (LES) with a flamelet model (FM) and showed that increasing the swirl beyond a critical value can cause an upstream propagation of vortex breakdown. This was also shown by the LES-FM computations of Duwig and Fuchs [79], who also showed the formation of a helical mode.

Recent experiments by Xiao et al. [1] and Hariharan et al. [13] have shown the transition of a fire whirl into a flame which exhibits the characteristics of vortex breakdown. It begins as a swirling, sooty flame which burns a liquid hydrocarbon and then reaches a steady state with only blue luminescence, indicating soot-free burning. The luminescence of the transitional state suggests that helical breakdown modes are present and the steady-state suggests the bubble mode. The flow structure and mode of combustion of this blue flame, the blue whirl, are, however, still unknown.

This chapter presents the first steps in understanding the flow and combustion states of the blue whirl. Here, we present a series of computations which demonstrate that reactive vortex breakdown can be computed using boundary conditions close to those measured in the blue whirl experiments [80]. This is done by solving the three-dimensional (3D), unsteady, compressible, reactive Navier-Stokes (NS)

equations coupled to a calibrated chemical-diffusive model for flames and energy release. The resulting flow and flame structures are presented and discussed.

4.2 Numerical Model

The numerical model solves the unsteady, compressible, reactive Navier-Stokes equations. The hyperbolic fluxes are computed using unsplit, fourth-order, flux-corrected transport. All parabolic fluxes are spatially discretized using a second-order, three-point central scheme. The diffusive fluxes include Fickian species diffusion, Fourier heat conduction, and Newtonian viscosity. The barely implicit correction (BIC) algorithm [29, 44] is used to remove the acoustic limit on the CFL time-step constraint, thereby removing the numerical expense of explicitly integrating the NS equations in a low-Mach-number flow. Further details on the integration procedure are discussed in [29].

We use a calibrated chemical-diffusive model (CDM) [30] to regulate the conversion of reactant to product and control the rate of heat release. The chemical parameters of the Arrhenius rate and heat of combustion are calibrated to reproduce the flame and thermal properties of heptane-air mixtures within a NS computation for varying stoichiometry. This calibration procedure is described in [30]. This work assumes a constant molecular weight of 30.6 g/mol for all species and a constant specific heat ratio of 1.19 for all species and temperatures.

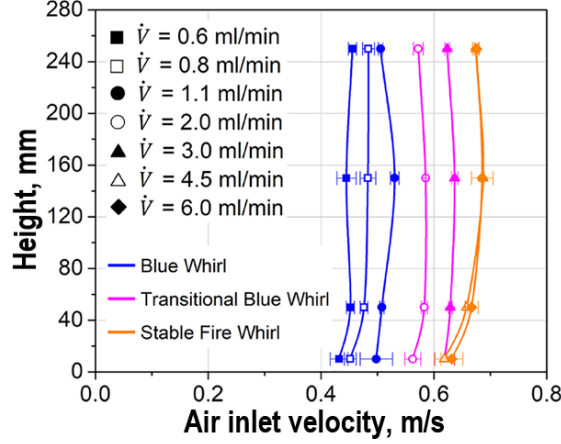


Figure 4.1: (Reprinted from [15]) Measured velocities at the slit inlets at different heights above the bottom surface. The fuel evaporation rates given in terms of volumetric flow rates, \dot{V} , are presented for each of the corresponding velocity measurements. Note that the blue whirl is observed for lower fuel flow rates, from $\dot{V} = 0.6$ to 1.1 ml/min.

4.3 Parameter Study

We perform a series of simulations where the fuel inflow conditions are varied to understand how the fuel evaporation affects the fire whirl. As a starting point on how to set the boundary conditions, we look to recent experimental measurements by Hu et al. [15] who have measured the fuel evaporation rates and the inflow velocities of air at the slits in the half-cylinder configuration [1]. The experimental measurements are presented in Fig. 4.1. The relevant findings here are that the blue whirl burns liquid heptane at a rate of 0.6 ml/min to 1.1 ml/min with corresponding slit velocities in the half-cylinder setup ranging from 45 cm/s to 50 cm/s.

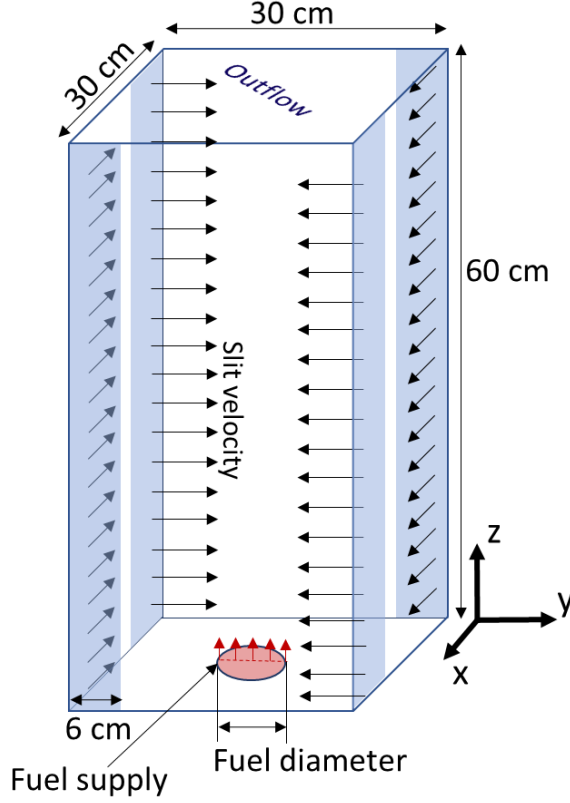


Figure 4.2: Schematic of the domain and boundary conditions used in the parametric study. The slit velocity is 40 cm/s and pushes in air. The fuel is heptane. In the parameter study, the fuel diameter and fuel mass flow rates are varied.

4.3.1 Geometrical Setup and Boundary Conditions

A schematic of the boundary conditions used in the simulations are presented in Fig. 4.2. Using the experiments as a guide, the simulation specifies the slit velocity at the corner gaps to push in air at 40 cm/s. The fuel diameter and fuel supply rates are independently varied. The gaseous fuel supply rate, given in terms of equivalent liquid volumetric flow rate, is varied from 0.25 ml/min to 1.1 ml/min in the simulation. The diameter for the fuel inflow is varied from 1.27 cm to 7.62 cm. A table presenting the simulation cases with values of fuel diameter and flow rates are presented in Table 4.3.1. The resulting fuel inflow velocities are shown in the

Case	Fuel supply rate ml/min	Fuel diameter cm	Fuel velocity cm/s
1	0.25	1.27	2.2416
2	1.1	2.54	2.4657
3	1.1	5.08	0.61643
4	0.7	7.62	0.17434
5	1.1	7.62	0.27397
6	0.25	7.62	0.062265
7	0.4	7.62	0.099624

Table 4.1: Fuel inflow conditions for the 7 cases in the parametric study. The fuel supply rate is the equivalent volumetric flow rate for liquid heptane whereas the fuel velocity is for the gaseous flow rate.

third column.

The initial condition is quiescent air at 298 K with a column of hot product gas at 2500 K placed above the fuel inlet to provide a heat source for ignition. The initial column of product gas has a diameter equal to 110% of the fuel inlet diameter. We find that the steady flow field is insensitive to the size of the column.

The mesh is refined around the center of the domain within a 11 cm square, along the entire height. We use two levels of refinement. The coarse level has a cell size of $\Delta x = 30/128$ cm and the fine level is $\Delta x = 30/256$ cm. The resulting mesh has 8,892,416 cells and a convective CFL of 0.3 is used for all computations.

4.3.2 Results

Here, we focus on cases 1 and 6 of the seven cases. We present the steady-state flow fields of the other five cases in the Appendix. For cases 1 and 6, in Figs. 4.3 and 4.4, we show the temperature, axial velocity, and tangential velocity of the resulting flow fields at a steady state. Cases 1 and 6 have the same fuel supply rate

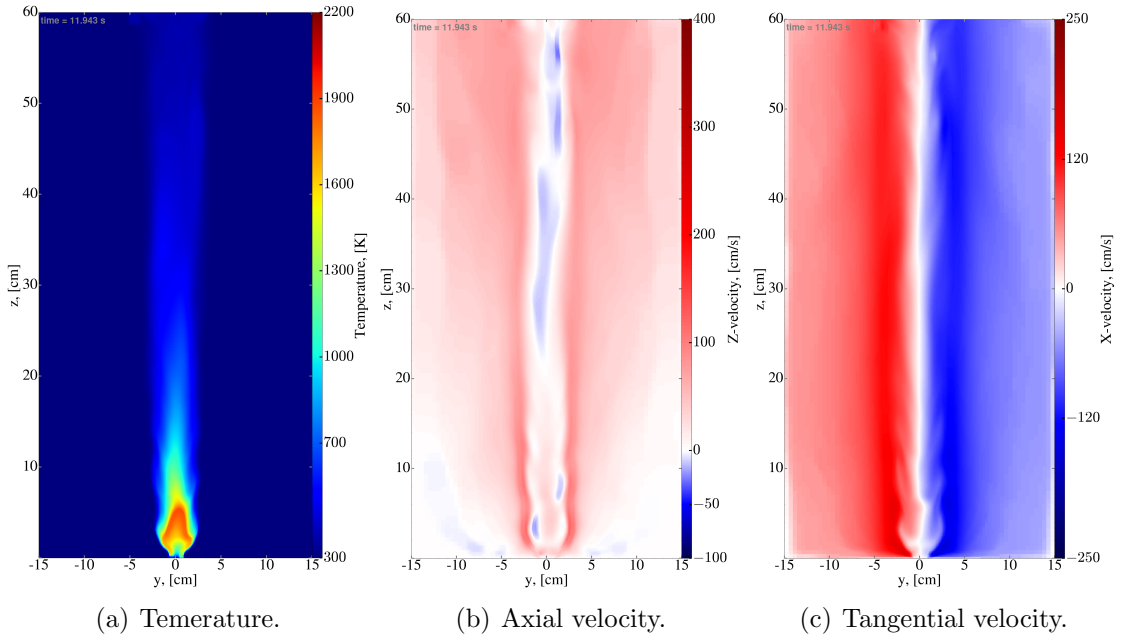


Figure 4.3: Case 1

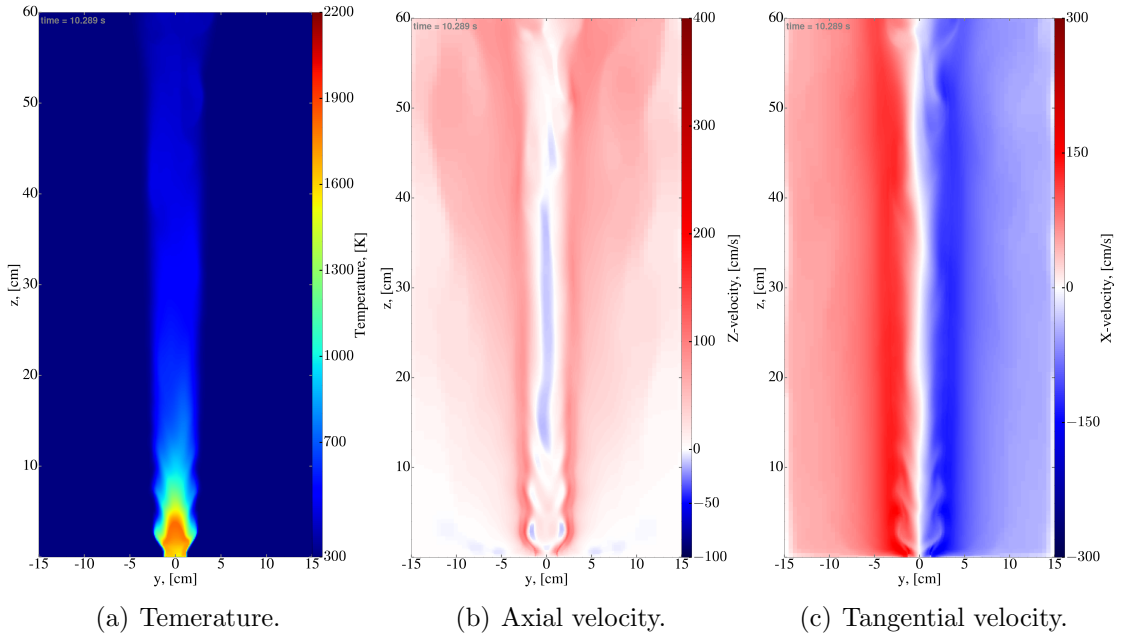


Figure 4.4: Case 6

of 0.25 ml/min with different fuel diameters. Case 1 has a smaller fuel diameter of 1.27 cm and case 6 is larger with 7.62 cm.

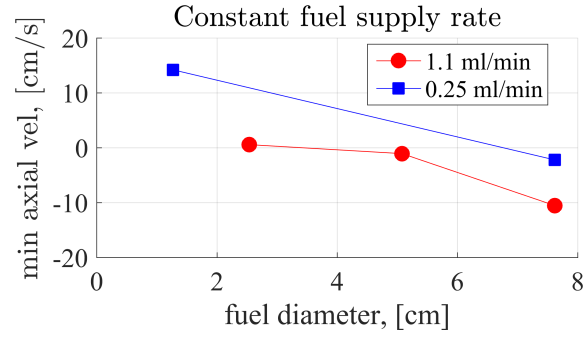
For case 1, Fig. 4.3a shows the flame anchored at the edge of the fuel inlet.

Figure 4.4a shows that for case 6, the flame diameter at the bottom surface is smaller than the fuel inlet diameter of 7.62 cm, showing that the flame has receded away from the edges of the fuel inlet. This is similar to experimental results reported in [16]. In case 6, because the flame is narrower than the fuel inlet, the fuel that enters around of the flame is not burned and is convected away. The flame height for the flame in case 1 is approximately 5 cm and the flame height for case 6 is approximately 4.5 cm, both much shorter than the fire whirl presented in Chapter 4.

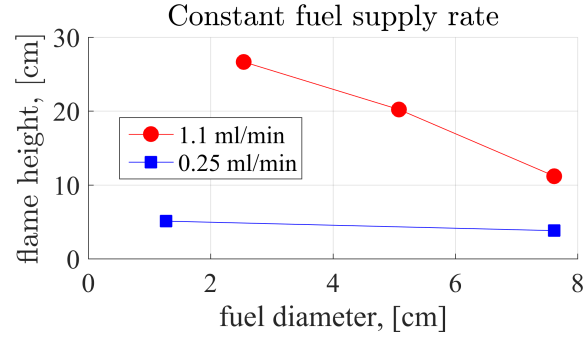
Figure 4.3b shows the axial velocity for case 1. Near the bottom of the domain, there is a toroidal vortex ring surrounding the flame with another toroidal vortex immediately above it. The flow above the flame exhibits a wake-like axial velocity profile, with lower velocity in the center and higher velocity away from the center. The axial velocity develops a reverse flow region at a height of 25 cm and is sustained up to the outflow boundary. The results are similar in case 6, as shown in the axial velocity map in Fig. 4.4b. There are two main differences between case 6 and case 1 in the axial velocity. The first is that in case 6, a small region of reverse flow occurs on the axial center line within the flame region, whereas in case 1, there is no reverse flow region on the centerline within the flame. This suggests there is vortex breakdown occurring within the flame of case 6 but none occurring in case 1. The second difference is that the reverse flow within the wake region occurs at a lower height for case 6 than for case 1.

Figures 4.3c and 4.4c show the tangential velocity map for cases 1 and 6, respectively. In both cases, the tangential velocity develops a maximum and a

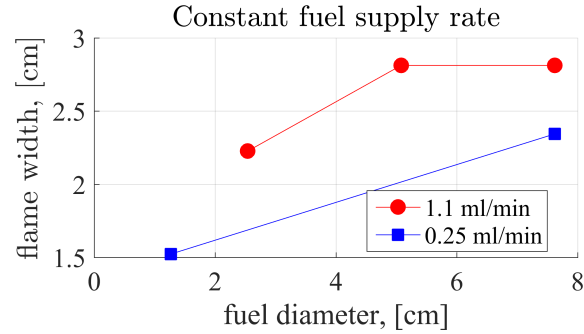
minimum around the flame and plume regions, showing the development of a vortex core.



(a) Minimum axial velocity along the axial center line within the flame region.



(b) Flame height.

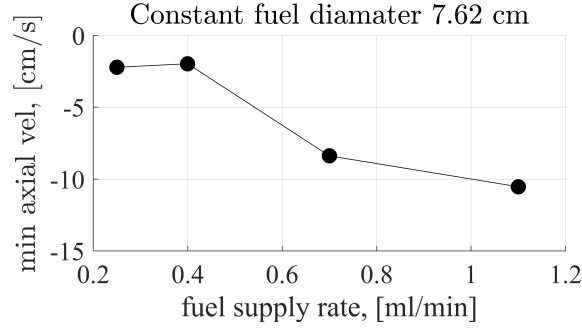


(c) Maximum flame width.

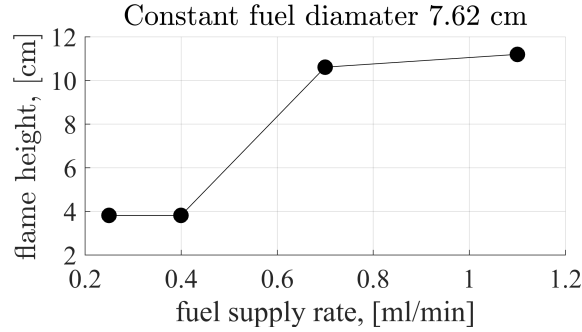
Figure 4.5: Constant fuel flow rate.

In Fig. 4.5, we show the measured minimum axial velocity along the vertical center line within the flame, the flame height, and the maximum flame width as functions of the fuel diameter. The two curves correspond to two different fuel flow rates. Figure 4.5a shows that for increasing fuel diameter, there is a decrease in

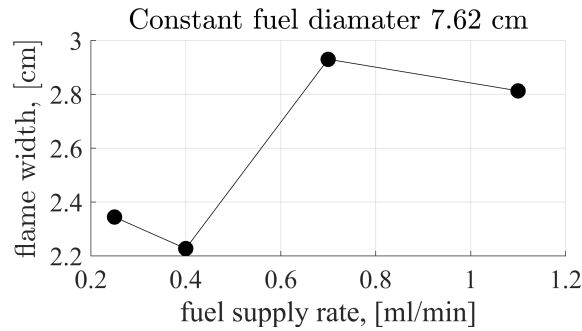
the minimum axial velocity along the centerline in the flame. This suggests that increasing the fuel diameter increases the strength of vortex breakdown. In Fig. 4.5a, we see that increasing the fuel diameter decreases the flame height.



(a) Minimum axial velocity along the axial center line within the flame region.



(b) Flame height.



(c) Maximum flame width.

Figure 4.6: Constant fuel diameter.

Figure 4.6 shows the flow properties from four cases as a function of increasing fuel supply rate for a constant fuel injection diameter of 7.62 cm. Figure 4.6a shows the minimum axial velocity along the vertical center line decreasing as the fuel

supply rate is increased. Figure 4.6b shows that the flame becomes longer as more fuel is supplied. The flame width in Fig. 4.6c is non-monotonic as fuel supply rate is increased, showing that the fuel supply rate of 0.7 ml/min is longer than 1.1 ml/min, and that 0.25 ml/min is longer than 0.4 ml/min. The higher flow rates of 0.7 and 1.1 ml/min are longer than the lower flow rates of 0.25 and 0.4 ml/min.

4.3.3 Discussion

The results suggest that increasing the fuel flow rates or increasing the fuel diameter lead to stronger vortex breakdown, suggesting that doing either may be favorable to the blue whirl formation. Increasing the fuel flow rate, however, leads to longer flame lengths, which is opposite to the decreasing flame length and decreasing fuel evaporation observed during the transition to the blue whirl. Increasing the fuel diameter leads to shorter flame lengths, which is in agreement the decreasing flame length during the observed blue whirl formation, but leaves unburned fuel within the domain, which is in contrast to unreported experimental measurements that suggest all the evaporated fuel is burned. These results, when considered together, are inconclusive on which fuel inflow conditions are needed to compute the blue whirl.

The velocity profiles and temperature maps show that the flow properties above 30 cm in height does not vary much. This suggests that the computational domain could be shortened, allowing for a reduction in numerical cost. Also, the computations may require increased resolution to better resolve the flame and fluid

length scales.

4.4 Lifted Flame Computations

Based off the findings in the parameter study, we performed additional computations with a shortened domain, higher resolution, and fuel injection diameters which are narrower than 1.27 cm. The air inflow was varied from 30 cm/s to 40 cm/s and the fuel supply rate was varied from 0.2 ml/min to 0.6 ml/min. We found that below 0.25 ml/min, the flame would eventually blow out in the computation, never lasting further than 6 physical seconds. The results from the other cases exhibited similar flow and flame characteristics and so we only show one case here.

4.4.1 Geometrical Setup and Boundary Conditions

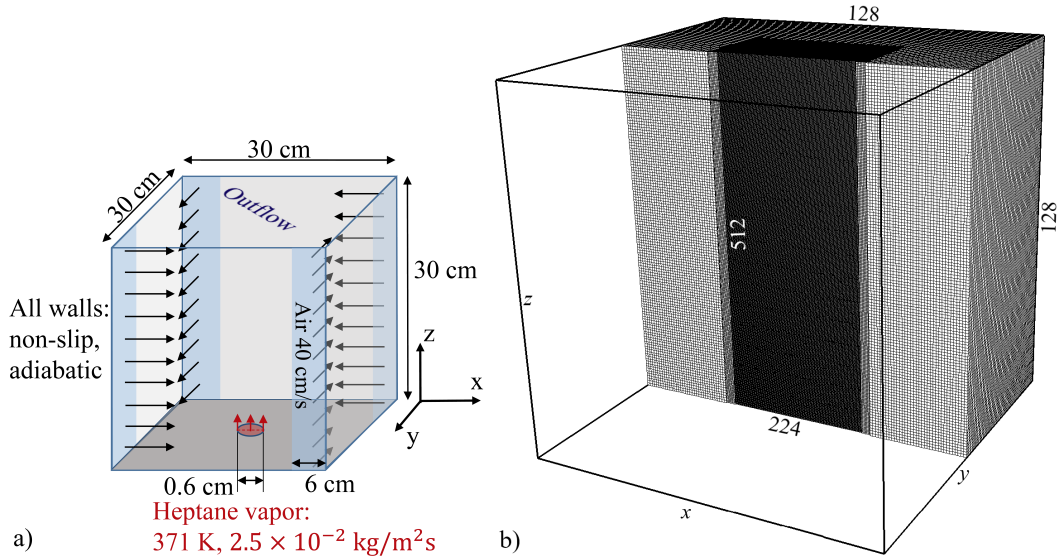


Figure 4.7: (a) The geometrical setup and boundary conditions. (b) A cut view of the computational mesh. The numbers indicate the number of cells at the coarsest and finest levels of refinement.

A schematic diagram of the geometrical setup and boundary conditions is

shown in Fig. 1a. The domain is a cube with sides that are 30 cm long. The upper boundary is an outflow condition and all other boundaries are non-slip, adiabatic walls. A fuel that is representative of heptane vapor is injected within a 0.6 cm diameter at the center of the bottom wall with a constant flux of 2.5×10^{-2} kg/m²s, equivalent to 0.55 ml/min liquid fuel volumetric flow rate. The inflow fuel temperature is 371 K, the evaporation temperature of heptane at 1 atm. Circulation is applied by forcing air through the four corners along slits which are 6.0 cm wide. The inflow air is 298 K and its velocity is 40 cm/s, orthogonal to the inflow boundary. The interior domain is initialized with quiescent air at 1 atm and 298 K with a column of hot product that is 1 cm in diameter and 10 cm high just above the fuel inflow for ignition. To avoid the generation of impulsive compression waves, the inflow of air and fuel are linearly accelerated from 0 m/s to their specified flux for the first 0.6 s of the computation.

The reactive BIC-FCT algorithm is incorporated into the BoxLib [62] adaptive mesh refinement library for parallelization and grid refinement. The mesh is Cartesian and each increasing level of refinement reduces the cell width by a half. The mesh refinement is conducted in advance, based on the anticipated flow structure. The computational mesh is shown in Fig. 4.7b. The number of cells along the height and width of the coarsest and finest levels of refinement are also shown. The finest cell size is $\Delta x = 0.586$ mm. The time-step size is limited by the convective CFL condition, which is 0.3.

4.4.2 Results and Discussion

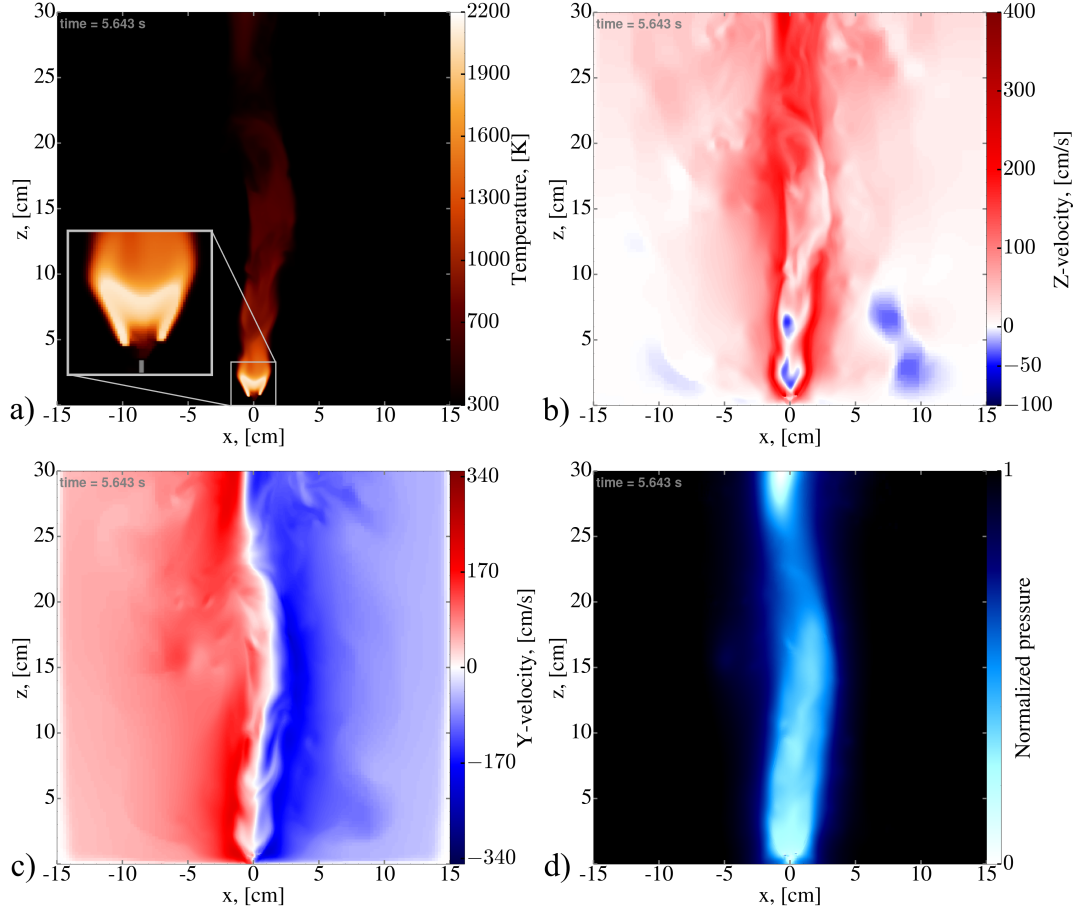


Figure 4.8: Contours of (a) temperature, (b) axial velocity, (c) tangential velocity, and (d) normalized pressure.

Center-slice contours of temperature, axial velocity, tangential velocity, and normalized pressure are shown in Fig. 4.8 at 5.6 s, after the flow has reached a quasi-steady-state. In the early stages of the formation, the initial column of hot products are convected out of the domain due to buoyancy. This establishes an axial velocity profile which promotes the radial inflow of oxidizer towards the influx of fuel within the boundary layer. A diffusion flame is then established and grows wider until the circulation from the air inflow couples with the hot, low-density

gas generated by the flame. A columnar vortex profile begins to form, and after 3.5 s, the swirl intensity near the fuel inflow becomes strong enough to cause vortex breakdown just above the fuel inflow region. Then at 4 s, the flame is lifted from the bottom floor as the radial inflow accelerates upward toward the axial direction. Figure 4.8a shows the lifted structure of the flame which is maintained for 2.5 s. At 6.5 s the flame is no longer lifted and precesses around the edge of the fuel injection boundary. The average peak temperature of the flame is 2150 K, approximately 150 K lower than the adiabatic flame temperature.

The computation shows the formation of two bubble modes. The first is defined by the finite reverse flow region in the center of the vortex axis just above the fuel inlet, shown as the blue region in the axial velocity contour of Fig. 4.8b. The bubble is surrounded by swirling gas. Most of the burning occurs within the lower half of this first bubble. Just outside of this reverse flow region, the axial velocity accelerates to 4 m/s, showing that the flow is moving around it due to the blockage effect of the bubble. This is consistent with nonreactive characteristics of the bubble mode. Just above the first bubble, at a height of approximately 4 cm, the peak tangential velocity moves closer to the vortex axis, showing the recovery of a columnar vortex. Here, the swirl is strong enough to generate another bubble mode at a height of 5 cm. Above this second bubble, the bulk motion of the vortex attains a precessing columnar structure but becomes more turbulent.

The contour is shown in Fig. 4.8d shows the pressure normalized by $(P - P_{max})/(P_{max} - P_{min})$. The average value of $(P_{max} - P_{min})$ in the computation is 6.4 Pa. The results show that the pressure is low near the core of the vortex and is

higher away from it. This is consistent with what is observed in vortex flows and further shows that the computation has established a strongly swirling flow.

To better understand the burning properties of the flame, we compute the flame index,

$$\text{Flame index} = \frac{\nabla Y_{fuel} \cdot \nabla Y_{oxidizer}}{|\nabla Y_{fuel}| |\nabla Y_{oxidizer}|}, \quad (4.1)$$

where Y_{fuel} and $Y_{oxidizer}$ are the fuel and oxidizer mass fractions, respectively. The flame index is a measure of the angle between the fuel and oxidizer gradients. When the gradients are pointing towards each other, the flame index is negative and shows a diffusion flame. When the gradients point in the same direction, the flame index is positive and shows a premixed flame. The flame index is shown in Fig. 4.9 along with the contour of stoichiometric mixture fraction shown in black and heat release contours shown by colors. Red regions of flame index are positive and the blue regions are negative. Figure 4.9 shows that most of the heat release occurs near the bottom of the flame, but significant burning still occurs within the inner structure of the bubble and on the outside. The burning in the center is a premixed flame whereas the burning along the stoichiometric contour is a diffusion flame. A small region of premixed burning exists outside of the stoichiometric region, suggesting a triple flame structure. It is likely the flame structure here requires further grid refinement.

The velocity and flame structure suggests that most of the burning occurs due to diffusive mixing processes and not due to convective mixing from the bubble. All the fuel is burned in the lower half of the bubble, within a perimeter outside of

the reverse flow region. The inner mixture of the bubble is fuel rich and the slow, recirculating flow within it increases the residence time of the fuel and provides sufficient time for it to diffuse towards the oxidizer in the outer part of the bubble.

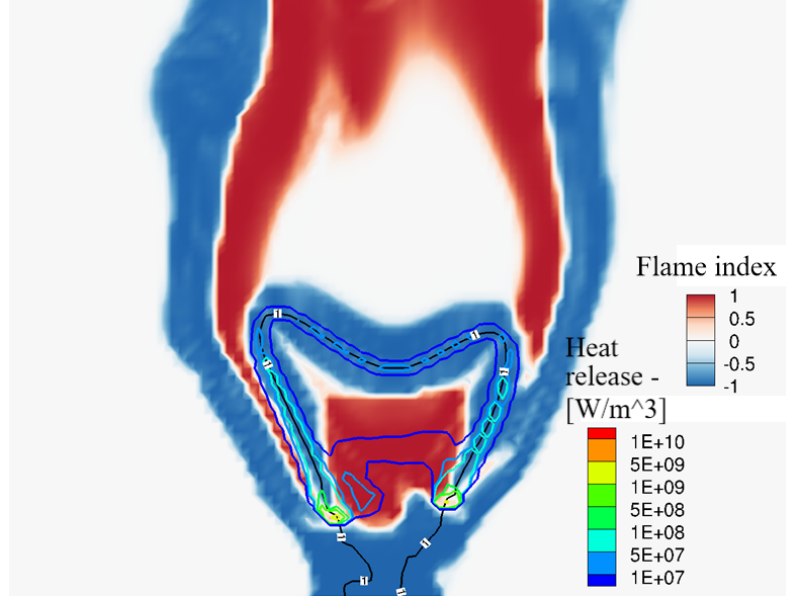


Figure 4.9: Contours of the flame index overlaid with contours of heat release within a zoomed in region of the reactive bubble.

4.4.3 Increased Resolution

We performed an additional simulation with increased resolution using the same boundary conditions described earlier in this section to determine how sensitivity of the solution to further refinement. Changes in the mesh are presented in Fig. 4.10. Figure 4.10a shows the original mesh and Fig. 4.10b shows the refined mesh. Compared to the previous mesh, the new mesh is finer at the coarse level and refines within an 11 cm box centered above the fuel inlet. The simulation here begins with 2 levels of refinement, which results in a smallest cell size that is equivalent to the finest level used in the original mesh. We further increase the refinement to 3

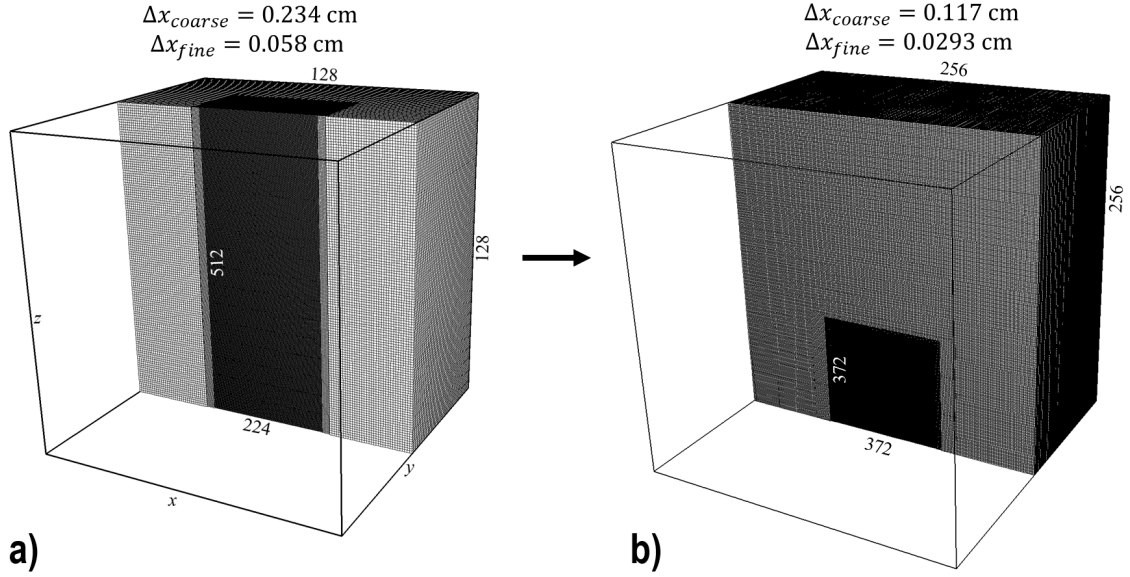


Figure 4.10: refinement

levels at 6.4 s, which is equivalent to an additional level of refinement in the original mesh. The simulation is then carried out for an additional 0.4 s.

At 2 levels of refinement, the solution is nearly identical to the original case and is therefore not presented here. When the mesh is refined to 3 levels, however, the flow shows many changes. In Fig. 4.11, we show these changes in vertical slices through different positions within the flame. These vertical slices show maps of temperature and a map of the fuel mass fraction is shown the bottom boundary ($z = 0$ m). A transparent contour of heat release rate is shown to illustrate the flame position. Figure 4.11 shows that the initially lifted flame is no longer lifted and is attached to the bottom boundary. It wanders around the fuel injection location and is no longer centered above it. The flame and its plume has also become more turbulent. The temperature in the center plane of the flame is the hottest and also shows a similar “cup”-like structure as seen in the less-refined case.

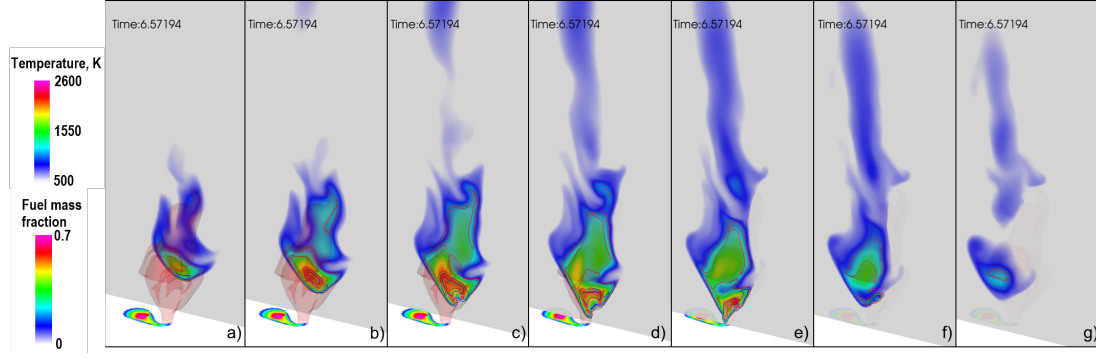


Figure 4.11: Temperature contour maps with superimposed heat release contour lines on vertical slices taken at various locations across the flame. From (a) to (g) vertical slices (z-y plane) are taken from $x = 0.144$ m to $x = 0.156$ m with a 0.002 m interval. The flame structure is shown by a 3D heat release surface contour with a value of 1×10^6 W/m³. A horizontal (x-y plane) slice is taken at the bottom of the domain ($z = 0$ m) colored by fuel mass fraction, on which the region with high fuel concentration indicates the fuel inflow.

Figure 4.12 shows maps of flame index overlaid with contours of heat release rate on vertical slices through the same positions in the flame as shown in Fig. 4.11. The heat release occurs in regions of diffusion and in premixed regions. The peak heat release occurs at the location where the premixed and diffusion regions join together. Overall, these results show that the flame has maintained a triple flame structure after mesh refinement.

4.4.4 Conclusions

This work has computed vortex breakdown and the resulting modes in a swirling diffusion flame by solving the unsteady, compressible, reactive NS equations. This computation has demonstrated the capability of a recently developed low-Mach-number solver and a calibrated chemical-diffusive model to compute the complex flow and flame structures of this flowfield. A fuel with burning properties

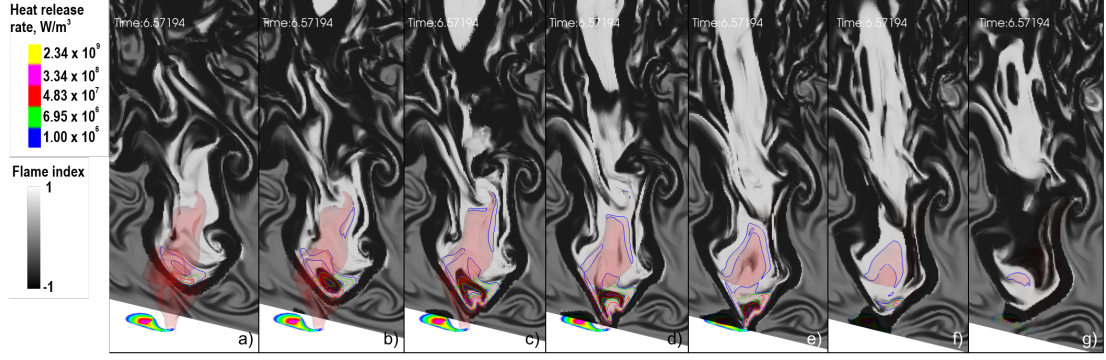


Figure 4.12: Flame index maps with superimposed heat release contour lines on vertical slices taken at various locations across the flame. From (a) to (g), vertical slices (z-y plane) are taken from $x = 0.144$ m to $x = 0.156$ m with a 0.002 m interval. The flame structure is shown by a 3D heat release surface contour with a value of 1×10^6 W/m³. A horizontal (x-y plane) slice is taken at the bottom of the domain ($z = 0$ m) colored by fuel mass fraction, on which the region with high fuel concentration indicates the fuel inflow.

of heptane was injected at the center of the bottom wall and circulation was applied by tangentially forcing air into the domain through four corners.

Two regions of vortex breakdown are observed, both exhibiting characteristics of the bubble mode. All the burning occurs within the lower half of the first bubble. The bubble traps a fuel-rich mixture inside of it. This fuel-rich mixture then continues to recirculate and diffuse excess fuel towards the oxidizer, causing most of the burning to occur within a diffusion flame. Computation of the flame index suggests that the burning occurs within a triple flame.

The mesh was further refined which led to changes in the flow and flame structure. The flow became more turbulent and the flame no longer remained lifted. The flame did, however, maintain its triple flame structure.

Chapter 5: Blue Whirl

This chapter presents the first results of unsteady, three-dimensional (3D) numerical simulations that examine vortex breakdown in a reactive flow that leads to a blue whirl. It reveals the flame and flow structure of the blue whirl through a series of numerical diagnostics, relates the results to prior experiments, and suggests a path forward for both future experiments and simulations to examine and potentially use this new, soot-free flame structure.

5.1 Computational setup

The computational setup for the simulation in this chapter, including the mesh and the initial and boundary conditions, is shown in Fig. 5.1. The domain is a cube with sides that are 30 cm long. The upper boundary is an outflow condition and all other boundaries are non-slip, adiabatic walls. Heptane vapor is injected within a specified diameter at the center of the bottom wall with a constant velocity of 5.8 cm/s and at the evaporation temperature of heptane at 1 atm, 371 K. This gaseous fuel flow rate is equivalent to a volumetric liquid fuel flow rate of 0.35 ml/min. The fuel inlet diameter varied from 2.54 cm to 0.9 cm during the simulation, which is explained in detail in the following “Simulation pathway” section.

Circulation is applied by forcing air through the four corners with a speed of 40 cm/s along slits which are 5 cm wide. Radial inflow is introduced by forcing air with a velocity of 60 cm/s through a 1.4 cm high and 16 cm wide region along the lower portion of the walls. The interior domain is initialized with quiescent air at 1 atm and 298 K with a column of hot product gas that is 1 cm in diameter and 10 cm high just above the fuel inflow for ignition.

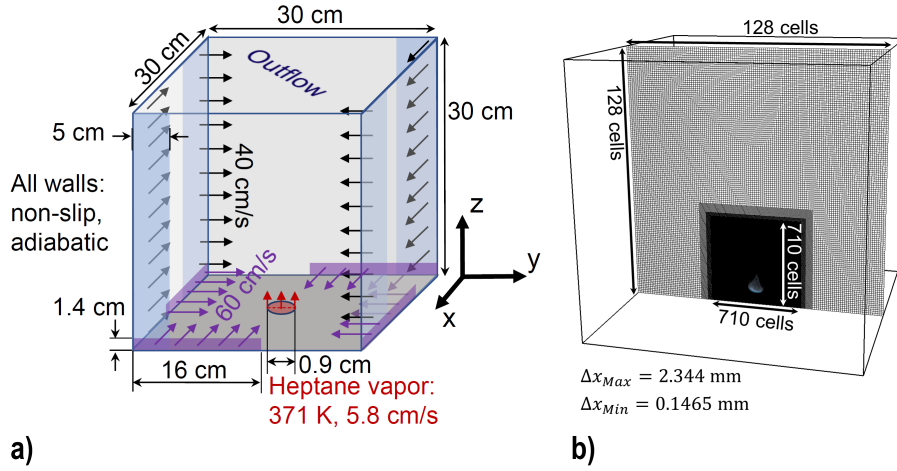


Figure 5.1: Computational setup. a) Schematic of the computational domain and the boundary conditions. b) A center slice of the 3D computational mesh. The mesh is composed of cubical control volumes. The width of the control volume in each level of refinement is half the width of the coarser level. The mesh is refined around the blue whirl which is shown as a volume rendering of the heat release rate. The size of the largest and smallest cells (Δx_{Max} , Δx_{Min} respectively) and the number of cells in the coarsest and finest mesh are indicated in b).

As shown in Fig. 5.1b, the simulations were performed on a 3D mesh which concentrated a fine grid along the center to cover the region of a blue whirl. The fine grid region is 10 cm in width, 10 cm in depth, and 10 cm in height. For the results shown, the width of the finest cell size in the center region was 0.01465 cm, corresponding to 5 levels of refinement from the coarsest cells at the edge of the domain. During the entire simulation, however, the mesh was slowly refined from 2

levels to 5 levels. This is explained in detail in the “Simulation pathway” section.

The adequacy of the numerical resolution was tested by increasing the levels of refinement in the blue-whirl region until there were no changes to the flow and flame structure. Refinement required for a premixed flame is reported in [48]. In this computation, there are enough computational cells within the flame thickness to give at most an 8% difference between the flame speed computed by BIC-FCT and the ideal value computed by chemical equilibrium software [58, 61]. In the rich and lean flame regions, this difference is smaller because there are more cells within the flame thickness since nonstoichiometric flames are thicker. The resolution in this simulation is also enough to resolve a diffusion flame, for which a cell size of 0.07 cm or smaller is required, determined by solving 2D counter-flow diffusion flames.

5.2 Simulation pathway

The computational search for the blue whirl took its lead from the experiments. We started the simulation with air and fuel flow rates close to the experimental measurements, which are air inflow of 40 m/s at the corner gaps and 60 m/s at the lower gaps along the bottom boundary and the equivalent liquid fuel volumetric flow rate of 0.4 ml/min [15]. From here, the simulation pathway took *five* steps.

1. First, we started with specifying the fuel inlet diameter as 2.54 cm. The resulting gaseous fuel inlet velocity is 0.9 cm/s. We used 2 levels of mesh refinement with the coarsest mesh described in the “Computational setup” section. Figure 5.2 shows a temperature map of the first step, overlaid with a contour of

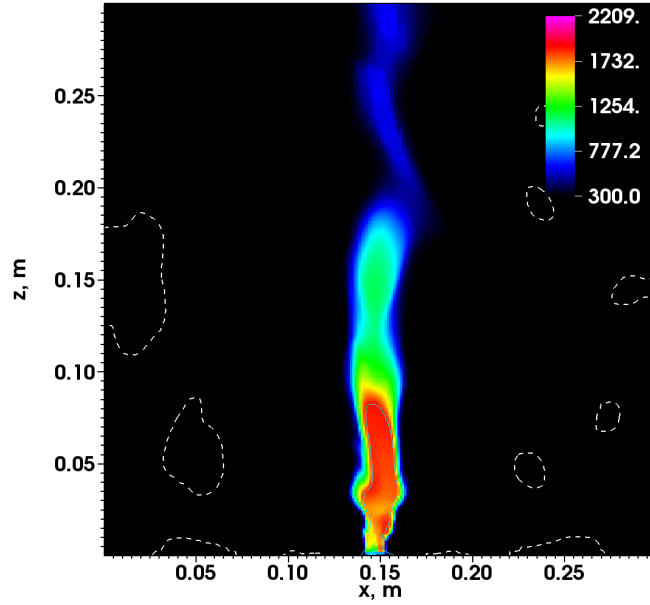


Figure 5.2: First step in the simulation pathway. Center-slice map of temperature (shown in units of K). Solid teal line is the stoichiometric contour. The dashed white lines are contours of zero axial velocity, indicating the regions of reverse flow. The mesh is refined with 2 levels and the fuel inflow diameter is 2.54 cm with an equivalent liquid fuel supply rate of 0.4 ml/min.

the stoichiometric equivalence ratio and zero-axial velocity, indicating regions of reverse flow. After the initial transient development, the flow reached a quasi-steady state with a whirling flame attached to the bottom boundary and no negative axial velocity was observed within the flame or vortex axis. The average flame width is 1.7 cm and the average flame height is 10 cm.

2. Then, in the second step, the fuel inlet diameter was decreased to 0.9 cm while all the rest configurations were kept the same. The resulting fuel inlet velocity is 5.8 cm/s. The resulting temperature map is shown in Fig. 5.3. After the flow reached the new quasi-steady state, the flame was lifted from the bottom boundary and stable, but there was still no negative axial velocity

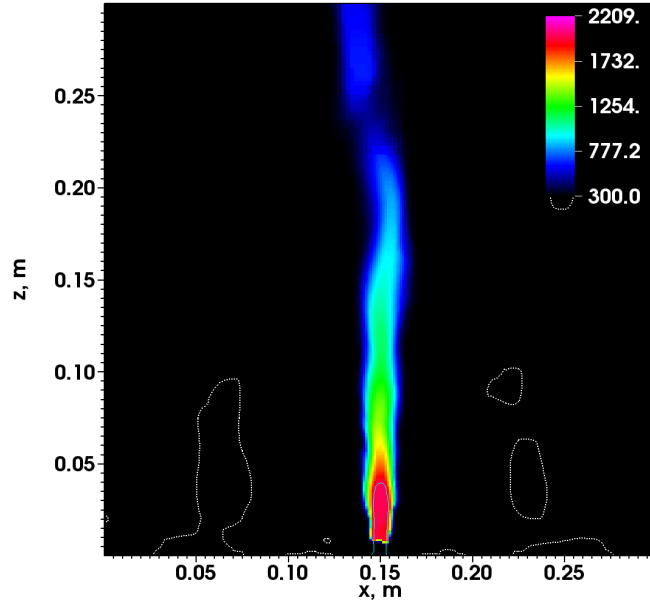


Figure 5.3: Second step in the simulation pathway. The fuel inflow diameter is decreased from 2.54 cm to 0.9 cm and the equivalent liquid fuel supply rate is changed from 0.4 ml/min to 0.35 ml/min. See Fig. 5.2 for color and contour description.

along the vortex axis, and hence, no sign of vortex breakdown. The flame is approximately 1.1 cm wide, 3 cm tall, and lifted by 0.7 cm.

3. In the third step, the mesh refinement was increased to 3 levels. The temperature map is shown in Fig. 5.4. At this quasi-steady state, the flame was still lifted and stable, but here, a recirculation zone formed inside the flame, which indicated vortex breakdown. The flame is approximately 1.2 cm wide, 5 cm tall, and lifted by 0.9 cm. The flame is relatively long and slender compared with the observed blue whirl. The minimum axial velocity is approximately -27 cm/s.
4. In the fourth step, the mesh was further refined to 4 levels. The temperature

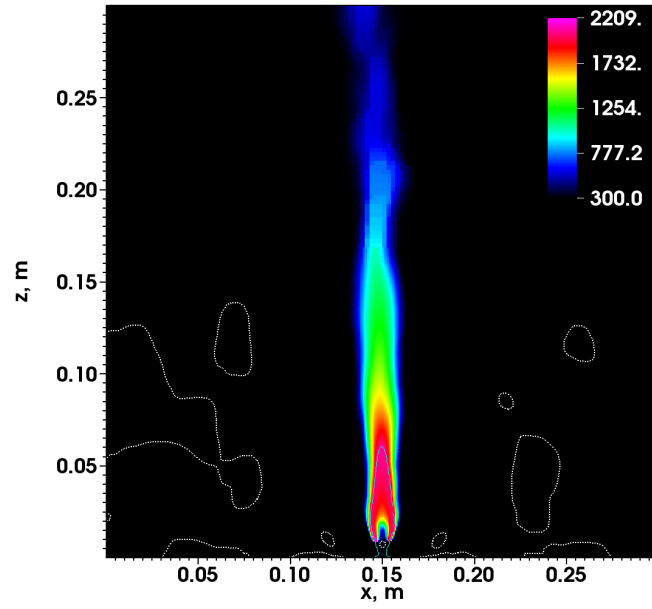


Figure 5.4: Third step in the simulation pathway. The mesh is refined another level from the second step. See Fig. 5.2 for color and contour description.

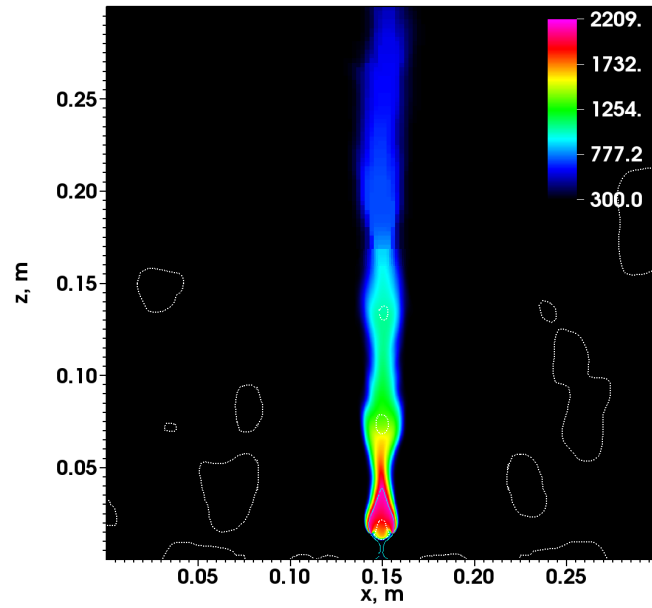


Figure 5.5: Fourth step in the simulation pathway. The mesh is refined another level from the third step. See Fig. 5.2 for color and contour description.

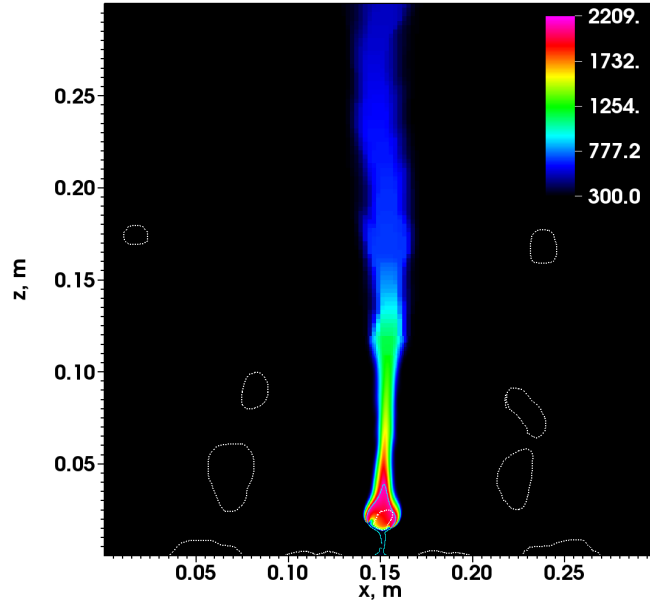


Figure 5.6: Fifth step in the simulation pathway. The mesh is refined another level from the fourth step. See Fig. 5.2 for color and contour description.

map is shown in Fig. 5.5. The flame was lifted more and the reverse flow became stronger. After the flow reached a quasi-steady state, the flame became flatter, wider and the blue whirl structure appeared. The flame is approximately 1.4 cm wide, 2.5 cm tall, and lifted by 1.1 cm. The minimum axial velocity oscillated between approximately -90 cm/s to -70 cm/s. Here, there are three regions of reverse flow along the vortex axis.

5. Finally, the mesh was refined to 5 levels. The temperature map is shown in Fig. 5.6. The structure of the blue whirl was maintained and the flame is approximately 1.6 cm wide, 1.5 cm tall, and lifted by 1.6cm. The minimum axial velocity oscillated between approximately -65 cm/s to -55 cm/s. Although the two reverse flow regions above the flame are no longer present in this step,

there was no major changes in the flow and flame structure near the flame region. We thus consider the solution to be well resolved and the result shown in this chapter is one time instance taken from the calculation at this stage.

5.3 Results

The simulation in this paper began with a whirling flame which went through several transitional stages, with the blue whirl emerging as the result of vortex breakdown. At the quasi-steady state, the blue whirl slightly meanders and tilts but remains stable through the duration of the simulation. To explain the dynamics of the blue whirl, and understand its relation to vortex breakdown and flame theory, we focus here on one time instance in a quasi-steady solution.

5.3.1 The flame structure revealed

Figure 5.7a is a volume rendering of the heat release rate from the final result of the blue-whirl simulation effort. Figure 5.7b is a schematic diagram that summarizes the result. It is posed next to Fig. 5.7c, the observed blue whirl. We see now that the blue whirl is composed of four types of flames. The lower part of the blue whirl is a rich premixed flame, and the purple crown is a diffusion flame. What cannot be seen easily in the laboratory experiments is the lean premixed flame surrounding the purple haze, that is, the upper region just outside of the diffusion flame. The bright blue ring is where the three types of flames meet, which is a triple flame. The interpretations presented in the schematic diagram in Fig. 5.7 are derived from

data extracted from simulations in which an initial flow structure was given and allowed to evolve to a point where the basic blue-whirl structure no longer changed significantly in time.

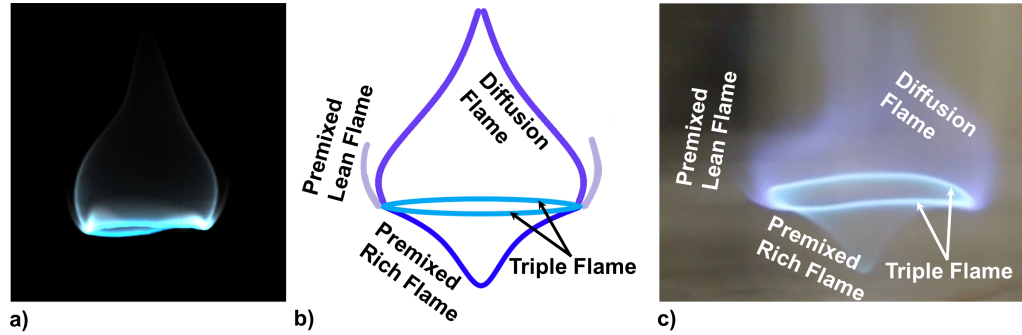


Figure 5.7: The flame structure of the blue whirl. a) Volume rendering of the heat release rate from the numerical simulation described in the text. b) Schematic diagram that summarizes a final result of the blue whirl simulation. c) Observed blue whirl.

The simulations consider a cubical enclosure with an open boundary at the top and non-slip walls at the lateral and the bottom boundaries. Heptane vapor is injected at the center of the bottom wall with a constant velocity. Circulation is applied by forcing air through four gaps along the corners of the lateral walls. The details of the computational setup is described later in the Method section.

Figure 5.8 is a comparison between the blue whirl experiment [14] and the simulation. The luminosity in Fig. 5.8a shows the experimental OH^* concentration [14] which indicates the intensity of the reaction. For the simulation result, this is indicated by the 3D volume rendering of the heat release rate shown in Fig. 5.8b (now readjusted in greyscale in contrast with Fig. 5.7a). Bright regions indicate stronger reaction and darker regions indicate weaker reaction. Both the experiment and simulation show that a significant amount of combustion occurs within the

blue ring. The simulation result shown here agrees well with the experimental measurement in terms of curvature of the reaction regions and distribution of the reaction.

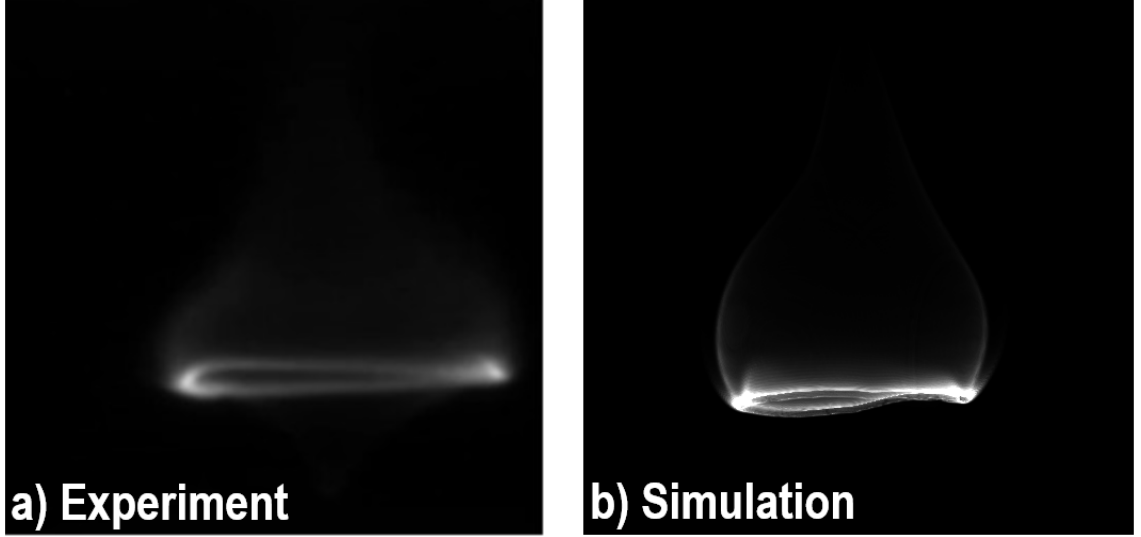


Figure 5.8: Comparison of a) experimental OH* concentration measurement (taken from Fig. 8a in [14]) with b) 3D volume rendering of heat release rate in the simulation. The volume rendering is taken from the side view.

Figure 5.9a is a map of the flame index [69], $I_f = \nabla Y_{\text{Fuel}} \cdot \nabla Y_{\text{Ox}} / |\nabla Y_{\text{Fuel}}| |\nabla Y_{\text{Ox}}|$, where Y_{Fuel} and Y_{Ox} are computed values of the mass fraction of fuel and oxidizer, respectively. $I_f > 0$ is a premixed flame and $I_f < 0$ is a diffusion flame. Fig. 5.9b is the corresponding map of equivalence ratio, ϕ , and Fig. 5.9c shows temperature. Contours of heat release rate are superimposed on each figure to indicate reaction regions.

In Fig. 5.9a, region 1 has positive I_f , and in Fig. 5.9b, region 1 has equivalence ratio larger than 1. Taken together, the heat-release rate in region 1 corresponds to a premixed fuel-rich flame. By similar reasoning, the heat release rate in region 2 corresponds to a diffusion flame, because region 2 has negative I_f and an equivalence

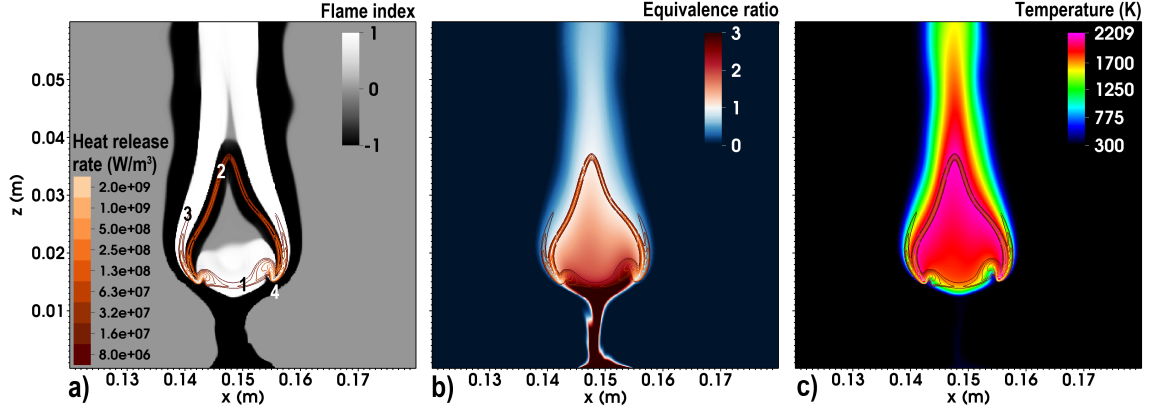


Figure 5.9: Slices through the center of the computational domain and parameters selected for combustion diagnostics. a) Flame index. b) Equivalence ratio. c) Temperature. Contours of heat release rate are superimposed on top to indicate reaction regions. Slices are shown for a zoomed in region which is 8 cm wide.

ratio of 1. The heat release rate in region 3 corresponds to a premixed fuel-lean premixed flame because region 3 has positive I_f and equivalence ratio less than 1. Region 4 is where the three flames meet and is the triple flame (or blue ring in the experiments). It has the most intense heat release, which is consistent with the OH^* experimental measurements [14] as mentioned earlier. The temperature map, Fig. 5.9c, shows that the hottest regions are the diffusion flame in the purple crown, in agreement with the experimental measurements [13, 14], and the region at the bright blue ring (that could not be measured in the experiment). The peak temperature in the simulation is 2209 K. It is slightly higher than the peak temperature measured in the experiment, which is around 2000 K [13]. Fig. 5.9 shows a gap between the flame and bottom surface, again consistent with the experimental observations [1]. Analysis of the composition of the data at the top of the computational grid shows that essentially all of the fuel is consumed in the blue whirl and only hot product and air exit the computational domain.

5.3.2 Flow structure

The flow structure shown confirms and elaborates on experimental observations. Figure 5.10 is a composite showing (a) streamlines, (b) tangential and (c) axial velocities, again all with superimposed heat release rate as an indicator of the flame location, as well as (d) a profile of the tangential velocity through a slice below the blue whirl. The evolution to this structure from the initial conditions (not shown here) in the simulation show the development of a whirling flame which undergoes vortex breakdown, leading to the typical bubble-mode.

The bubble mode of vortex breakdown is revealed by the streamlines in Fig. 5.10a. It shows that the recirculation zones are inside the flame and in particular, the vortex rim is inside what we see as the blue ring. This is in qualitative agreement with the experimental results shown in Fig. 1.1b, where the recirculation zone illuminated by the soot pattern is inside the blue rim. The tangential velocity map in Fig. 5.10b shows that below the flame, the peak tangential velocity is high and the vortex core is narrow. This is more easily seen in the tangential velocity profile shown in Fig. 5.10d, which is extracted along the white dashed line in Fig. 5.10b. The peak tangential velocity is approximately 2.3 m/s and the vortex core is 0.6 cm measured from the positive and negative tangential velocity. The peak tangential velocity is higher and the vortex core is narrower comparing with the initial whirling flame stage, at which the peak tangential velocity is around 1.8 m/s and the vortex core is about 1.2 cm (not shown here). The upper portion of the tangential velocity map shows the flow recovering the vortex structure as it leaves the bubble. The

axial velocity map in Fig. 5.10c shows a jet-like velocity profile below the flame with a maximum axial velocity of 4.5 m/s. Within the lower part of the flame, there is a negative axial velocity region, and taken together with the streamlines in Fig. 5.10a, we again see the characteristics of a vortex-breakdown bubble inside the flame. The minimum negative axial velocity oscillates between around -0.65 m/s to -0.55 m/s at the quasi-steady state. In the upper portion of the flame, above the bubble, the flow is accelerating in the axial direction as shown in the the axial velocity map. This acceleration is an upward-moving jet of hot product gas, caused by the volumetric expansion from the flame and buoyancy effects. The resulting shear layer forms roll-ups, as seen in Fig. 5.10c, which show that it is beginning to go unstable. This instability has not, however, transitioned to turbulence and the flow structure remains laminar above the flame.

5.3.3 Comparison with Burgers vortex model

The Burgers vortex model is a solution of the Navier-Stokes equations that describes the velocity profile of a viscous vortex. Viscous diffusion causes the vortex core to become wider. Radial forces which push inward on the vortex cause the core to become narrower. The Burgers vortex model balances these two effects. Recent experimental work [7, 18, 72] have shown that the Burgers vortex provides the best fit for the velocity field of a fire whirl. Here, we compare the tangential velocity of the blue whirl at different heights with the Burgers vortex model to determine how well the blue whirl velocity field can be approximated by existing vortex theory.

The equation that gives the tangential velocity profile of a Burgers vortex is given by Eq. 3.6 in Chapter 3. The equation for circulation is given by Eq. 3.9.

Figure 5.11 shows the comparison of the numerical simulation with the Burgers

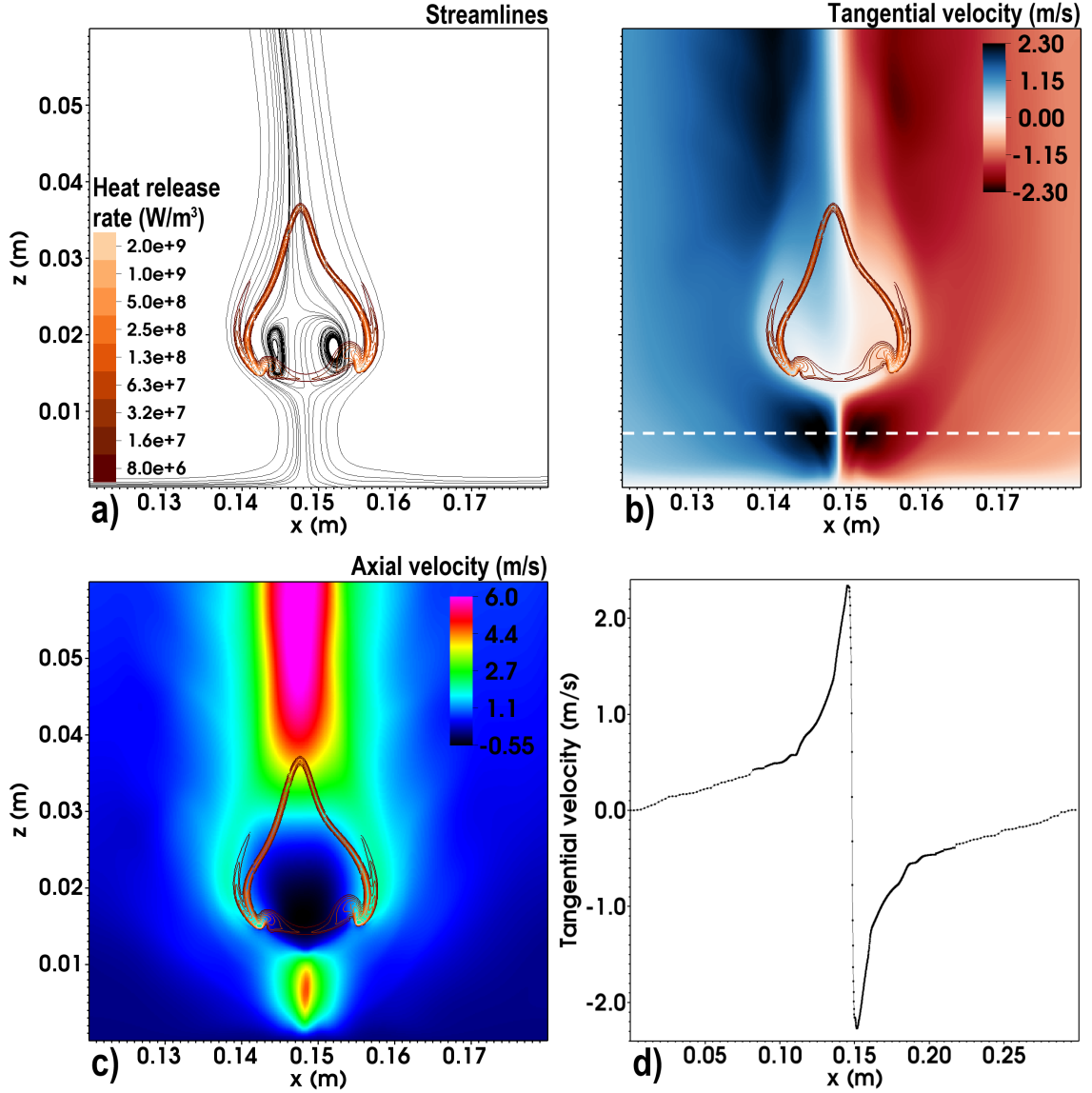


Figure 5.10: Slices through the center of the computational domain and values selected for flow diagnostics. a) Streamlines. b) Tangential velocity. c) Axial velocity. Contours of heat release rate are superimposed on top to indicate reaction regions. Slices are shown for a zoomed in region which is 8 cm wide. d) Line plot of tangential velocity taken below the blue whirl from the white dashed line in b), shown for the entire width of the computational domain.

vortex as computed from Eq. 3.6. The tangential velocity profile of the numerical simulation shown in Fig. 5.11 is extracted from a height of 7 mm above the bottom floor and about 5 mm below the flame for a single time instance. Here, the value of the freestream circulation Γ_0 used in Eq. 3.6 is determined from the tangential velocity of the simulation at a radius of 5 cm from the center of the vortex. The center of the vortex core, where the radius is equal to 0, is defined to be the location where the tangential velocity is zero. The resulting Γ_0 is $0.1665 \text{ m}^2/\text{s}$, the vortex core radius, as measured from the location of peak tangential velocity, is 2.99 mm, and the parameter k used in Eq. 3.6 is 1.404×10^5 . In Fig. 5.11a, the peak tangential velocity predicted by the Burgers vortex is 268% higher than the numerical simulation. The Burgers vortex over predicts the tangential velocity from the center of the vortex to the outer vortex region. The circulation is computed in the same way as Chapter 3 and is shown in Fig. 5.11b. Similar to the tangential velocity, the Burgers vortex also over predicts the circulation.

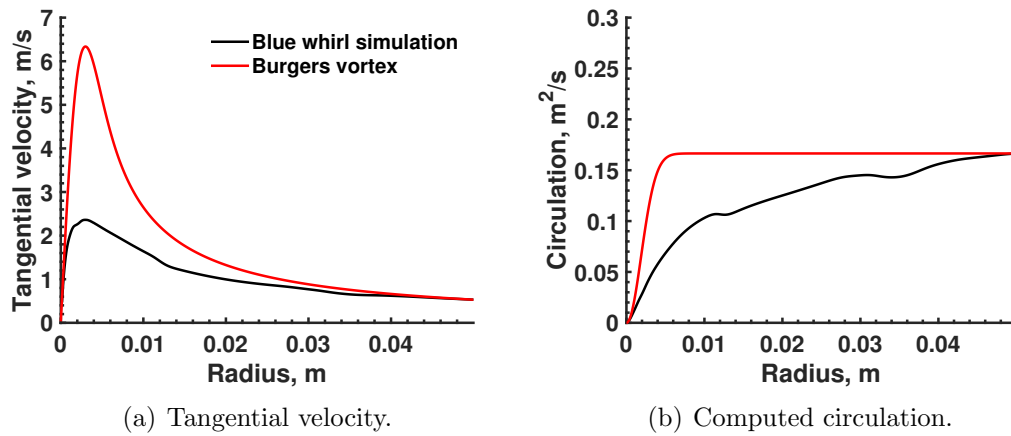


Figure 5.11: A comparison of a time instance from the blue whirl simulation and a curve fit using the Burgers vortex model for tangential velocity. The simulation results are extracted along the x direction at a height of 7 mm, about 5 mm below the flame.

We also compare the vortex profile in the plume region of the simulation with the Burgers vortex. Figure 5.12 shows the comparison at a height of 80 mm, which is approximately 40 mm above the flame. Here, Γ_0 is $0.2426 \text{ m}^2/\text{s}$, vortex core radius is 8.68 mm, and k is 1.667×10^4 . Figure 5.12a shows that the Burgers vortex over predicts the peak tangential velocity by 152%. Figure 5.12b shows that the Burgers vortex over predicts the circulation for all radial locations. The agreement in the plume is better than near the floor as shown in Fig. 5.11 and this is most likely due to additional viscous effects from the boundary layer on the floor. These results suggest that the Burgers vortex may be not be sufficiently adequate to describe the flow field of the blue whirl.

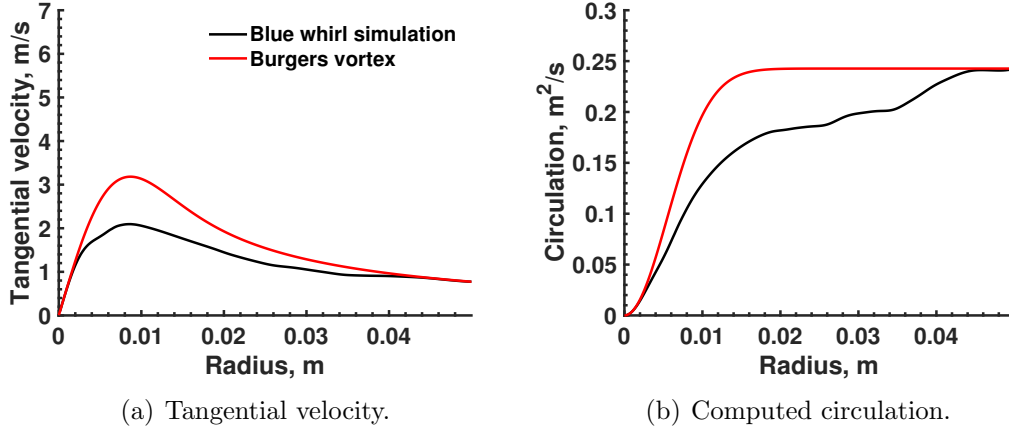


Figure 5.12: A comparison of a time instance from the blue whirl simulation and a curve fit using the Burgers vortex model for tangential velocity. The simulation results are extracted along the x direction at a height of 80 mm, approximately 40 mm above the flame.

5.3.4 Boundary layer diagnostics

Finally, we use information from the flow streamlines in Fig. 5.13 superimposed on a 3D map of heat release rate (yellow structure in the figure) to show how air

from the boundary layer is introduced into the flame. The streamlines are colored by the local temperature of the flow. The four streamlines start at 5 cm from the center of fuel injection on an $x - y$ plane. The streamlines in Fig. 5.13a and Fig. 5.13b originate at two different heights from the lower boundary, 0.5 mm and 2.0 mm, respectively.

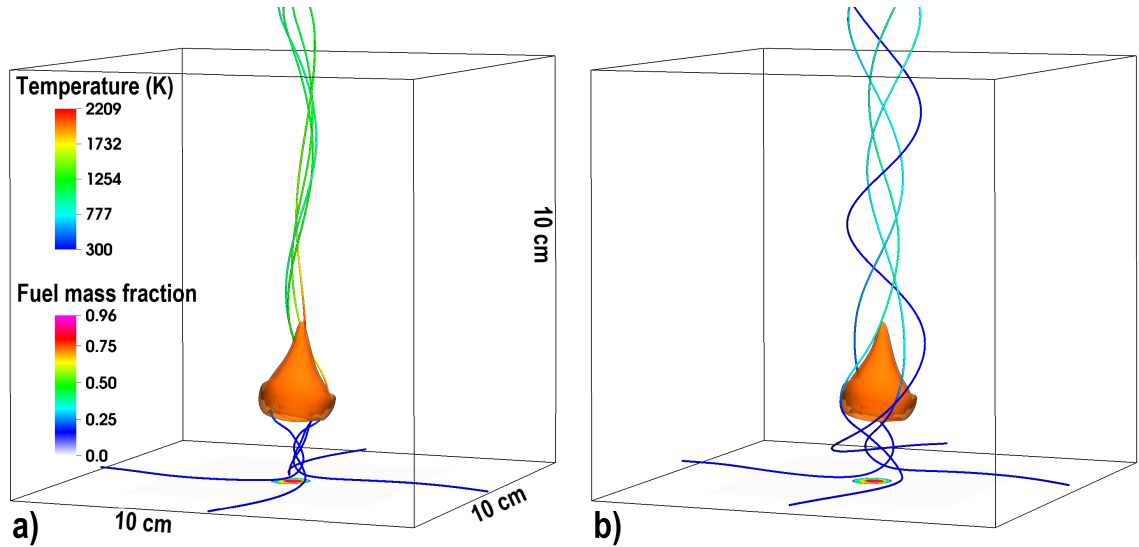


Figure 5.13: Streamlines superimposed on a 3D heat release rate isocontour of 3 MW/m^3 . a) Streamlines which originate at 0.5 mm from the lower boundary. b) Streamlines which originate at 2.0 mm from the lower boundary. The streamlines are colored by the local temperature of the flow. A 2D map of fuel mass fraction along the bottom boundary is shown, indicating the region of fuel inflow. The box indicates the region of mesh refinement.

First, from Fig. 5.13b, we see that air from the higher portion of the boundary layer maintains a low temperature of 300 K even after moving around the flame. This shows that air from the upper part of the boundary layer is not involved in the combustion process. (This is also consistent with the experiments in which you can put your hand right up to the flame on the sides and it does not feel hot.)

The story is different, however, with air from the lower part of the boundary

layer, shown in Fig. 5.13a, depending on the height at which the flow reaches the upward draft and is pulled into the flame. Air from very close to the bottom boundary, as shown here, first encounters the heptane vapor and is mixed due to the strong circulation below the bubble. This forms the rich premixed flame conditions seen at the bottom of the bubble. Then most of the residual, unburned fuel and product is pulled into the bubble, which is shown in bubble mode simulations. This region inside the bubble creates the fuel rich region which feeds the diffusion flame in the crown.

Meanwhile and simultaneously, air from higher in the boundary layer, here between the bottom (e.g., the 0.5 mm height) and the 2.0 mm height, is drawn upwards and flows around the entire structure. Outside air and the residual fuel from inside the bubble set up a diffusion flame bordering the crown. A small amount of fuel also leaks outside of the bubble and burns with the outside air to form a very lean premixed flame outside of the crown. All of these flames – the rich premixed flame, the diffusion flame, and the lean premixed flame – come together as a triple flame and occurs at the blue ring.

5.4 Discussion

The flame and flow structure of the blue whirl is now revealed by solving the 3D time-dependent Navier-Stokes equations coupled to a model for chemical energy release and species conversion from fuel to product for heptane gas. The result was achieved by using the experimental conditions as a starting point and then varying

the physical conditions represented in the calculations until the blue whirl appeared. The blue whirl is composed of three different flame structures, a diffusion flame and a premixed rich and lean flame. All of these flames meet in a fourth structure, a triple flame, which appears as a whirling blue ring. The blue whirl emerges as the result of vortex breakdown. It consumes all fuel as there is no unburned fuel measured in the computational domain. The structure of the blue whirl and its flow properties provide an excellent starting point for examining some of the fundamental questions related to the blue whirl, such as how and whether it might scale to larger sizes and whether it can be made directly without going through the fire whirl state. There are several elements of the physical results that should be discussed before the numerical model is described in more detail.

The 3D unsteady numerical simulation described in this paper is one of many simulations carried out in which boundary and fuel inflow conditions were successively varied until a flame structure appeared that was in qualitative and even quantitative agreement with the observed blue whirl. Many computations with variations in geometrical, physical, and computational parameters were required to find this solution shown above. Critical elements in finding the solutions consisted of determining the appropriate air and fuel inflow geometry and the inflow rate of air and fuel to allow vortex breakdown to occur, the flame to lift away from the bottom surface, and the blue whirl to form. The details of the path leading to the solutions in this paper are described in the Methods section.

Notable differences between the experiments reported and the simulations include: fuel injection vs fuel evaporation; the shape of the external container; self-

determining inflow boundary conditions vs forced air inflow. The primary difference in physical conditions from the reported experiments is that the process of heptane evaporation was bypassed by assuming a small forced inflow of pure heptane gas (here 371 K) at the bottom of the domain. Recent experiments have shown the blue whirl can be obtained from gaseous fuel injection, which verifies our approach of not including fuel evaporation. Experiments performed in square containers have been reported to produce blue whirls. Thus we know the blue whirl does not depend on the external shape of the container. The formation of the blue whirl is sensitive to the inflow boundary conditions. We know, however, that it is more easily formed when the inflow conditions are as smooth and laminar as possible.

The blue whirl is *at least* a curious phenomenon that has many intriguing aspects. The most curious aspect is that it evolves spontaneously and presents itself as a stable state persisting until all of the fuel is burned. The second curiosity was that it is laminar and burning soot free, whereas the initial state was sooty, turbulent, and noisy. A third curiosity was that in the experiments, it was not burning a gas, but a liquid hydrocarbon sitting on a water surface. Further experimentation revealed more features, such as its averaged temperature profile and its sensitivity to the boundary layer. Added to all of this was that it was very beautiful, both in its stable state, as a spinning blue top-like flame, and when it went slightly unstable, perhaps revealing some of its inner structure. The route to its formation and its transient unstable states implied its relation to the fluid phenomenon of vortex breakdown and the various states that evolve from this instability.

A recurring question, however, was whether the blue whirl could be useful in

any way for efficient combustion with no soot formation. This involves questions such as: Can it be formed under controlled conditions more directly and without going through the fire whirl state? Can the size be controlled? Can it be made larger or smaller? Is there a scaling that can be used? Other, perhaps more far out questions, were: Can it be made without the confining walls? Can multiple blue whirls be made and work together? Could it be part of a combustor or a propulsion device? The lure of being able to burn any liquid hydrocarbon efficiently and cleanly is extremely attractive.

None of these questions can be answered easily until we at least understand the structure and dynamics of the flame and have a tool through which we can easily explore some of these questions. This paper describes a first step: a tool that can be used to explore and test the phenomenon, and how it has been used to reveal the blue whirl structure.

5.5 Computational resources required

With two levels of mesh refinement, this computation covered 12 s of physical time and with three levels of refinement, the computation covered another 3 s of physical time. The computation covered another 0.6 s of physical time in total with four and five levels of refinement, 0.3 s each. The final mesh with five levels of refinement contains 410 million cells. The computation overall took about 600,000 CPU hours on 40 Dell Poweredge C8220 nodes using dual Intel Ivy Bridge E5-2680v2 processors running at 2.80 GHz with 20 cores per node.

Chapter 6: Summary and Conclusions

This thesis has studied a newly discovered flame [1] called the blue whirl. It is a small, stable, swirling flame that was discovered [1] to form from a large, sooty fire whirl. The blue whirl burns heavy hydrocarbon, liquid fuels on top of water and its blue emission indicates clean, efficient combustion. Understanding its structure is a critical step to harness its potential for low-emission combustion. This work, for the first time, has presented the flame and flow structure of the blue whirl. The structure was computed by performing numerical simulations which took their lead from experimental observations and measurements. To perform these simulations, we developed a new computational tool that can compute the unsteady dynamics of low-Mach-number, reactive flows. This work also presented the numerical methods and models used in this computational tool.

First, we developed a combustion model, the CDM, to compute both premixed and non-premixed systems. The CDM, in the present formulation, assumes an irreversible, one-step reaction which is governed by an Arrhenius-type rate. The pre-exponential factor and activation energy in this Arrhenius rate and the heat release were calibrated over a range of equivalence ratios ranging from fuel-lean to fuel-rich. They were calibrated to reproduce the critical properties of 1D, premixed

flames at these equivalence ratios in a Navier-Stokes computation. These properties are the flame temperature, speed, and thickness. This work extended the CDM to compute reactive mixtures with varying stoichiometry, allowing for the computation for diffusion flames. The procedure for doing this was presented.

The CDM was then integrated into an algorithm, BIC-FCT, which solves the Navier-Stokes equations for low-Mach-number flows. BIC-FCT removes the sound speed restriction on integration time steps by using explicit FCT as a predictor and then applying a corrector by solving an elliptic equation for a pressure correction. In a time step, the BIC-FCT procedure first integrates non-convective processes, such as diffusion and chemistry. During this, all changes in internal energy are removed and stored as a separate scalar variable, S , to prevent constol-volume combustion. Then, the explicit prediction step is performed by solving the inviscid conservation laws of mass and momentum using an explicit, one-step, Euler time integration with an unsplit [63] version Flux-Correct Transport [46]. The conservation of energy is also solved in this step and the changes in internal energy S are then added back into the energy equation as a source term. After the explicit prediction, the implicit prediction is carried out by solving a single elliptic equation for a pressure correction, which is then applied to the energy and momentum. A conservative filter is applied to the conserved variables (mass, momentum, and energy) to remove any spurious oscillations which may arise from the pressure correction.

The combined BIC-FCT-CDM algorithm was applied to a series of six test problems, each with successively increasing difficulty. Simulations of 1D, premixed flames showed that BIC-FCT with the CDM can reproduce the flame speed, thick-

ness, and temperature of more detailed chemical-transport models [58, 59]. Simulations of a 2D coflow diffusion flame show that the algorithm is able to compute the qualitative features of a diffusion flame, such as the peak temperature occurring and reactant concentration depleting along the stoichiometric contour. 2D counter flow diffusion flame simulations show that the flow structure, such as the temperature, velocity, and species profile show good qualitative agreement with chemical equilibrium software [61] using more detailed chemical-transport models [59]. The results also showed that BIC-FCT with the CDM can capture the trends of a strained diffusion flame, where temperature decreases with increasing strain. With sufficient strain, the flame is extinguished showing for the first time that the CDM can compute extinction. Computation of a 2D triple flame shows that the algorithm can compute complex heat release structures in laminar flows. 2D, unsteady, reactive coflow flame computations show that BIC-FCT-CDM can compute a lifted diffusion flame and that the chosen outflow boundary conditions have minimal reflections into the domain as flow eddies with large density gradients are convected out of it. Finally, the test problems culminated with a simulation of a 3D, unsteady fire whirl. The resulting temperature and velocity profiles showed good qualitative agreement with prior experimental [3, 5, 17, 18, 71, 72] and numerical work [23, 24]. The tangential velocity profile in the plume also showed quantitative agreement with Burgers vortex model, in agreement with prior experimental work [7, 18, 72]. These results demonstrate that BIC-FCT-CDM can compute a fire whirl.

Using the newly developed BIC-FCT-CDM code, a series of reactive vortex breakdown computations were performed in an effort to “find” the blue whirl in

the simulations. The computations considered square enclosures with walls at the bottom and sides and an outflow at the top. A constant flux of fuel was specified at the center of the bottom boundary with air forced in at the corners of the domain to impose circulation. The diameter of the fuel flux and the fuel mass flow rate were varied, using the experimental measurements as a starting point. A narrow fuel injection area, around 6 mm wide diameter, with an equivalent liquid fuel flow rate of 0.3 ml/min results in a lifted flame with vortex breakdown. Some key characteristics, however, such as the turbulence and heat release structure indicate that this was not the blue whirl.

Finally, by introducing additional air inflow partially at the corners between the bottom floor and lateral walls, i.e. partially “lifting” the wall, the lifted flame became stabilized and resulted in a heat release structure which agreed with experimental OH* chemiluminescence measurements of the blue whirl. The flame structure was composed of a fuel-rich premixed flame at the bottom blue cone of the blue whirl, a diffusion flame in the upper hazy region, a fuel-lean premixed flame outside of the diffusion flame, and a triple-flame at the blue ring. The results also showed the bubble mode of vortex breakdown within the flame.

This work has answered a fundamental question of the blue whirl: What is the flame and flow structure? The blue ring was shown to be a merging region for a diffusion flame, premixed-lean flame, and premixed-rich flame, all of which are stabilized by the bubble mode of vortex breakdown. This work described the final state of this new self-stabilized, self-sustained, soot-free flame. More questions, however, need to be addressed in the future to determine whether we can harness

its potential for soot-free combustion. For example, can the blue whirl be scaled to smaller or larger sizes? Can we bypass the sooty, fire-whirl states all together? Can the blue whirl be formed under more controlled conditions? Can it be made without confining walls or with a smaller confinement? Can there be multiple blue whirls made to work together? In the pathway to simulate the blue whirl in this work, two key features were critical for the formation of the blue whirl: the lifted flame and bubble mode of vortex breakdown. These two key conditions should serve as a guide for further studies on other aspects of the blue whirl. Also, the boundary layer near the bottom floor was also found to be critical for the oxidizer that is burned by the blue whirl. The numerical tool that was developed from this study can be used for future numerical experiments to address these stated questions and even finding new directions as further experiments and simulations are performed.

6.1 Summary of Contributions

A list of the key contributions is listed below:

1. Identified the flame and flow structure of the blue whirl.
2. Developed a low dissipation algorithm for low-Mach-number, reactive flows and CFD code was developed and tested for a wide variety of combustion applications.
3. For the first time, showed that the chemical-diffusive model can be used to compute both premixed and diffusion flames.

6.2 Recommendations for Future Work

A series of simulations, which are not presented here, showed what could be the transitional structures seen in the formation of the blue whirl. These results suggest that further simulations, where the fuel inflow and air inflow are controlled as functions of time could force the flow to transition from fire whirl to blue whirl. The numerical model and code developed in this thesis provides the basis for this future study.

This thesis showed that the chemical-diffusive model can compute the strain versus temperature relationship of counter flow diffusion flames, along with extinction. Better agreement could be obtained here if an additional parameter is added to the Arrhenius rate which could be calibrated to match the strain versus temperature of experiments or detailed chemistry. This additional parameter could be T^n where T is temperature and n would be a potential parameter for calibration.

An axi-symmetric, 2D model would be a useful tool to perform further parametric studies on the blue whirl. It would help answer the question of whether the blue whirl could scale to larger sizes in a computationally efficient way.

Finally, a more comprehensive set of boundary conditions could be included in the current model. One would be an evaporation model including the effects of heat conduction, convection, and radiation on the fuel surface could be included along with air inflow conditions which are not forced. These changes would allow us to better understand *why* the transition from fire whirl to blue whirl occurs.

Appendix A: Parametric study results

These are results of the parametric study in Chapter 4.

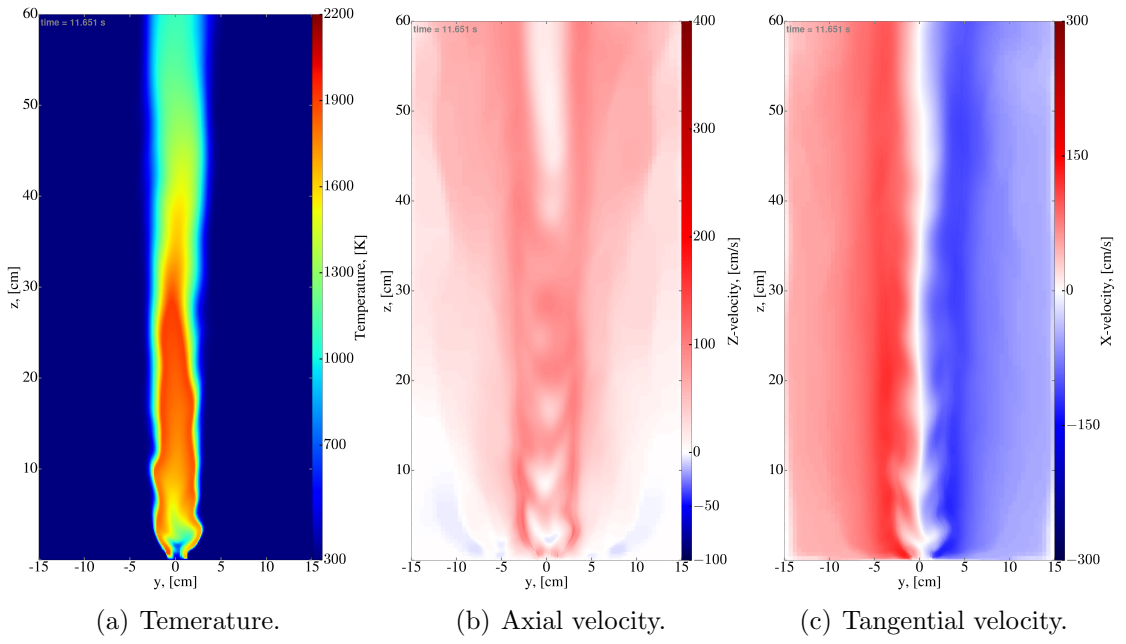


Figure A.1: Case 2

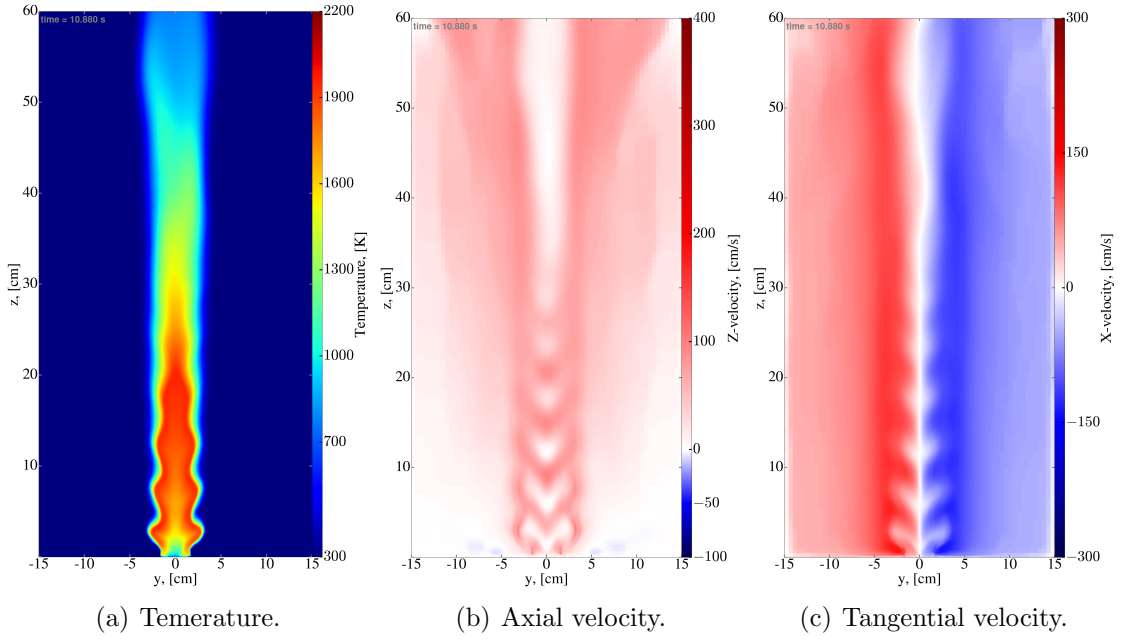


Figure A.2: Case 3

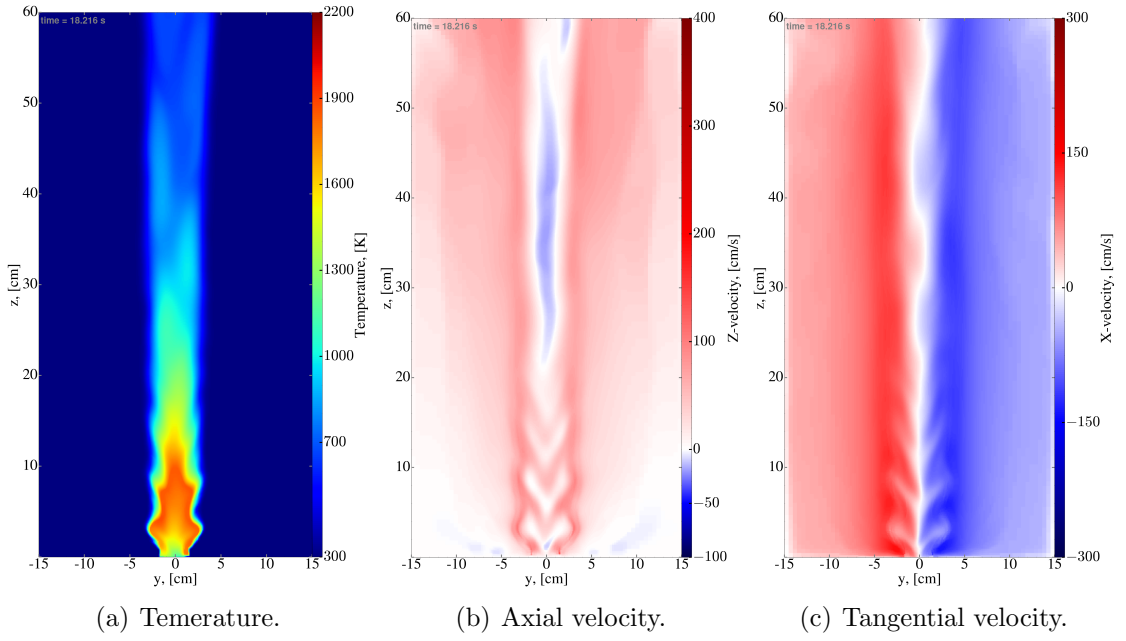


Figure A.3: Case 4

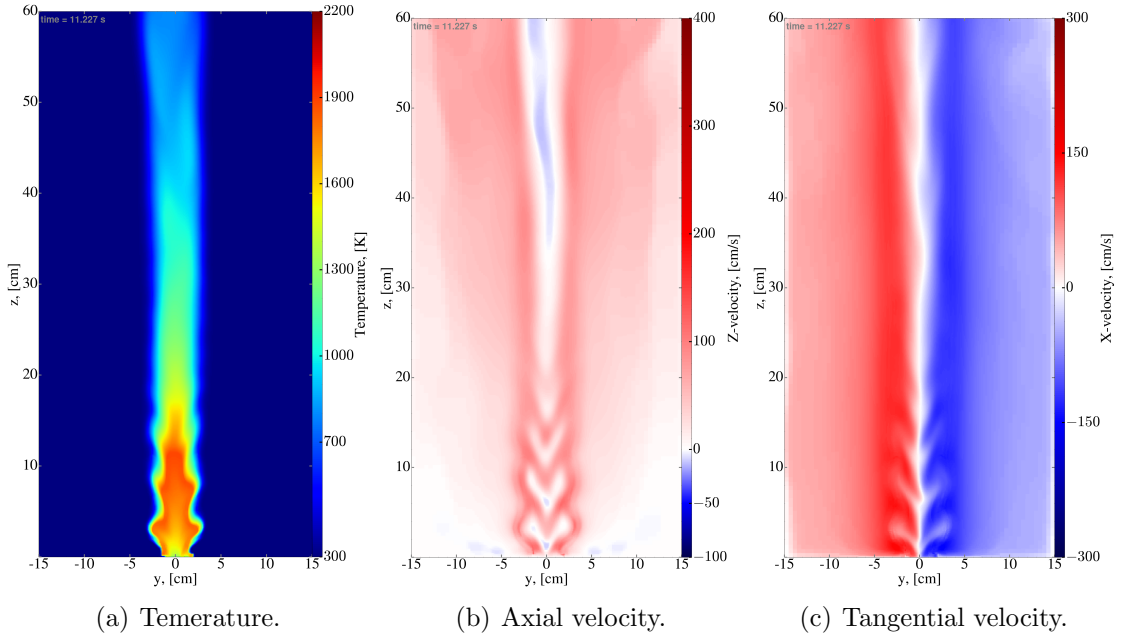


Figure A.4: Case 5

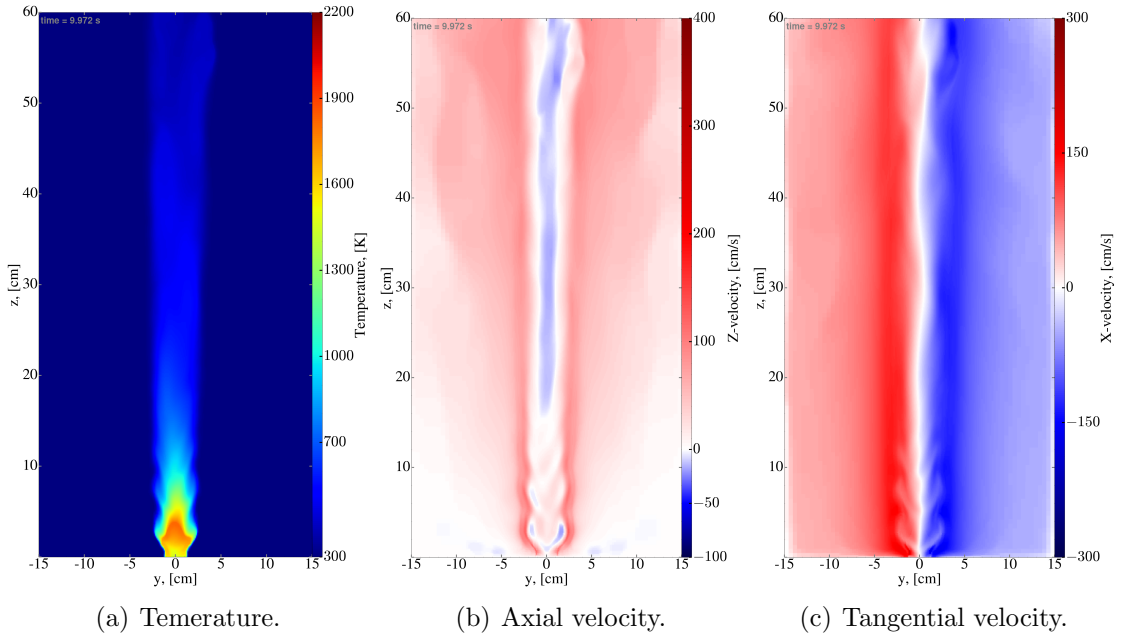


Figure A.5: Case 7

Bibliography

- [1] Huahua Xiao, Michael J Gollner, and Elaine S Oran. From fire whirls to blue whirls and combustion with reduced pollution. *Proceedings of the National Academy of Sciences*, 113(34):9457–9462, 2016.
- [2] GEORGE M Byram and RE Martin. Fire whirlwinds in the laboratory. *Fire Control Notes*, 33(1):13–17, 1962.
- [3] Howard W Emmons and Shuh-Jing Ying. The fire whirl. In *Symposium (international) on Combustion*, volume 11, pages 475–488. Elsevier, 1967.
- [4] MOHAMED I Hassan, KAZUNORI Kuwana, KOZO Saito, and FENGJUAN Wang. Flow structure of a fixed-frame type firewhirl. *Fire Safety Science*, 8: 951–962, 2005.
- [5] Jiao Lei, Naian Liu, Linhe Zhang, Haixiang Chen, Lifu Shu, Pu Chen, Zhihua Deng, Jiping Zhu, Kohyu Satoh, and John L de Ris. Experimental research on

- combustion dynamics of medium-scale fire whirl. *Proceedings of the Combustion Institute*, 33(2):2407–2415, 2011.
- [6] YASUHIRO Hayashi, KAZUNORI Kuwana, and RITSU Dobashi. Influence of vortex structure on fire whirl behavior. *Fire Safety Science*, 10:671–679, 2011.
 - [7] Pengfei Wang, Naian Liu, Katherine Hartl, and Alexander Smits. Measurement of the flow field of fire whirl. *Fire Technology*, 52(1):263–272, 2016.
 - [8] KA Hartl and Alexander J Smits. Scaling of a small scale burner fire whirl. *Combustion and Flame*, 163:202–208, 2016.
 - [9] AM Grishin, AN Golovanov, AA Kolesnikov, AA Stokratov, and R Sh Tsvyk. Experimental study of thermal and fire tornados. In *Doklady Physics*, volume 50, pages 66–68. Springer, 2005.
 - [10] BR Morton. The physics of fire whirls. In *Fire Research Abstracts and Reviews*. National Academy of Sciences, 1970.
 - [11] Ritsu Dobashi, Tetsuya Okura, Ryosuke Nagaoka, Yasuhiro Hayashi, and Toshio Mogi. Experimental study on flame height and radiant heat of fire whirls. *Fire Technology*, 52(4):1069–1080, 2016.
 - [12] Sriram Bharath Hariharan. The structure of the blue whirl: a soot-free reacting vortex phenomenon, 2017.
 - [13] Sriram Bharath Hariharan, Evan T Sluder, Michael J Gollner, and Elaine S

- Oran. Thermal structure of the blue whirl. *Proceedings of the Combustion Institute*, 37(3):4285–4293, 2019.
- [14] Sriram Bharath Hariharan, Paul M Anderson, Huahua Xiao, Michael J Gollner, and Elaine S Oran. The blue whirl: Boundary layer effects, temperature and oh* measurements. *Combustion and Flame*, 203:352–361, 2019.
- [15] Yu Hu, Sriram Bharath Hariharan, Haiying Qi, Michael J Gollner, and Elaine S Oran. Conditions for formation of the blue whirl. *Combustion and Flame*, 205:147–153, 2019.
- [16] Wilfried Coenen, Erik J Kolb, Antonio L Sánchez, and Forman A Williams. Observed dependence of characteristics of liquid-pool fires on swirl magnitude. *Combustion and Flame*, 205:1–6, 2019.
- [17] Ali Tohidi, Michael J Gollner, and Huahua Xiao. Fire whirls. *Annual Review of Fluid Mechanics*, 50:187–213, 2018.
- [18] Jiao Lei, Naian Liu, Linhe Zhang, and Kohyu Satoh. Temperature, velocity and air entrainment of fire whirl plume: a comprehensive experimental investigation. *Combustion and Flame*, 162(3):745–758, 2015.
- [19] Jiao Lei, Naian Liu, Yan Jiao, and Shaojie Zhang. Experimental investigation on flame patterns of buoyant diffusion flame in a large range of imposed circulations. *Proceedings of the Combustion Institute*, 36(2):3149–3156, 2017.
- [20] K Satoh and KT Yang. Simulations of swirling fires controlled by channeled self-generated entrainment flows. *Fire Safety Science*, 5:201–212, 1997.

- [21] A Yu Snegirev, JA Marsden, J Francis, and GM Makhviladze. Numerical studies and experimental observations of whirling flames. *International journal of heat and mass transfer*, 47(12-13):2523–2539, 2004.
- [22] Keng Hoo Chuah and Genichiro Kushida. The prediction of flame heights and flame shapes of small fire whirls. *Proceedings of the Combustion Institute*, 31(2):2599–2606, 2007.
- [23] Kazunori Kuwana, Satoshi Morishita, Ritsu Dobashi, Keng H Chuah, and Kozo Saito. The burning rate’s effect on the flame length of weak fire whirls. *Proceedings of the Combustion Institute*, 33(2):2425–2432, 2011.
- [24] ACY Yuen, GH Yeoh, Sherman CP Cheung, QN Chan, TBY Chen, W Yang, and H Lu. Numerical study of the development and angular speed of a small-scale fire whirl. *Journal of computational science*, 27:21–34, 2018.
- [25] RM Parente, JMC Pereira, and JCF Pereira. On the influence of circulation on fire whirl height. *Fire Safety Journal*, 106:146–154, 2019.
- [26] Turgut Sarpkaya. On stationary and travelling vortex breakdowns. *Journal of Fluid Mechanics*, 45(3):545–559, 1971.
- [27] Sidney Leibovich. The structure of vortex breakdown. *Annual review of fluid mechanics*, 10(1):221–246, 1978.
- [28] Lewis Mununga, D Lo Jacono, Jens Nørkær Sørensen, Thomas Leweke, Mark C Thompson, and Kerry Hourigan. Control of confined vortex breakdown with partial rotating lids. *Journal of Fluid Mechanics*, 738:5–33, 2014.

- [29] Xiao Zhang, Joseph D Chung, Carolyn R Kaplan, and Elaine S Oran. The barely implicit correction algorithm for low-mach-number flows. *Computers & Fluids*, 175:230–245, 2018.
- [30] Joseph D Chung, Xiao Zhang, Carolyn R Kaplan, and Elaine S Oran. Low-Mach-number simulation of diffusion flames with the chemical-diffusive model. In *AIAA Scitech 2019 Forum*, page 2169, 2019.
- [31] Elaine S Oran and Jay P Boris. *Numerical simulation of reactive flow*. Cambridge University Press, 2005.
- [32] Fernando F Grinstein, Len G Margolin, and William J Rider. *Implicit large eddy simulation: computing turbulent fluid dynamics*. Cambridge university press, 2007.
- [33] IJ Keshtiban, F Belblidia, and MF Webster. Compressible flow solvers for low mach number flows—a review. *Int. J. Numer. Methods Fluids*, 23:77–103, 2004.
- [34] Eli Turkel. Preconditioned methods for solving the incompressible and low speed compressible equations. *Journal of computational physics*, 72(2):277–298, 1987.
- [35] Y-H Choi and Charles L Merkle. The application of preconditioning in viscous flows. *Journal of Computational Physics*, 105(2):207–223, 1993.
- [36] Meng-Sing Liou. A sequel to ausm, part ii: Ausm+-up for all speeds. *Journal of computational physics*, 214(1):137–170, 2006.

- [37] Walter W Jones and Jay P Boris. Flame and reactive jet studies using a self-consistent two-dimensional hydrocode. *The Journal of Physical Chemistry*, 81(25):2532–2534, 1977.
- [38] R Rehm and H Baum. The equations of motion for thermally driven, buoyant flows. *Journal of Research of the NBS*, 83:297–308, 1978.
- [39] Ben Thornber, Andrew Mosedale, Dimitris Drikakis, David Youngs, and Robin JR Williams. An improved reconstruction method for compressible flows with low Mach number features. *Journal of computational Physics*, 227(10):4873–4894, 2008.
- [40] SV Patankar and DB Spalding. A calculation procedure for heat, mass and momentum transfer in three-dimensional parabolic flows. *International Journal of Heat and Mass Transfer*, 15(10):1787–1806, 1972.
- [41] JP Van Doormaal and GD Raithby. Enhancements of the simple method for predicting incompressible fluid flows. *Numerical heat transfer*, 7(2):147–163, 1984.
- [42] AG Tomboulides, JCY Lee, and SA Orszag. Numerical simulation of low mach number reactive flows. *Journal of Scientific Computing*, 12(2):139–167, 1997.
- [43] Emmanuel Motheau and John Abraham. A high-order numerical algorithm for dns of low-Mach-number reactive flows with detailed chemistry and quasi-spectral accuracy. *Journal of Computational Physics*, 313:430–454, 2016.

- [44] G Patnaik, RH Guirguis, JP Boris, and ES Oran. A barely implicit correction for flux-corrected transport. *Journal of Computational Physics*, 71(1):1–20, 1987.
- [45] G Patnaik, KJ Laskey, K Kailasanath, ES Oran, and TA Brun. FLIC - A detailed, two-dimensional flame model. *NRL Memorandum report*, 6555, 1989.
- [46] Jay P Boris, Alexandra M Landsberg, Elaine S Oran, and John H Gardner. LCPFCT-A flux-corrected transport algorithm for solving generalized continuity equations. Technical report, NAVAL RESEARCH LAB WASHINGTON DC, 1993.
- [47] Carolyn R Kaplan, Alp Özgen, and Elaine S Oran. Chemical-diffusive models for flame acceleration and transition-to-detonation: genetic algorithm and optimisation procedure. *Combustion Theory and Modelling*, 23(1):67–86, 2019.
- [48] DA Kessler, VN Gamezo, and ES Oran. Simulations of flame acceleration and deflagration-to-detonation transitions in methane–air systems. *Combustion and Flame*, 157(11):2063–2077, 2010.
- [49] Jay P Boris and David L Book. Flux-corrected transport. i. SHASTA, a fluid transport algorithm that works. *Journal of computational physics*, 11(1):38–69, 1973.
- [50] Charles K Westbrook and Frederick L Dryer. Simplified reaction mechanisms for the oxidation of hydrocarbon fuels in flames. *Combustion Science and Technology*, 27(1-2):31–43, 1981.

- [51] Eduardo Fernández-Tarrazo, Antonio L Sánchez, Amable Linan, and Forman A Williams. A simple one-step chemistry model for partially premixed hydrocarbon combustion. *Combustion and Flame*, 147(1):32–38, 2006.
- [52] Elaine S Oran, J. P. Boris, TR Young Jr, M Flanigan, and T Burks. Simulations of gas phase detonations: Introduction of an induction parameter model. Technical report, Naval Research Lab Washington D.C., 1980.
- [53] Alexei M Khokhlov and Elaine S Oran. Numerical simulation of detonation initiation in a flame brush: the role of hot spots. *Combustion and Flame*, 119(4):400–416, 1999.
- [54] Alexei M Khokhlov, Elaine S Oran, Almadena Yu Chtchelkanova, and J Craig Wheeler. Interaction of a shock with a sinusoidally perturbed flame. *Combustion and Flame*, 117(1-2):99–116, 1999.
- [55] Vadim N Gamezo, Daniel Desbordes, and Elaine S Oran. Formation and evolution of two-dimensional cellular detonations. *Combustion and Flame*, 116(1-2):154–165, 1999.
- [56] D. A. Kessler, V. N. Gamezo, and E. S. Oran. Gas-phase detonation propagation in mixture composition gradients. *Phil. Trans. R. Soc. A*, 370(1960):567–596, 2012.
- [57] Carolyn R Kaplan, Alp Ozgen, and Elaine S Oran. Chemical-diffusive models for flame acceleration and transition to detonation: Genetic algorithm and optimization procedure. *accepted to Combustion Theory and Modeling*, 2018.

- [58] Tianfeng Lu and Chung K Law. Linear time reduction of large kinetic mechanisms with directed relation graph: n-heptane and iso-octane. *Combustion and Flame*, 144(1-2):24–36, 2006.
- [59] Hai Wang and Alexander Laskin. A comprehensive kinetic model of ethylene and acetylene oxidation at high temperatures. *Progress Report for an AFOSR New World Vista Program*, 1998.
- [60] Vadim N Gamezo, Alexei M Khokhlov, and Elaine S Oran. The influence of shock bifurcations on shock-flame interactions and ddt. *Combustion and flame*, 126(4):1810–1826, 2001.
- [61] David G. Goodwin, Harry K. Moffat, and Raymond L. Speth. Cantera: An object-oriented software toolkit for chemical kinetics, thermodynamics, and transport processes. <http://www.cantera.org>, 2017. Version 2.3.0.
- [62] Boxlib users’s guide website. URL <https://ccse.lbl.gov/BoxLib/>.
- [63] Steven T Zalesak. Fully multidimensional flux-corrected transport algorithms for fluids. *Journal of computational physics*, 31(3):335–362, 1979.
- [64] C Richard DeVore. An improved limiter for multidimensional flux-corrected transport. Technical report, NAVAL RESEARCH LAB WASHINGTON DC, 1998.
- [65] SH Chung. Stabilization, propagation and instability of tribrachial triple flames. *Proceedings of the Combustion Institute*, 31(1):877–892, 2007.

- [66] H Phillips. Flame in a buoyant methane layer. In *Symposium (International) on Combustion*, volume 10, pages 1277–1283. Elsevier, 1965.
- [67] PN Kioni, B Rogg, KNC Bray, and A Linán. Flame spread in laminar mixing layers: the triple flame. *Combustion and Flame*, 95(3):276–290, 1993.
- [68] Tarek Echekki and Jacqueline H Chen. Structure and propagation of methanol–air triple flames. *Combustion and Flame*, 114(1-2):231–245, 1998.
- [69] H Yamashita, M Shimada, and T Takeno. A numerical study on flame stability at the transition point of jet diffusion flames. In *Symposium (International) on Combustion*, volume 26, pages 27–34. Elsevier, 1996.
- [70] Matthew J Turk, Britton D Smith, Jeffrey S Oishi, Stephen Skory, Samuel W Skillman, Tom Abel, and Michael L Norman. yt: A multi-code analysis toolkit for astrophysical simulation data. *The Astrophysical Journal Supplement Series*, 192(1):9, 2010.
- [71] Kuibin Zhou, Naian Liu, Jesse S Lozano, Yanlong Shan, Bin Yao, and Kohyu Satoh. Effect of flow circulation on combustion dynamics of fire whirl. *Proceedings of the Combustion Institute*, 34(2):2617–2624, 2013.
- [72] Katherine Anderson Hartl. *Experimental investigation of laboratory fire whirls*. PhD thesis, 2016.
- [73] Turgut Sarpkaya. Vortex breakdown in swirling conical flows. *AIAA J*, 9(9):1792–1799, 1971.

- [74] MG Hall. Vortex breakdown. *Annual review of fluid mechanics*, 4(1):195–218, 1972.
- [75] Walter John Grabowski and SA Berger. Solutions of the Navier-Stokes equations for vortex breakdown. *Journal of Fluid Mechanics*, 75(3):525–544, 1976.
- [76] RE Spall, TB Gatski, and RL Ash. The structure and dynamics of bubble-type vortex breakdown. In *Proceedings of the Royal Society of London A: Mathematical, Physical and Engineering Sciences*, volume 429, pages 613–637. The Royal Society, 1990.
- [77] MR Ruith, P Chen, E Meiburg, and T Maxworthy. Three-dimensional vortex breakdown in swirling jets and wakes: direct numerical simulation. *Journal of Fluid Mechanics*, 486:331–378, 2003.
- [78] Ying Huang and Vigor Yang. Effect of swirl on combustion dynamics in a lean-premixed swirl-stabilized combustor. *Proceedings of the Combustion Institute*, 30(2):1775–1782, 2005.
- [79] Christophe Duwig and Laszlo Fuchs. Large eddy simulation of vortex breakdown/flame interaction. *Physics of Fluids*, 19(7):075103, 2007.
- [80] Francis H Harlow and Anthony A Amsden. Numerical calculation of multiphase fluid flow. *Journal of Computational Physics*, 17(1):19–52, 1975.